NASA CONTRACTOR REPORT

NASA CR-578

NASA CR-578

PREDICTED AND MEASURED PERFORMANCE OF TWO FULL-SCALE DUCTED PROPELLERS

by A. R. Kriebel and M. R. Mendenhall

Prepared by
ITEK CORPORATION
Palo Alto, Calif.
for Ames Research Center

NATIONAL AERONAUTICS AND SPACE ADMINISTRATION • WASHINGTON, D. C. • SEPTEMBER 1966

NASA CR-578

PREDICTED AND MEASURED PERFORMANCE OF TWO FULL-SCALE DUCTED PROPELLERS

By A. R. Kriebel and M. R. Mendenhall

Prepared under Contract No. NAS 2-2647 by
ITEK CORPORATION
Palo Alto, Calif.

for Ames Research Center

NATIONAL AERONAUTICS AND SPACE ADMINISTRATION

For sale by the Clearinghouse for Federal Scientific and Technical Information
Springfield, Virginia 22151 – Price $3.00

TABLE OF CONTENTS

LIST OF SYMBOLS

A	area of duct exit plane, $\pi D^2/4$
A_P	propeller disk area, $\pi/4 \left(D_P^2 - D_H^2 \right)$
B_n	Fourier series coefficients for v_γ, Equation (16)
B_n^*	Fourier series coefficients for u_γ, Equation (15)
c	chord length of duct
c_n	Glauert series coefficients for γ_α, Equation (20)
C_m	pitching moment coefficient, M/RAq
C_n	Glauert series coefficients for γ_D, Equation (17)
C_N	normal force coefficient, N/Aq
C_p	pressure coefficient, $1 - u_s^2/V^2$
C_T	thrust coefficient, T/Aq
D	diameter of duct exit plane and duct reference cylinder
D_H	maximum diameter of hub
D_P	diameter of propeller
f_n	functions of c/D, Equations (4), (5), and (6)
H	boundary-layer shape factor, δ^*/θ
J	propeller advance ratio, V/nD_P
ℓ	length derived from duct velocity profile, Sketch C, page 21
M	aerodynamic pitching moment about the duct midchord diameter, positive clockwise, Sketch A, page 5
n	propeller rotational speed, rev/sec
N	normal force, Sketch A, page 5
p_t	measured total pressure

p_{t_∞}	free-stream total pressure
$P_{k\ell}$	coefficients from Reference 4, Tables VI and VII, Equation (19)
q	free-stream dynamic pressure, $\rho V^2/2$
r_s	local radius of duct surface, Sketch B, page 7
R	radius of duct exit plane, D/2
Re_θ	Reynolds number based on momentum thickness θ, $u_s(\theta)/\nu$
Re_∞	free-stream Reynolds number per foot, V/ν
R_n	Fourier series coefficients of duct camberline, Equation (11)
R_N^*	Fourier series coefficients for effective camberline of thick duct, Equation (13)
t	duct thickness
T	thrust force, Sketch A, page 5
u	local velocity in the duct boundary layer
u_s, u_s^*	local velocity at duct surface, and at duct camberline, Sketch B, page 7
u_γ, v_γ	axial and radial velocity components induced at duct reference cylinder by trailing vortex cylinder, Equations (15) and (16)
$u_{\gamma_D}, v_{\gamma_D}$	axial and radial velocity components induced at duct reference cylinder by vorticity bound to duct reference cylinder, Equations (18) and (19)
u_{γ_α}	axial velocity generated at duct reference cylinder by angle of attack, Equation (20)
V	free-stream velocity, Sketch A, page 5
V_j	axial velocity component in slipstream, Sketch A, page 5
x, x_s	axial distances defined in Sketch B, page 7
y	distance from duct wall within the duct boundary layer
α	free-stream angle of attack, Sketch A, page 5
β	propeller blade pitch angle measured at the blade tip for the 4-foot propeller and at 3/4 blade radius for the 7-foot propeller

γ strength of vortex cylinder extending from duct trailing edge, Sketch A, page 5

γ_D axially symmetric component of duct-bound vorticity, Equation (17)

γ_α component of duct bound vorticity proportional to $\cos \phi$, Equation (20)

ρ free-stream density

δ^* displacement thickness of duct boundary layer, $\int_0^\infty \left(1 - \frac{u}{u_s}\right) dy$

δ_e deflection angle of elevon, degrees

ν kinematic viscosity of air

Δp rise in static and total pressure across actuator disk, $T_{P(D)}/A_P$

$\epsilon, \epsilon_e, \epsilon_t$ slope of duct camberline, effective slope, effective slope due to duct thickness, Equations (11) and (13)

θ transformed axial distance, $x_s = -(c/2)\cos \theta$, Sketch B, page 7 or momentum thickness of duct boundary layer, $\int_0^\infty \frac{u}{u_s}\left(1 - \frac{u}{u_s}\right) dy$

ϕ azimuthal angle, Sketch B, page 7

Subscripts

DP for the ducted propeller combination

D(P) for the duct in the presence of the propeller (or actuator disk)

ℓ laminar

max maximum

P for the propeller

P(D) for the propeller (or actuator disk) shrouded by the duct

sep	separation
t	turbulent

PREDICTED AND MEASURED PERFORMANCE OF TWO FULL-SCALE DUCTED PROPELLERS

By A. R. Kriebel and M. R. Mendenhall
Vidya Division, Itek Corporation

SUMMARY

A theoretical study was made of the ability of previously developed theory for a ducted propeller at angle of attack to predict duct-to-propeller thrust ratio, normal force, and pitching moment. The theoretical predictions were extended to include duct pressure distribution, boundary-layer characteristics, and duct stall boundary. The methods were evaluated by use of wind-tunnel data for two large-scale ducted propeller models. Data available consisted of overall thrust, normal force and pitching moment, duct surface pressure distribution, total pressure surveys at three axial stations in the duct, and a duct stall boundary deduced from tufts, sound, and pitching moment data.

The experimental data indicated that the flow over a ducted propeller at angle of attack is very complex, with much free vorticity generated by nonuniform blade loading and flow separation from the duct and centerbody. On the basis of the extended theory and data, an analytical model was developed which represents the propeller as a uniformly loaded actuator disk and the duct as a thin cylinder for purposes of computing forces and moments and as a thick, cambered ring airfoil for computing duct pressures and boundary layers. Based on this model, duct thrust and pitching moments were computed which agreed well with measured results. Reasonable agreement on duct normal force was obtained for one model. A considerable over-prediction of measured normal force was obtained with the second model, which is felt to be due to the highly nonuniform blade loading. Predicted duct pressure distributions for both axial flow and angle of attack were generally reasonably accurate, with the greatest differences occurring on the windward inner surface. Predicted boundary-layer separation on the windward inner duct surface correlated reasonably well with experimental indications of duct lip stall at angle of attack.

INTRODUCTION

A theoretical aerodynamic analysis of a ducted propeller at angle of attack is presented in References 1 and 2. This potential flow analysis can be used to predict the force and moment on the duct in terms of the propeller thrust. The usefulness of any theory is dependent on evaluation by comparison with valid data. Much of the previous data (summarized in Ref. 1) are restricted to hovering or axial flight and/or low Reynolds number with flow separation from the duct. Full-scale test data for two ducted-propeller configurations at angle of attack, presented herein, allow a correlation study and a good evaluation of the potential flow theory. The duct force and moment are predicted by use of Reference 2 and compared with experiment. The analysis is extended to predict the duct pressure distribution which is also compared with experiment. Duct boundary-layer separation is predicted and compared with a duct stall boundary deduced from experimental performance.

The analysis is based on a combination of two previous potential flow theories for a ring-wing at a small angle of attack, Reference 3, and for a lightly loaded ducted propeller in axial flow, Reference 4. In Reference 2, the duct thrust, normal force, and pitching moment were predicted by representing the propeller as a uniformly loaded actuator disk. Estimates of the normal force and pitching moment on propeller blades operating in a duct were small compared with those on the duct. Small amounts of duct taper, camber, and thickness were estimated to have little effect on the duct force and moment; hence, the duct is represented herein as a thin cylinder to predict its force and moment.

For comparison with test data, the theory is used to predict the thrust, normal force, and pitching moment on the cylinder in terms of the measured total thrust (on both the disk and cylinder). The predicted duct thrust is then compared with the value deduced from the measured duct pressure distribution. The predicted duct normal force and pitching moment are compared with the values measured for the ducted propeller unit.

EXPERIMENTAL PROGRAM

Two full-scale ducted propellers were tested at angle of attack in the NASA Ames Research Center 40- by 80-foot wind tunnel. The first of these

was an exact duplicate of those used on the Doak VZ-4DA airplane. This unit, which is referred to herein as the 4-foot model, consists of a duct with a chord-to-diameter ratio of 0.608 and a profile thickness-to-chord ratio of 0.158; an eight-bladed propeller with fixed blade pitch of 15° at the tip; a set of seven inlet guide vanes of variable pitch; and a set of nine stators aft of the propeller. A photograph and a sketch of the cross section of this ducted propeller are shown in Figures 1(a) and 2(a). Complete details of the 4-foot model and the test methods are described in Reference 5. The second unit tested was a model of the ducted propellers used on the Bell X22-A VTOL airplane. It was mounted on the tip of a stub wing. This unit, referred to as the 7-foot model, consists of a duct with a chord-to-diameter ratio of 0.525 and a profile thickness-to-chord ratio of 0.172; a three-bladed variable pitch propeller; and six streamlined support struts aft of the propeller. For some of the tests, an elevon extended across the duct exit plane with a thickness of 0.44 foot and a chord of approximately 5 feet. A photograph and a sketch of the cross section of this model are shown in Figures 1(b) and 2(b). The test setup and techniques were similar to those used with the 4-foot model.

For the 4-foot model, the data included direct measurement of lift, drag, and pitching moment reported in Reference 5 and duct surface pressure at 27 orifice stations around the duct profile at each of 10 azimuth locations, Figure 3(a). Total pressure was measured along the duct radii directly ahead of the inlet vanes, directly behind the propeller, and across the duct exit plane with pressure rakes at 10 azimuth locations, Figure 3(b). The duct surface pressures and rake total pressures were integrated to obtain duct forces and moments and propeller thrust.

Data for the 7-foot model included direct measurements of forces and moments and duct surface-pressure measurements at 19 orifice stations around the duct profile for 3 azimuth locations, Figure 3(c). Since the duct pressure data were taken at only 3 azimuth locations, pressure integrations were made to obtain duct thrust only at zero angle of attack.

In addition to the data described above, stalling of the 4-foot model duct was deduced from observation of tufts, sound level, and pitching moment as described in Reference 5.

METHOD OF PREDICTION

Potential Flow Model

For a ducted propeller at angle of attack, the analysis of Reference 2 predicts the thrust, normal force, and pitching moment on the duct in terms of the propeller thrust. The analysis represents the propeller and stator blading and the centerbody as a uniformly loaded actuator disk. There is no swirl in the slipstream, and the circulation about each propeller and stator blade is assumed to be invariant with radius and time. The boundary layer and frictional drag of the duct are neglected. The ducted propeller is assumed isolated in the free stream.

Calculative examples were run to investigate the effects of duct camber, radial variation of disk loading, and duct skin friction in order to arrive at a simple, yet realistic analytical flow model. The work is described in more detail in Appendices A and B. As a result of this work, the following assumptions were employed:

(a) The actuator disk loading is applied only to the annular area swept out by the propeller blades and not to the aft part of the centerbody or inner duct surface.

(b) The duct thrust is taken as that due to leading-edge suction on a thin cylinder.

(c) The effects of duct camber and thickness are neglected except in computing the duct pressure distribution and boundary layer. (It is shown in Ref. 2 that this is a good approximation for the duct force and moment.)

(d) The propeller and stators are represented as a uniformly loaded actuator disk. The centerbody, support wing, and elevon are neglected.

To predict duct pressure and velocity distributions and boundary layers, it was necessary to use a duct profile thickness distribution. The duct profiles for the two ducts do not correspond to any standard airfoil section. However, it was found that the NACA 0018 is a good approximation to the actual thickness distribution of both configurations, particularly over the forward portion of the airfoil where the pressure distribution is of greatest interest.

Duct Force and Moment

To predict the duct force and moment, the duct is represented as a thin cylinder through the actual duct trailing edge as shown in Sketch A.

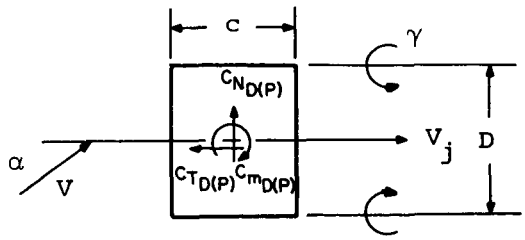

Sketch A.- Flow model for predicting duct force and moment.

All the trailing vorticity is placed on the extension of the cylinder. This approximation requires the free-stream crossflow to be small compared with the slipstream velocity ($V \sin \alpha \ll V_j$). The pressure jump across the actuator disk Δp is equal to the increased total pressure in the slipstream as given by

$$\frac{\Delta p}{q} = \frac{V_j^2}{V^2} - 1 = \left(\frac{V \cos \alpha + \gamma}{V}\right)^2 - 1$$

$$= 2\frac{\gamma}{V} \cos \alpha + \frac{\gamma^2}{V^2} - \sin^2\alpha \qquad (1)$$

The propeller thrust is taken as

$$T_{P(D)} = A_P \Delta p \qquad (2)$$

where A_P is the annular area swept out by the propeller blades. Hence, the propeller thrust coefficient is

$$C_{T_{P(D)}} = \frac{T_{P(D)}}{Aq} = \frac{A_P}{A} \cdot \frac{\Delta p}{q} \qquad (3)$$

The coefficients for the duct force components and pitching moment are given by Equations (20) through (23) of Reference 2 as

$$C_{N_{D(P)}} = f_1 \sin\alpha \left(\cos\alpha + f_2 \frac{\gamma}{V}\right) \tag{4}$$

$$C_{T_{D(P)}} = f_3 \sin^2\alpha + f_4 \left(\frac{\gamma}{V}\right)^2 \tag{5}$$

$$C_{m_{D(P)}} = 4 f_5 \sin\alpha \cos\alpha + (f_5 f_6 + f_7) \frac{\gamma}{V} \sin\alpha \tag{6}$$

where the f_n coefficients are given versus the duct chord-to-diameter ratio c/D in Table I, Reference 2.

Use of blade element theory in Reference 2 indicated that the normal force and pitching moment on the propeller are generally small compared with those on the duct. Therefore, we take the coefficients for the ducted propeller unit as

$$C_{T_{DP}} = C_{T_{P(D)}} + C_{T_{D(P)}} \tag{7}$$

$$C_{N_{DP}} = C_{N_{D(P)}} \tag{8}$$

$$C_{m_{DP}} = C_{m_{D(P)}} \tag{9}$$

The strength of the vortex cylinder surrounding the slipstream is found by substituting Equations (1), (3), and (5) into (7) and solving for

$$\frac{\gamma}{V} = -\frac{\cos\alpha}{\frac{A}{A_P} f_4 + 1} + \sqrt{\left(\frac{\cos\alpha}{\frac{A}{A_P} f_4 + 1}\right)^2 + \frac{\frac{A}{A_P} C_{T_{DP}} - \left(\frac{A}{A_P} f_3 - 1\right) \sin^2\alpha}{\frac{A}{A_P} f_4 + 1}} \tag{10}$$

The general procedure for prediction is to determine γ/V from Equation (10) using a measured value of $C_{T_{DP}}$, and then to evaluate the preceding expressions. This value of γ/V is also used to predict the duct surface-pressure distribution and boundary layer.

Duct Pressure Distributions

The duct pressure distribution is obtained by first predicting the bound vorticity and velocity distribution over the thin duct camberline, then including the effect of duct thickness to obtain the surface velocity distribution, and finally using Bernoulli's law to get the duct surface pressure.

The flow model used to predict the duct surface pressure is shown in Sketch B.

Numbers 1 through 4 designate the camberline or duct surfaces indicated.

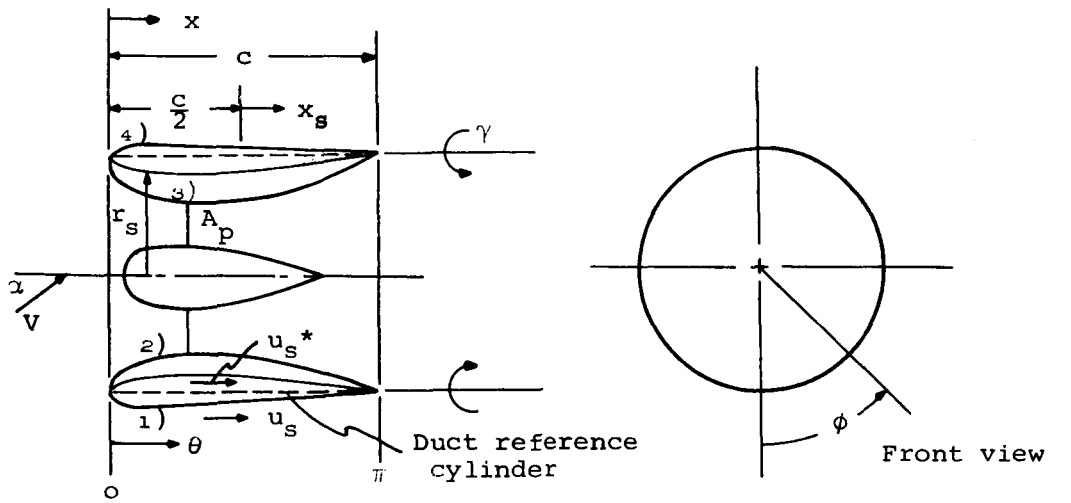

Sketch B.- Flow model for predicting duct pressure distribution.

Duct-bound vorticity.- All the bound and trailing vorticity is placed on a reference cylinder through the duct trailing edge. The distribution of duct-bound vorticity is composed of elementary γ_D vortex rings which are axially symmetric and elementary γ_α rings with strength proportional to $\cos \varphi$. The axially symmetric part of the flow field, composed of $V \cos \alpha$ plus that induced by the γ_D rings and the γ cylinder, is set tangent to the duct camberline. This boundary condition is actually imposed at the duct reference cylinder and it determines the strength of the γ_D rings.

The γ_α rings, together with the axial vortex filaments which trail from them, are required to cancel the velocity across the duct reference cylinder due to the free-stream crossflow $V \sin \alpha$.

The slope of the duct camberline is expressed as a four-term cosine series

$$\epsilon = \frac{dr_s}{dx_s} = \sum_{o}^{3} R_n \cos n\theta \tag{11}$$

where

$$\cos \theta = - \frac{2x_s}{c}$$

Integration gives the duct camberline shape as

$$\frac{r_s - R}{c} = - R_o \left(\frac{1 + \cos \theta}{2} \right) + R_1 \left(\frac{1 - \cos^2 \theta}{4} \right) + R_2 \left(\frac{1}{6} + \frac{1}{2} \cos \theta - \frac{1}{3} \cos^3 \theta \right) + R_3 \left(- \frac{1}{4} + \frac{3}{4} \cos^2 \theta - \frac{1}{2} \cos^4 \theta \right) \tag{12}$$

The R_n coefficients are determined such that Equation (12) fits the geometric camberline at $x/c = 0$, 1/4, 1/2, 3/4, and 1. An effective camber due to thickness ϵ_t is subtracted from Equation (11), as described in Reference 6. This effect is due to the radial velocity induced by the source rings used to generate duct thickness.[1] We take ϵ_t for a NACA 0018 thickness distribution using Equation (44), Reference 6. Thus, the slope of the effective camberline is specified as

$$\epsilon_e = \epsilon - \epsilon_t = \sum_{o}^{3} R_n^* \cos n\theta \tag{13}$$

[1]Evaluation of the axial velocity induced by the source rings from Reference 6 indicates that it is nearly the same as for a straight, two-dimensional wing with the same thickness as the duct. This approximation will be employed in the present analysis.

To set the flow tangent to the camberline, we specify that

$$v_\gamma + v_{\gamma_D} = \epsilon_e \left(V \cos \alpha + u_\gamma + u_{\gamma_D} \right) \tag{14}$$

The u and v terms are the axial and radial velocity components induced along the duct reference cylinder by the γ cylinder extending from the duct trailing edge and the γ_D rings bound to the duct reference cylinder. These terms are expressed as a six-term cosine series as follows. The components induced by the vortex cylinder can be found from Reference 7 in terms of elliptic integrals. Fourier analysis by machine then gives

$$\frac{u_\gamma}{\gamma} = \sum_0^5 B_n^* \cos n\theta \tag{15}$$

$$\frac{v_\gamma}{\gamma} = \sum_0^5 B_n \cos n\theta \tag{16}$$

If the duct-bound vorticity is put in terms of a Glauert series as[2]

$$\frac{\gamma_D}{\gamma} = C_o \cot \frac{\theta}{2} + \sum_1^5 C_n \sin n\theta \tag{17}$$

then the corresponding induced axial velocity component is, from Equation (18), Reference 2

$$\frac{4D}{c} \frac{u_{\gamma_D}}{\gamma} = \left(\ell n \frac{16D}{c} - 1 \right) \left(C_o + \frac{C_1}{2} \right) + \left(C_o + \frac{C_2}{2} \right) \cos \theta + \frac{C_3 - C_1}{4} \cos 2\theta + \frac{C_4 - C_2}{6} \cos 3\theta + \frac{C_5 - C_3}{8} \cos 4\theta \tag{18}$$

[2]Between the actuator disk and duct trailing edge, γ_D includes the vorticity shed from the disk onto the inner duct surface. The Kutta condition of no flow across the duct trailing edge is satisfied because γ_D is non-singular at $\theta = \pi$ in Equation (17).

The radial velocity component can be found from Equation (14) of Reference 4 as

$$\frac{v_{\gamma_D}}{\gamma} = \frac{C_o}{2} - \sum_{\ell=o}^{\infty} \frac{C_\ell}{2} P_{o\ell} + \sum_{k=1}^{\infty} \cos k\theta \left(- \frac{C_k}{2} + \sum_{\ell=o}^{\infty} \frac{C_\ell}{2} P_{k\ell} \right) \qquad (19)$$

The $P_{k\ell}$ coefficients appearing in Equation (19) are evaluated in Tables 2.1 through 2.4 of Reference 4.

The six unknown C_n coefficients appearing for γ_D are determined by: (1) substituting the foregoing cosine series for the terms in Equation (14), (2) expanding the right-hand side as a cosine series, and (3) equating each of the six harmonics of Equation (14). The resulting six linear algebraic equations are then solved by machine for the six C_n. The remaining part of the duct vorticity γ_α is the same as determined by Weissinger for a ring-wing at angle of attack, and is given by Equation (8) of Reference 2 as

$$\frac{\gamma_\alpha}{V \sin \alpha \cos \phi} = c_o \cot \frac{\theta}{2} + \sum_{1}^{5} c_n \sin n\theta \qquad (20)$$

Weissinger's values for the c_n coefficients are given in Table 1, Reference 2. The axial velocity induced by γ_α along the duct reference cylinder is given by Equation (19) of Reference 2 as

$$\begin{aligned} \frac{4Du_{\gamma_\alpha}}{cV \sin \alpha \cos \phi} = {} & \left(\ell n \frac{16D}{c} - 3 \right) \left(c_o + \frac{c_1}{2} \right) + \frac{1.46c}{4D} \left(c_o + \frac{c_2}{2} \right) \\ & + \left[c_o - \frac{1.46c}{4D} \left(c_o + \frac{c_1}{2} \right) + \frac{c_2}{2} \right] \cos \theta \\ & + \frac{c_3 - c_1}{4} \cos 2\theta + \frac{c_4 - c_2}{6} \cos 3\theta \\ & + \frac{c_5 - c_3}{8} \cos 4\theta \end{aligned} \qquad (21)$$

Finally, the velocity distribution over the four duct camberline surfaces shown in Sketch B, page 7, can be evaluated by substitution of preceding expressions into

$$u_s^* = \pm \frac{\gamma_D + \gamma_\alpha}{2} + V \cos \alpha + u_\gamma + u_{\gamma_D} + u_{\gamma_\alpha} \tag{22}$$

where the plus sign refers to the inner surfaces 2 and 3 and the minus sign the outer surfaces 1 and 4. At the sides of the duct, γ_α induces a tangential velocity component. We do not consider this component, since it vanishes at the vertical plane of symmetry, to which we restrict the pressure distribution predictions.

Duct surface velocity.- To obtain the duct surface velocity from the velocity distribution over the camberline (Eq. (22)), we apply corrections to the discontinuous (vorticity) and continuous terms in Equation (22). These correction factors are deduced as follows from theoretical results for two-dimensional (c/D = 0) thick airfoils in Reference 8. For a thin flat plate at angle of attack, the bound vorticity is

$$\frac{\gamma_D}{V} = 2\alpha \cot \frac{\theta}{2} \tag{23}$$

At $\alpha = 1/(2\pi)$, the lift coefficient is unity and

$$\frac{\gamma_D}{2V} = \frac{1}{2\pi} \cot \frac{\theta}{2} \tag{24}$$

This chordwise distribution is listed in Table I for comparison with values for a NACA 0018 airfoil from Reference 8. It is evident that thickness has little effect on the bound vorticity except near the airfoil nose where $x < 0.1c$. Hence, we shall correct the singular ($\cot(\theta/2)$) terms in γ_D and γ_α by replacing $\cot(\theta/2)$ by the corresponding value for a NACA 0018 airfoil when $x < 0.1c$. For example, at the leading edge $(1/2\pi)\cot(\theta/2)$ is replaced by 1.342. The surface velocity distribution for a two-dimensional NACA 0018 airfoil at $\alpha = 0$ is shown in the last column of Table I. In this case, the continuous part of the camberline velocity distribution is V and the continuous part of the surface velocity distribution is $VF(x)$, where $F(x)$ is given by the last column in Table I. By analogy, we shall obtain the continuous part of the duct surface velocity by multiplying

the continuous part of the camberline velocity by $F(x)$. Thus, we obtain the duct surface-velocity distribution from the duct camberline distribution (Eq. (22)) as

$$u_s = \pm\left(\frac{\gamma_D + \gamma_\alpha}{2}\right)_c + \left(V \cos \alpha + u_\gamma + u_{\gamma_D} + u_{\gamma_\alpha}\right) F(x) \qquad (25)$$

where the subscript c on the first parenthesized term indicates that the term is corrected only when $x < 0.1c$, as described previously.

Duct pressure distribution.- The duct surface-pressure coefficient is obtained from Equation (25) by Bernoulli's law as

$$C_p = 1 - \frac{u_s^2}{V^2} \qquad (26)$$

However, on the inner duct surface downstream of the actuator disk, the total pressure is increased by Δp and C_p is increased by $\Delta p/q$ due to the pressure jump across the disk.

Duct Boundary-Layer Model and Assumptions

Our purpose in computing the duct boundary layer is to predict those conditions under which separation occurs on the windward inside surface before the propeller. We use the axisymmetric Truckenbrodt method to obtain the momentum thickness (θ) and shape factor (H) of the boundary layer and then use an empirical rule ($H = 1.8$) to predict turbulent separation.

The Truckenbrodt method (Ref. 9 or 10) was compared to known results in both laminar and turbulent flow and found to give excellent agreement. We computed the laminar boundary-layer parameters for Howarth flow on a flat plate and found agreement to within 5 percent of the exact Howarth solution. Also, turbulent boundary-layer parameters were computed for a NACA 65(216)-222 profile at 10.1° angle of attack using the measured velocity distribution, as obtained from Reference 11. The computed momentum thickness, shape factor, and separation point all agree well with measured results presented therein.

We make use of the following assumptions in calculating the duct boundary layers:

(1) The boundary-layer momentum thickness is small in comparison with the duct radius so that the presence of the boundary layer does not appreciably alter the potential flow around the duct.

(2) The predicted surface velocity (Eq. (25)) is taken as the boundary-layer-edge velocity distribution.

(3) The velocity profiles in the boundary layer are approximated by a one-parameter family of curves.

As a transition criterion, it is assumed that the boundary layer changes from laminar to turbulent at a Reynolds number of about 400 based on momentum thickness and local surface velocity.[3] In cases with high adverse pressure gradients near the leading edge, the laminar boundary layer separated ($H = 4.04$) before $Re_\theta = 400$. In these cases, it was assumed that the separated region acts as a turbulence trip, and the point of transition was located at the first indication of laminar separation. In Reference 12, it is reported that small laminar separation bubbles on ring wings, which did not show up in the pressure distribution, did serve as turbulence trips.

The shape factor (H) is used to estimate the location of boundary-layer separation from the duct. The usual criteria for boundary-layer separation is that turbulent separation occurs when H has attained a value between 1.8 and 2.4, and laminar separation occurs when $H = 4.04$.

The Truckenbrodt solution to the boundary layer is based on integration of the energy equation. The energy equation is written in the form

$$\frac{1}{2}\frac{1}{u_s^3 r_s}\frac{d}{dx}\left(u_s^3 r_s \delta^{**}\right) = \frac{d + t}{\rho u_s^3} \tag{27}$$

where δ^{**} is the energy thickness of the boundary layer, d is the dissipation term, and t is the energy of turbulent motion term. The right side of Equation (27) is the shear stress work in the boundary layer.

---

[3]The transition criterion is based on a measured critical Reynolds number on a flat plate, $Vx/\nu = 3\times10^5$ (Ref. 10). This corresponds to $V\theta/\nu \approx 365$ in a laminar boundary layer on a flat plate. Since the location of turbulent separation is insensitive to small variations in transition location, transition was assumed to occur when $350 < u_s\theta/\nu < 425$.

Truckenbrodt's final expression for momentum thickness as a function of boundary-layer-edge conditions is

$$\frac{\theta(z)}{s} = \frac{1}{\left(\frac{u_s}{V}\right)^3\left(\frac{r_s}{s}\right)}\left[c_1^* + \left(\frac{c_{f_t}}{2}\right)^{1+n}\int_{z_1/s}^{z/s}\left(\frac{u_s}{V}\right)^{3+2n}\left(\frac{r_s}{s}\right)^{1+n} d\left(\frac{z}{s}\right)\right]^{1/1+n} \tag{28}$$

where

$$c_1^* = \left\{\frac{c_{f_\ell}}{2}\left[\int_0^{z_1/s}\left(\frac{u_s}{V}\right)^5\left(\frac{r_s}{s}\right)^2 d\left(\frac{z}{s}\right)\right]^{1/2}\right\}^{1+n}$$

c_{f_ℓ} = laminar flat-plate drag coefficient from the Blasius relation, based on q and s

c_{f_t} = turbulent flat-plate drag coefficient from the Schultz-Grunow relation, based on q and s

$n = 1$ for laminar flow

$n = 1/6$ for turbulent flow

The actual calculation of momentum thickness is carried out in a surface coordinate system where z is measured from the leading edge along the surface of the duct and s is the surface length of the duct. The point of transition of the boundary layer from laminar to turbulent is denoted by z_1. After the boundary layer is computed in the surface coordinate system, the results are transferred into a coordinate system based on axial distance x and chord length c.

Boundary-layer parameters were computed on the inside surface of both ducts using measured and predicted velocity distributions. Computation of these parameters using the measured velocity distribution was started at the leading edge. When the predicted velocity distribution was used to compute the boundary-layer parameters, the computation was started either at the leading edge or at the stagnation point on the outside surface.

RESULTS

The predicted force and moment coefficients are given by Equations (3) through (10) in terms of the parameters A_p/A, c/D, and f_n. Values for these parameters are listed in Table II for both ducts. The f_n are found by interpolation from Table 1, Reference 2. The total measured force and moment coefficients are deduced from force balance data. Individual measured duct and propeller thrust coefficients are determined from integrations of measured pressure distributions over the duct surface and total pressure rake data before and just aft of the propeller.

Division of Thrust in Axial Flow

Four-foot model.- For a series of axial flow runs with the 4-foot model duct, the measured thrust coefficients are listed in Table III. The sum of the individual duct and propeller measured thrusts ($C_{T_{D(P)}}$ and $C_{T_{P(D)}}$) is equal to the total measured thrust $C_{T_{DP}}$ within 7 percent. The values of γ/V and $C_{T_{D(P)}}$ predicted from the measured $C_{T_{DP}}$ are listed next. Finally, the values of γ/V and $C_{T_{D(P)}}$ predicted from the measured $C_{T_{P(D)}}$ are shown. The latter values are obtained by use of Equations (3), (1), and (5), in succession, rather than by the usual method (Eqs. (10) and (5)).

Seven-foot model.- Measured values of $C_{T_{DP}}$ and $C_{T_{D(P)}}$ are shown in Table III together with the predicted values of $C_{T_{D(P)}}$. The effect of elevon removal is shown by comparison of the first two groups of runs. The effect of changing propeller blade pitch is indicated by the last two groups of runs.

Duct Force and Moment at Angle of Attack

Four-foot model.- Normal force, duct thrust force, and pitching moment coefficients predicted versus the total thrust coefficient are shown in Figures 4, 5, and 6, together with measured force-balance values. The data generally lie below the predicted curves, particularly the normal-force coefficient. The measured duct normal force (deduced from the pressure distribution) is considerably smaller than the measured total normal force, as shown in Table IV.

Seven-foot model.- Similar predicted and measured coefficients for the larger duct are shown in Figures 7 and 8. The data are all for the same propeller pitch and with the elevon either off or aligned with the duct axis. In this case, the data tend to lie above the predicted values. The elevon appears to have most effect on the measured normal force at the highest angles of attack.

Duct Pressure Distributions in Axial Flow

Following the procedure described previously, the first step in predicting the duct pressure distribution is to fit Equation (12) to the duct camberline and solve for the four camberline coefficients R_n. The computed values for R_n are given in Table II for both ducts. The thickness distributions for both ducts were approximated by a NACA 0018 profile. The resulting duct profiles are compared with actual profiles in Figure 9. The analytical profiles fit the nose radius of curvature for both ducts. However, the hook in the camberline near the leading edge of the larger duct is not well represented. Attempts to fit the hook with the four-term series caused a very poor fit over most of the camberline.

The effective camber due to thickness (ϵ_t in Eq. (13)) is given by Reference 6 for a NACA 0008 profile and $c/D = 1/2$. Multiplication by 18/8 gives, for a 0018 profile and $c/D = 1/2$,

$$\epsilon_t = 0.001 + 0.040 \cos \theta + 0.013 \cos 2\theta - 0.001 \cos 3\theta$$

This distribution was used for both ducts. The resulting R_n^* coefficients for the effective camberline (Eq. (13)) are given in Table II.

Fourier analysis by machine gives the series coefficients B_n and B_n^*, which appear in Equations (15) and (16) for the velocity components induced by the vortex cylinder trailing from the duct. Machine computed values are given in Table V for the two ducts.

The $P_{k\ell}$ coefficients which appear in Equation (19) are found by interpolation from Tables 2.3 and 2.4 of Reference 4. Values for the two ducts are given in Tables VI and VII.

The C_n coefficients in Equation (17) for the duct-bound vorticity γ_D must be computed for each case since they depend upon γ/V. However, for no duct camber ($R_n^* = 0$) the C_n depend only upon c/D, and these values are given in Table V.

The c_n coefficients in Equation (20) for the duct-bound vorticity γ_α can be found by interpolation from Table 1 of Reference 2. Values for the two ducts are given in Table V.

Four-foot model.- Duct pressure distributions computed for the smaller duct in axial flow are shown in Figure 10 at four thrust levels. Measured data are shown by the vertical lines to indicate the variation with azimuth. The discontinuous change in predicted pressure on the inner duct surface is caused by the pressure jump across the assumed uniformly loaded actuator disk.

Actual propeller disk loadings were obtained by measuring total pressure distributions in a plane just downstream of the propeller and in the duct exit plane. Results for two advance ratios, shown in Figure 11, indicate quite nonuniform loadings. The influence of nonuniform disk loading on duct pressure distribution is discussed in Appendix A.

Seven-foot model.- For a series of axial flow runs, the measured and predicted duct pressure distributions are shown in Figures 12, 13, and 14. Figures 12 and 13 show the influence of elevon removal, and Figures 13 and 14 indicate the effect of changing blade pitch. As before, the pressure jump across the uniformly loaded actuator disk appears as a discontinuity in the duct surface pressure.

Duct Pressure Distributions at Angle of Attack

Four-foot model.- Measured and predicted pressure distributions at angle of attack for three advance ratios are shown in Figures 15, 16, and 17. The pressures shown are all in the plane of symmetry[4] except the measured pressures on duct surfaces 3 and 4 in Figure 15, which are at an azimuth station 30° off the plane of symmetry. In order to clarify the figures, the data points are shown only for the windward inner surface (surface 2). Since the actuator disk is assumed to be uniformly loaded, the same pressure jump across the disk acts on both inner surfaces.

---

[4] That plane through the duct centerline which contains the freestream velocity vector. For the tests described herein, the ducted propeller models were rotated about a vertical axis in the tunnel to get an "angle of attack" flow condition; thus, the plane of symmetry in the test models is a horizontal plane through the duct centerline (see Fig. 1).

Radial distributions of total pressure at the duct exit in the plane of symmetry are shown in Figure 18 for two advance ratios. These data show that the propeller loading was not uniform and that the flow was separated from the windward inner duct surface (surface 2) aft of the propeller for angles of attack greater than approximately 20°.

Seven-foot model.- Pressure distributions measured and predicted for the 7-foot model duct at angle of attack are shown in Figures 19 and 20 for two advance ratios. The effect of angle of attack at a high advance ratio is shown in Figures 19 and 12(b); and at a low advance ratio in Figures 20 and 12(e). All the data at angle of attack were taken 13° off the plane of symmetry (see Fig. 3(c)).

Duct Boundary-Layer Calculations

With the foregoing duct surface geometry and both measured and predicted surface-pressure distributions, duct boundary layers were computed using the method previously described. Bernoulli's equation was used to relate surface velocity and pressure distributions. The boundary layers were computed only on the lower inner surface[5] of the computed duct profile back to the propeller station.

Four-foot model.- For the smaller duct in axial flow at various advance ratios, the computed boundary-layer momentum thickness, shape factor, and surface-velocity distributions are shown in Figure 21. The computation was started at the leading edge where the momentum thickness was assumed zero in each case. Transition was governed by the assumed Re_{θ} criterion in all cases except $J = 0.178$ with the predicted velocity distribution, where laminar separation triggered transition.[6] The turbulent boundary layers computed from the predicted velocity distributions did not show separation from the duct ahead of the propeller. However, when the measured velocity distribution was used for the computation for the hovering flight condition ($J = 0$) and a second high thrust condition ($J = 0.178$), the boundary layer was predicted to separate slightly ahead of the propeller.

---

[5]The computed duct shape is the superposition of a NACA 0018 thickness distribution on the duct camberline shape from Equation (12).

[6]Since a stepwise numerical integration scheme was used to compute boundary-layer growth, a chordwise station where $Re_{\theta} = 400$ exactly was rarely found, which accounts for the variation of transition Re_{θ} shown.

For non-zero angles of attack at $J = 0.178$, the predicted boundary-layer characteristics are shown in Figure 22. Figure 22(a) shows predicted surface velocity distribution, momentum thickness, and shape factor for angles of attack of 20° and 40°. The boundary layers were computed from the stagnation point on the outside surface at $x/c = 0.1$ for $\alpha = 20^{\circ}$ and $x/c = 0.15$ for $\alpha = 40^{\circ}$, using the predicted velocity distributions. Neither boundary layer was predicted to separate upstream of the propeller. The results for $\alpha = 60^{\circ}$ are shown in Figure 22(b) for both measured and predicted velocity distributions. In addition, for the predicted velocity distribution, boundary-layer computations were made starting at the leading edge and at the stagnation point ($x/c = 0.45$ on the outside surface). The starting point made very little difference in the computed boundary-layer characteristics. Separation was predicted to occur for all cases at $\alpha = 60^{\circ}$. Similar results for $\alpha = 80^{\circ}$ are shown in Figure 22(c). For $\alpha \geq 60^{\circ}$, separation was predicted to occur further forward with the predicted than with the measured velocity distributions.

For a higher advance ratio ($J \simeq 0.34$) the effect of angle of attack on the duct boundary layer is shown in Figure 23. Using the predicted velocity distribution for $\alpha = 0^{\circ}$, 20°, 40°, and 60°, the boundary layers were computed from the leading edge. Turbulent boundary-layer separation was predicted only when $\alpha = 60^{\circ}$. Using the measured velocity distribution for $\alpha = 0^{\circ}$, the turbulent boundary layer was predicted to separate slightly ahead of the propeller.

The results at the highest advance ratio considered ($J \simeq 0.54$) are shown in Figure 24. At $\alpha = 0^{\circ}$, the boundary layer computed from the leading edge using both measured and predicted velocity distributions did not separate before the propeller. At $\alpha = 20^{\circ}$ and 40°, the predicted velocity was used to compute the boundary layer from the stagnation points on the outer surface at $x/c = 0.03$ and 0.05, respectively. At $\alpha = 40^{\circ}$, the boundary layer was also computed from the leading edge using the measured velocity. The turbulent boundary layer was predicted to separate only with the measured velocity for $\alpha = 40^{\circ}$.

Seven-foot model.- The momentum thickness and shape factor for the larger duct in axial flow at several advance ratios are shown in Figure 25. The boundary layers for all advance ratios were computed from the leading edge using the measured velocity distribution. At advance ratios below

0.434, the boundary layers were predicted to separate ahead of the propeller. The boundary layer at an intermediate advance ratio ($J = 0.216$) was also computed from the leading edge using the predicted velocity distribution, but it did not separate.

For a number of angles of attack at a high advance ratio ($J \simeq 0.52$), the predicted boundary-layer momentum thickness, shape factor, and surface velocity distribution are shown in Figure 26(a). Using predicted velocity distributions, the boundary layers were computed from the leading edge at $\alpha = 0^\circ$ and 20°, and from $x/c = 0.05$ near the outside stagnation point at $\alpha = 40^\circ$. No separation was indicated. The measured velocity distribution was also used for computations at $\alpha = 0^\circ$ and 40°. Only for the last of these computed boundary layers was separation predicted. One can note from the measured pressure distribution for this last case (Figure 19(b)) that a strong indication of separation is evident at $x/c \simeq 0.05$.

Since turbulent separation was not obtained at 40° with the predicted velocity distribution, this case was repeated assuming transition did not occur. Laminar separation was then predicted to occur (at $x/c = 0.02$ and $Re_\theta = 500$) when the boundary layer was started both at the stagnation point and at the leading edge.

For a lower advance ratio ($J \simeq 0.21$), the boundary layers computed at $\alpha = 20^\circ$ and 40° are shown in Figure 26(b). Measured velocity distributions were used, and separation was predicted forward of the propeller in both cases.

Duct stall boundary.- A summary of all of the boundary-layer separation predictions on the smaller duct is shown in Figure 27(a). The purpose of this presentation is to attempt to compare predicted separation results with the only data available: an observed stall boundary from Reference 5. Each point in Figure 27(a) represents a test condition at the appropriate angle of attack and advance ratio. The chordwise location of the predicted separation point, based on either measured or predicted velocity distribution, is noted beside each point. The upper dashed curve is the boundary corresponding to separation midway between the leading edge and the propeller station ($x/c \simeq 0.15$). This boundary is estimated from the points computed with measured velocity distributions. The other dashed curves correspond to separation at other values of x/c, as estimated from the computed points. The solid curve is the experimental stall boundary deduced from measured

pitching moment, sound levels, and observation of tufts on the inner duct lip (Ref. 5).

A summary of predicted boundary-layer separation results for both ducts for axial flow is shown in Figure 27(b). The chordwise location of the predicted separation points, based on measured velocity distributions, is shown as a function of total ducted propeller thrust.

All of the computed separation points on both ducts are shown in Figure 28. The points are plotted versus a Reynolds number based on a length ℓ obtained as indicated in Sketch C and Figure 28. The maximum value of u/u_{max} is translated to the ordinate ($x = 0$) and a straight line is drawn from this point through the known separation point on the curve. The intercept on the abscissa is the length ℓ.

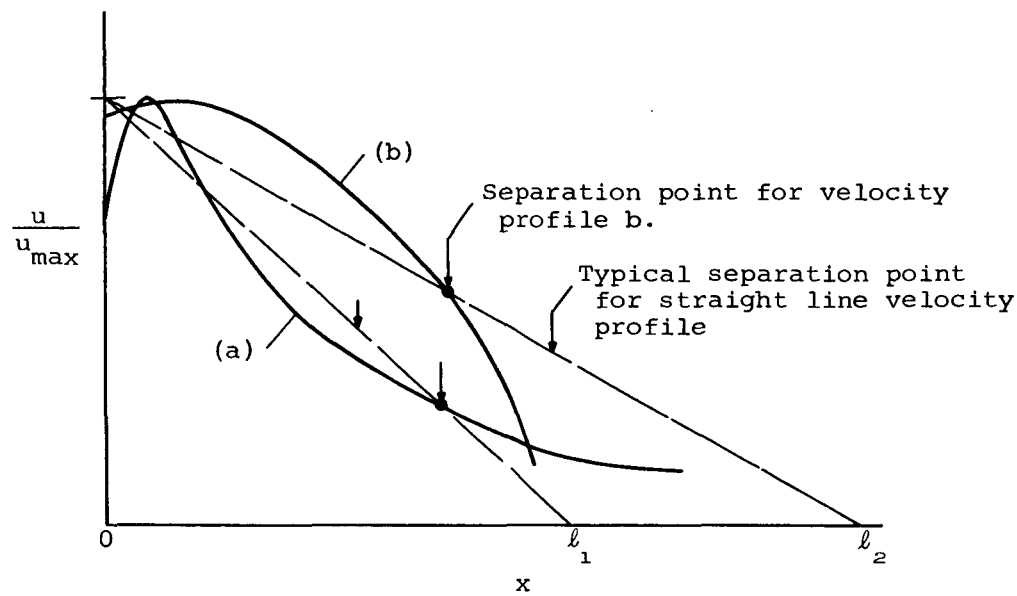

Sketch C.- Linear approximation to duct velocity distributions.

If linear velocity profiles are used with the Truckenbrodt method to compute the location of separation, the solid line in Figure 28 is obtained. This line shows that the separation points for a series of straight line velocity profiles, computed by the Truckenbrodt method as before, are all at nearly a constant velocity ratio, $u_{sep}/u_{max} \simeq 0.65$. The points on Figure 28 which lie below the solid line are for velocity

profiles which are convex downward, for example, curve (a) in Sketch C, or the dashed curve in Figure 22(c). On the other hand, the points which lie above the curve are for convex upward profiles such as curve (b) in Sketch C, or the dashed curve in Figure 23.

DISCUSSION

Division of Thrust in Axial Flow

The 4-foot model duct thrust predicted both from the measured total thrust and the measured propeller thrust (Table III) agrees with the measured value within +10/-12 percent. This agreement seems satisfactory in view of the fact that the theory neglects the observed nonuniformity of propeller blade loading and the prevalence of flow separation from the duct diffuser in addition to many other real effects.

For the 7-foot model duct in axial flow, the measured duct thrust generally exceeds the predicted value (Table III). The flow separated from the inner duct surface upstream of the propeller when $C_{T_{DP}} > 2$ according to the boundary-layer predictions using the measured pressure distributions (Fig. 27(b)). The predictions did not account for the hook in the duct camberline near the leading edge or the duct frictional drag. However, calculations indicate that both of these effects are appreciable only at low thrust levels (Appendices A and B). Calculations also indicate that the thrust on the 7-foot model (but not the 4-foot model) duct is predicted more accurately when the pressure rise across the actuator disk is assumed to act on the aft part of the inner duct surface (Appendix A).

Duct Force and Moment at Angle of Attack

The thrust on the smaller duct at angle of attack is reasonably well predicted (Fig. 5). The measured duct thrust was almost independent of angle of attack.

The main difference between the measured and predicted performance of the two ducted propellers is the normal force at angle of attack. The measured values of normal force for the 4-foot model duct (Fig. 4) are generally much smaller than for the 7-foot model duct (Fig. 7), particularly at high thrust levels, even though the two duct configurations are very similar. The predicted normal force is nearly the same for the two ducts

and generally in good agreement with the data for the larger duct without the elevon (Fig. 7(a)). The data and predictions both indicate that there was considerable flow separation from the 4-foot model duct at angle of attack. However, it is felt that the very low normal force measured for the smaller duct at high thrust level was caused largely by the concentration of propeller thrust loading toward the hub. Except for this effect, one might expect the normal force on the smaller unit to be greater than predicted for the duct alone because of the large centerbody and large number of stator and propeller blades. Theoretical estimates[7] indicate that concentration of the propeller loading toward the hub does cause the duct normal force to decrease significantly at high thrust level but has little effect on the duct thrust.

For the 7-foot model, the addition of the elevon (aligned) has the effects of increasing measured normal force at high angles of attack and decreasing it at low angles of attack (Fig. 7). The predicted normal force, which does not consider the elevon, agrees better with the elevon-off data, as might be expected. The most probable reason for the underprediction of normal force on the larger unit is the existence of normal force components on the blading, centerbody, and elevon (if present) which are not predicted by the theory. Only that component acting on the duct is shown in Figure 7. This tends to be borne out by Table IV, which indicates measured duct normal forces lower than measured overall normal forces for the 4-foot unit.

The measured pitching moment results for both ducts are consistent with the normal force results, in that higher moments are obtained with the larger than with the smaller duct. The pitching moment appears to be well predicted for both ducts (Figs. 6 and 8).

Duct Pressure Distributions in Axial Flow

The pressure distributions for the 4-foot model duct (Fig. 10) appear to be reasonably well predicted. At the higher thrust levels, and particularly for the hovering flight condition, the pressure on the inner duct surface aft of the propeller is lower than predicted. This is probably due to the fact that the propeller loading is concentrated near the hub so that the full disk pressure jump is not applied suddenly to the duct surface.

[7] Kriebel, A. R.: Investigation of Dynamic Stability Derivatives of Ducted Propellers, 1st Quarterly Progress Rpt., Vidya Project No. 9270, Contract NOw 65-0348-c, June 1965.

The pressure distributions for the larger duct (Figs. 12 through 14) are accurately predicted on the outer surface. However, on the more critical inner surface, the pressure is predicted less accurately than for the smaller duct. This is particularly true when the blade pitch and thrust coefficient are high (Fig. 14). Although the presence of the elevon appears to have little effect on the duct pressure distribution (Figs. 12(c) and 13(c)), increased blade pitch at a fixed thrust lowers the measured pressure over the inner duct surface (Figs. 12(d) and 14(a)). The effect is complicated by the fact that separation of the boundary layer slightly ahead of the propeller was computed for all of the measured pressure distributions shown at the higher blade pitch. Such separation and possible reattachment after the propeller would probably be affected by the loading of the propeller blade tips.[8]

The discontinuity in duct pressure predicted for a uniform actuator disk loading is not evident from the data for either ducted propeller. This can be attributed to the low loading of the propeller blade tips for the smaller unit as mentioned earlier. For the larger unit the blade tips were apparently more highly loaded, but the computed duct boundary layer separated near the propeller except when the blade loading was low. The separation of the duct boundary layer may have caused the pressure discontinuity on the inner duct wall to be smoothed out similar to a shock wave-boundary layer interaction. The predicted pressure gradient on the inner duct surface can be improved by smoothing out the theoretical discontinuity across the actuator disk.

Duct Pressure Distributions at Angle of Attack

The predicted pressure distributions at angle of attack are in overall qualitative agreement for both ducts (Figs. 15, 16, 17, 19, and 20). However, the accuracy is poorest on the most critical surface 2. For surface 2 the pressure is underpredicted more for the smaller than for the

[8] Recently, rake data were obtained on the 7-foot model approximately 10 inches upstream of the duct exit for $\alpha = 0^{\circ}$, $\beta = 29^{\circ}$, $J = 0$, 0.22, 0.45, 0.62. The measured total pressure was very uniform for each one of these runs except within the duct boundary layer (about 2 in. thick) and toward the centerline ($r \leq 18$ in. where $\Delta p \simeq 0$). The low dynamic head in the central part of the slipstream is believed to have: (1) caused the velocity over the inner duct surface to be higher than predicted, and (2) reduced the effectiveness of the elevon.

larger duct. This is in agreement with the fact that the normal force on the smaller duct was overpredicted whereas the normal force on the larger model was not. Duct flow separation for the 4-foot model is not evident from any of the measured pressure distributions (Figs. 15, 16, and 17). For the smaller duct the inaccuracy of prediction is ascribed to the influence on the overall theoretical flow model of flow separation from the duct aft of the propeller and the nonuniformity of the propeller loading.

For the larger duct at low thrust coefficient (Fig. 19(a)), the pressure gradient on the uppermost surface 4 is more adverse than predicted. This is believed to be caused by the hook near the leading edge of the actual camberline (Fig. 9) which cannot be accurately represented by the four-term series expression for the camberline. The corresponding suction peak is much smaller for the smaller duct. As the angle of attack is increased to 40° in Figure 19(b), the flow separates from surface 4. The flow is also separated from surface 2 in Figure 19(b) as shown by the measured pressure distribution.

At higher thrust coefficient (Fig. 20), the stagnation point moves onto surface 4 and the pressure gradient becomes favorable. The computed separation on surface 2 was near the propeller (Fig. 26(b)) and the separation bubble did not appear in the data for $\alpha \leq 40^{\circ}$. Hence, the predicted pressure distributions are relatively accurate.

Duct Boundary-Layer Calculations

Comparison of measured and predicted pressure distributions.- The boundary layers computed for both ducts using predicted pressure distributions (Figs. 21 through 26) agree reasonably well with those computed from the measured pressures except near the propeller. The predicted pressure gradient is typically less adverse just upstream of the propeller which delays separation of the predicted turbulent boundary layer. The more adverse pressure gradient near the propeller characteristic of the measured pressure distributions causes the momentum thickness to grow more rapidly which in turn causes a more rapid increase in shape factor. In Figures 21, 23, 24, and 25, this difference in pressure gradient causes the boundary layer corresponding to the measured pressure to separate ahead of the propeller while the predicted pressure boundary layer does not. However, when the boundary layer separates farther forward, similar results are

obtained using measured and predicted pressure distributions (Figs. 22(b) and 22(c)).

Starting point.- In Figures 22(b) and 22(c), the boundary layers computed from the leading edge are compared with those computed from the outside surface stagnation point. Up to the leading edge the pressure gradient is highly favorable and the momentum thickness at the leading edge is quite small. There is only a small difference in momentum thickness on the inside surface and negligible difference ($< 0.01c$) between the computed separation points. Therefore, the additional effort required to compute the boundary layer from the stagnation point does not seem required.

Four-foot model.- A summary of all the computed separation points for the smaller duct is shown in Figure 27(a). The dashed curves indicate the location of separation on the windward inner duct surface 2 as estimated from the computed points. These curves are obviously rough estimates because of the small number of points. The upper dashed curve, which can be estimated more accurately than the others, gives the estimated flight conditions (angle of attack versus advance ratio) for separation about midway between the duct lip and propeller ($x/c = 0.15$). The stall boundary deduced in Reference 5 from sound, tuft, and pitching moment data lies somewhat above the upper dashed curve; hence, this stall boundary apparently corresponded to separation very near the leading edge of the duct. The lowest dashed curve indicates that separation is expected to occur before the propeller except for low angle of attack and high advance ratio. The dashed curve for separation at $x/c = 0.24$ indicates that this is the calculated location of separation for hovering flight (any α at $J = 0$) and that there are values of α for $J > 0$ which fix the separation point at $x/c = 0.24$. A "duct stall boundary" could be defined to correspond with a fixed location of separation before the propeller. This boundary would then correspond with any one of the curves indicated in Figure 27(a) depending on the chosen location of separation.

Seven-foot model.- The measured pressure distribution on the duct at $\alpha = 40^{\circ}$ (Fig. 19(b)) indicates a separated region at $x/c \simeq 0.05$. The boundary layer computed from the leading edge using the measured pressure distribution separates at $x/c = 0.032$ (Fig. 26(a)). Since this pressure distribution clearly indicates a separation region, the computed result is encouraging in terms of the method used to predict the boundary layer. No

separation was computed using the predicted pressure distribution, but this distribution was inaccurate because of the flow separation.

Boundary-Layer Separation in Axial Flow

The computed separation points for both ducts in axial flow are compared in Figure 27(b). When the total thrust coefficient is near 20, it can be seen that the boundary layer on the larger duct separates slightly farther forward; however, the larger duct carries a considerably larger fraction of the thrust (Table III). The computed boundary layers on both ducts in axial flow are separated ahead of the propeller when $C_{T_{DP}} > 2$. Without unsteady effects due to finite propeller blades, the boundary layer was computed beyond the propeller for both ducts in axial flow for $C_{T_{DP}} < 2$ using the measured velocity distribution. Separation occurred on the smaller duct at $x/c = 0.65$ for $C_{T_{DP}} = 0.684$ and on the larger duct at $x/c = 0.65$ for $C_{T_{DP}} = 0.890$. Thus, the computed boundary layers on the inner surface of both ducts separate even for thrust coefficients smaller than unity.

Boundary-Layer Separation Summary

The computed separation results for both ducts are compared in Figure 28. The solid line gives the velocity ratio for separation as predicted for a constant adverse velocity gradient indicated in the sketch in Figure 28. The points which lie above the curve are for increasingly adverse velocity gradients such that $u(x)$ is convex upward. The points below the curve are for $u(x)$ curves which are sharply peaked near the leading edge and convex downward. It can be seen that all of the computed separation points lie within a rather narrow band of velocity ratio, $0.6 \leq u_{sep}/u_{max} \leq 0.8$. This approach offers the potential for predicting the location of separation for a typical duct velocity profile rather closely, providing these results can be verified by boundary layer measurements.

CONCLUSIONS AND RECOMMENDATIONS

The ability of previously developed theory for a ducted propeller at angle of attack to predict the duct-to-propeller thrust ratio, the normal force, and the pitching moment was evaluated by use of wind tunnel data for two large-scale ducted propellers. The theoretical predictions were

extended to include the pressure distribution, boundary layer, and stall boundary for the duct.

The experimental data presented herein show that the flow over a ducted propeller at angle of attack is generally very complex with much free vorticity generated by nonuniform blade loading and separation of the flow from the duct and centerbody. Specifically, the rake data for the 4-foot model show that the blade loading was concentrated near the hub and that the flow was generally separated from the inner duct surface.

The theoretical flow model concentrates the free vorticity into a thin duct boundary layer and a single vortex cylinder trailing from the duct. Nevertheless, this simple model succeeds in predicting at least qualitatively the force and moment, the pressure distribution, and the separation of the boundary layer over the entire operating range of propeller thrust and free-stream angle of attack.

The following specific conclusions are drawn from the experimental data and theoretical calculations reported herein.

(1) The duct thrust force and pitching moment, as predicted for a thin cylinder surrounding an actuator disk, correspond reasonably well with the measured data. In hovering flight the 4-foot model duct carries about 50 percent of the total thrust and the 7-foot model duct about 60 percent. For the larger model, the duct thrust is predicted more accurately with the assumption that the pressure rise across the actuator disk acts on the inner duct surface aft of the propeller. This is not the case for the smaller duct, apparently because the propeller loading is low near the blade tips.

(2) The duct normal force at angle of attack is well predicted for the 7-foot model and considerably overpredicted for the 4-foot model. This difference is also believed to be caused by the concentration of propeller loading nearer the hub for the smaller model, since theoretical estimates indicate that the duct normal force decreases with reduced loading of the propeller blade tips.

(3) The duct pressure distributions predicted for axial flow correspond reasonably well with the measured data. However, when the thrust level and blade pitch are both high, the pressure on the inner surface of the 7-foot duct is lower than predicted, and the predicted discontinuity in pressure across the propeller is not evident in the data. These

differences are believed to be caused by low loading of the central part of the propeller.

(4) The predicted duct pressure distributions at angle of attack are in qualitative agreement with the data, but they are not always quantitatively accurate, particularly in the critical region for flow separation, inside the windward duct lip.

(5) For both ducts in axial flow, separation of the boundary layer on the inner surface is predicted to occur before the propeller except when the advance ratio is high and the thrust coefficient is low. Separation is predicted slightly farther forward on the 7-foot model duct than on the 4-foot model duct for the same thrust coefficient in axial flow; however, the duct-to-propeller thrust ratio is higher for the larger duct. The prediction of flow separation from the inner duct lip of the 4-foot model duct at angle of attack corresponds well with the stall boundary deduced experimentally from tufts, sound level, and pitching moment.

The general conclusion of this study is that the difference between the measured performance of the two ducted propellers and the theoretical predictions is caused mainly by differences in blade loading distribution and the prevalence of flow separation from the inner duct surface. More data and theory are needed to define and predict the distribution of blade loading, the duct boundary layer, and the interaction between the propeller blade tips and a region of flow separation.

It is recommended that additional experimental work be conducted to determine the distribution of vorticity in and around a ducted propeller in axial flow and at angles of attack up through the stall boundary. Measurements should be made of total and static pressure distribution, just before and aft of the propeller, at the duct exit, and in the wake. Detailed boundary-layer measurements should be made to determine where boundary-layer separation occurs on the outer and inner duct surfaces and the centerbody. The size of the separated regions should be defined, particularly a laminar separation bubble near the duct lip (if it exists) and the region near the blade tips. These data could be used with the methods described herein to determine their validity and the extent to which they should be modified and/or extended.

Vidya Division, Itek Corporation
Palo Alto, California
May 17, 1966

APPENDIX A

DISCUSSION OF ASSUMPTIONS

Three assumptions were made regarding duct thrust which are examined here. These were to neglect the effects of (1) duct camber, (2) radial variation of propeller disk loading, and (3) disk pressure jump acting on the inner duct surface. The duct friction drag is also neglected based on the results in Appendix B.

Duct Camber

The camber on the 4- and 7-foot models is relatively small. To verify that the effect of this camber on the duct thrust is small, the value of the duct thrust coefficient was computed from Equation (B-3) of Reference 13 as

$$C_{T_{D(P)}} = -\pi \frac{c}{D} \frac{\gamma^2}{V^2} \Big[C_o(4B_o + 2B_1) + 2C_1 B_o + C_2 B_1 + C_3 B_2 + C_4 B_3 + C_5 B_4 + \ldots - C_1 B_2 - C_2 B_3 - C_3 B_4 - C_4 B_5 - \ldots \Big] \qquad \text{(A-1)}$$

This equation is derived by summing the thrust force on the elementary ring vortices of the duct-bound vorticity due to the radial velocity acting on them. The duct vorticity includes the effect of thickness ϵ_t, and the radial velocity is that induced by the trailing vorticity. It can be shown that Equation (A-1) is mathematically identical to the duct thrust corresponding to the pressure distribution integrated over the duct for constant total head. Values computed from Equation (A-1) using the appropriate duct characteristics are listed in Table A-1 for comparison with values from Equation (5) and Table III. The values are in close agreement except when the duct thrust is extremely small compared with both the propeller thrust and the duct friction. Hence, the effect of camber on the thrust of both ducts seems negligible and use of the simple Equation (5) is considered justified.

Radial Variation of Propeller Disk Loading

To predict the duct force, moment, and pressure distribution, it was assumed that the vorticity bound to the propeller blades did not vary with radius and that it was all shed from the blade tips onto the inner duct surface and then trailed from the duct (Sketch B). Here we shall examine the effect of alternate placement of this trailing vorticity.

First, two computed cases were repeated with the vorticity trailing axially downstream from the propeller blade tips as shown in Figures A-1 and A-2. Comparison of the resulting predicted duct pressure distributions in these figures shows that they do not agree as well with the data as the former predicted distributions (from Figs. 10(a) and 10(c)). The corresponding duct thrust coefficient predicted from the measured total thrust coefficient is listed in Table A-II for comparison with measured and predicted values given previously in Table III. The results indicate that when the vorticity is not allowed to follow the duct, both the duct thrust and the pressure distribution are underpredicted.

To investigate a radial variation of disk loading, predictions were made by approximating the measured total pressure distribution with the stepwise distribution shown in Figure 11(b) for the 4-foot model. The predicted duct pressure distribution is shown by dashed curves in Figure A-3. Predicted thrust coefficients are listed in Table A-III for comparison with measured values and those previously predicted in Table III. The predicted results indicate that the division of thrust between the duct and propeller and the duct pressure distribution are nearly the same as before for the single vortex cylinder trailing from the duct. Moreover, the discontinuity in duct surface pressure at the propeller is smoothed out as the propeller blade tips are unloaded. The difficulty with this approach, however, is that propeller wake surveys are generally not available to define the radial loading variation and, at present, there is no method of predicting the variation from propeller, duct, and onset flow characteristics.

Duct Thrust from Pressure Jump

For a uniform actuator disk loading there is a discontinuity in the duct pressure across the disk. The increased pressure acting on the inner duct surface aft of the propeller causes a duct thrust which has been

neglected. To investigate this effect, calculations were repeated assuming a uniformly loaded actuator disk as before, but with the pressure jump acting on the inner duct surface. The computational procedure is the same as before except that in calculating γ/V we let $A_p/A = 1$ in Equation (10). Recomputed pressure distributions for both ducts are shown by the dashed curves in Figures A-4, A-5, and A-6. Predicted force coefficients are listed in Table A-IV for comparison with measured values and those previously predicted in Table III.

With the disk pressure jump acting on the inner duct surface, the duct thrust from leading edge suction ($C_{T_{D_S}}$) is less than the duct thrust previously predicted, but the total duct thrust is greater than previously predicted. For the 4-foot model, the recomputed duct thrust is considerably greater than the measured thrust and the agreement is much worse than that of Table III. For the 7-foot duct, the recomputed duct thrust is generally in better agreement with the measured values than is the case in Table III. This trend is probably caused by higher blade tip loading for the larger propeller such that more of its pressure rise acted on the duct. The pressure distributions (Figs. A-4 through A-6) indicate that the reduced duct leading-edge suction causes poorer agreement with the measured data for both ducts.

Comparison of the last two columns in Table A-IV shows that the total duct thrust from the pressure distribution over the cambered duct is nearly equal to the sum of the leading-edge suction on the equivalent thin cylinder plus the disk pressure jump acting on the inner duct surface.

Based on the results in this appendix, it seems possible to predict the duct thrust and pressure distribution using a uniformly loaded actuator disk to represent a nonuniformly loaded propeller by use of the following approximations:

(1) Neglect the pressure rise across the propeller blade tips, so that the total pressure is constant around the duct profile. The total measured duct thrust is then given by the radial velocity induced by the disk acting on the duct-bound vorticity (Eq. (A-1)). Compute this duct thrust by approximating it with the leading-edge suction on a thin cylinder (Eq. (5)). The frictional drag force on the duct is neglected based on the results in Appendix B.

(2) The duct pressure distribution is computed for the uniformly loaded disk with the discontinuity in pressure across the actuator disk. This pressure distribution approximates that which would be computed for a nonuniformly loaded propeller with the discontinuity smoothed out locally as the propeller blade tips are unloaded.

TABLE A-I

COMPARISON OF PREDICTED DUCT THRUSTS FOR THIN CYLINDERS AND FOR THICK DUCTS

	J	Predicted $C_{T_{D(P)}}$ (Eq. (3))	Predicted $C_{T_{D(P)}}$ (Eq. (A-1))
Four-foot Model Duct	0.541	0.168	0.181
	.178	8.62	8.66
Seven-foot Model Duct	0.682	0.0022	0.0036
	.525	.095	.104
	.437	.230	.240
	.311	.99	1.02
	.214	3.19	3.11

TABLE A-II

DUCT THRUST FOR ALTERNATE PLACEMENT
OF PROPELLER VORTICITY, 4-FOOT MODEL

Table III			Repeated Cases	
J	Measured $D_{T_{D(P)}}$	$C_{T_{D(P)}}$ From Measured $C_{T_{DP}}$ (Eq. (5))	$C_{T_{D(P)}}$ From Measured $C_{T_{DP}}$	
			(Eq. (5))	(Eq. (A-1))
0.541	0.186	0.168	0.156	0.114
.178	7.98	8.62	6.66	6.50

TABLE A-III

THRUST COEFFICIENTS FOR NONUNIFORM
PROPELLER BLADE LOADING, 4-FOOT MODEL

Coefficient	Measured	Predicted Table III	Repeated Case
$C_{T_{DP}}$	19.4	19.4	19.7
$C_{T_{D(P)}}$	8.0	8.6	8.7
$C_{T_{P(D)}}$	10.8	10.8	11.0

TABLE A-IV

DUCT THRUST WITH DISK PRESSURE JUMP ACTING ON THE DUCT

(a) 4-foot model.

Table III				Repeated Cases		
J	Measured $C_{T_{DP}}$	Measured $C_{T_{D(P)}}$	Predicted $C_{T_{D(P)}} = C_{T_{D_s}}$ (Eq. (5))	$C_{T_{D_s}}$ (Eq. (5))	Predicted $C_{T_{D(P)}} = C_{T_{D_s}} + \frac{\Delta p(A - A_p)}{qA}$	Predicted $C_{T_{D(P)}}$ = Eq. (A-1) $+ \frac{\Delta p(A - A_p)}{qA}$
0.541	0.890	0.186	0.168	0.102	0.338	0.348
.471	1.53	.403	.367	.244	.630	
.419	2.25	.671	.625	.427	.972	
.342	4.15	1.39	1.38	1.00	1.94	
.220	12.7	5.03	5.32	4.10	6.68	
.178	19.4	7.98	8.62	6.74	10.52	
0	306.0	147.0	164.0	136.0	187.0	

TABLE A-IV.- CONCLUDED.

(b) 7-foot model.

Table III				Repeated Cases		
J	Measured $C_{T_{DP}}$	Measured $C_{T_{D(P)}}$	Predicted $C_{T_{D(P)}} = C_{T_{D_s}}$ (Eq. (5))	$C_{T_{D_s}}$ (Eq. (5))	Predicted $C_{T_{D(P)}} = C_{T_{D_s}} + \frac{\Delta p(A - A_p)}{qA}$	Predicted $C_{T_{D(P)}} =$ Eq. (A-1) $+ \frac{\Delta p(A - A_p)}{qA}$
0.438	1.19	0.335	0.225	0.160	0.375	0.392
.219	8.46	3.47	3.05	2.46	3.72	3.79
.432	3.26	1.34	.912	.715	1.25	
.216	18.1	10.26	7.38	6.31	8.83	
.077	173.0	104.4	85.2	74.0	94.6	

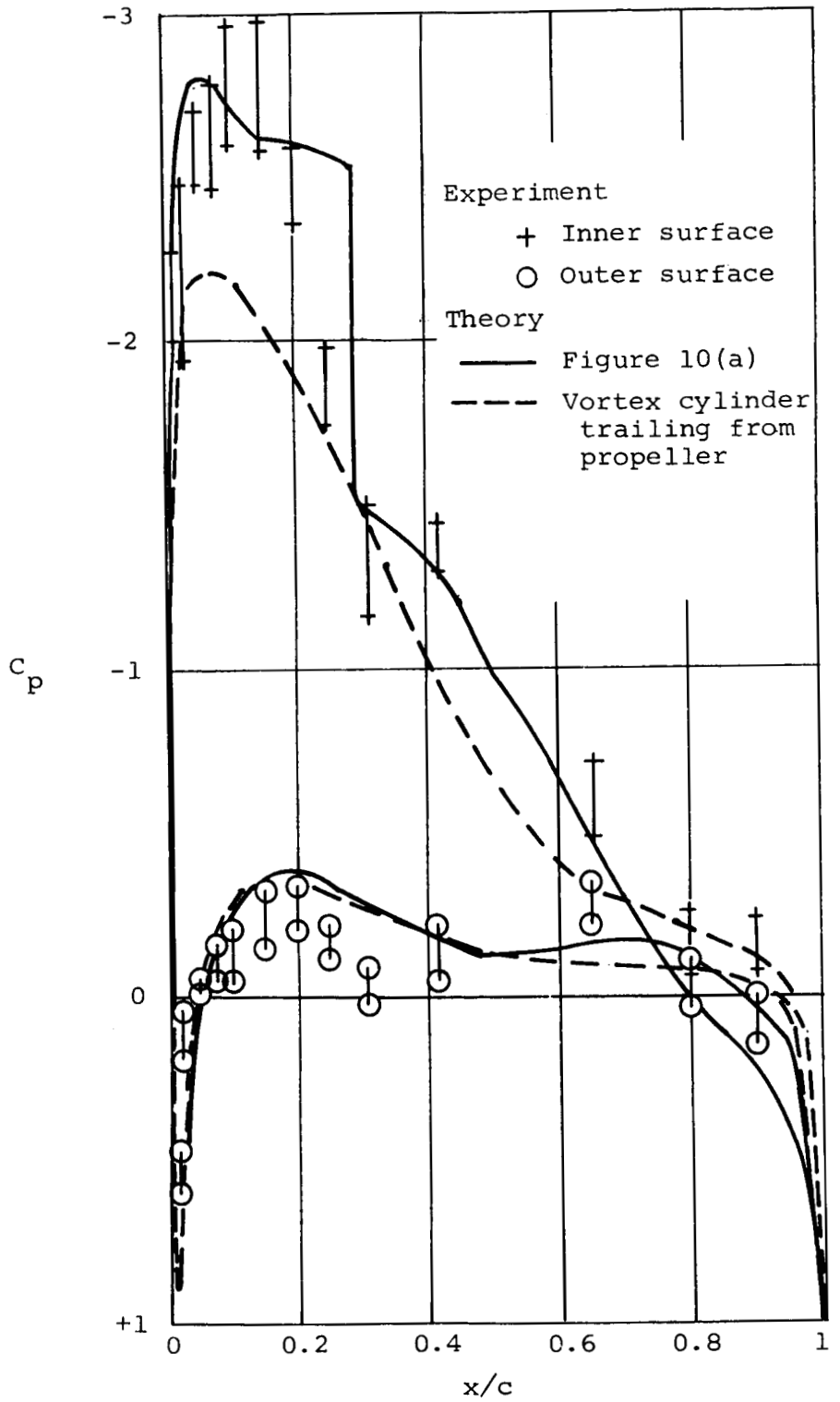

Figure A-1.- Pressure distribution for the 4-foot model duct with a vortex cylinder trailing from the propeller blade tips at $\alpha = 0$, $J = 0.541$.

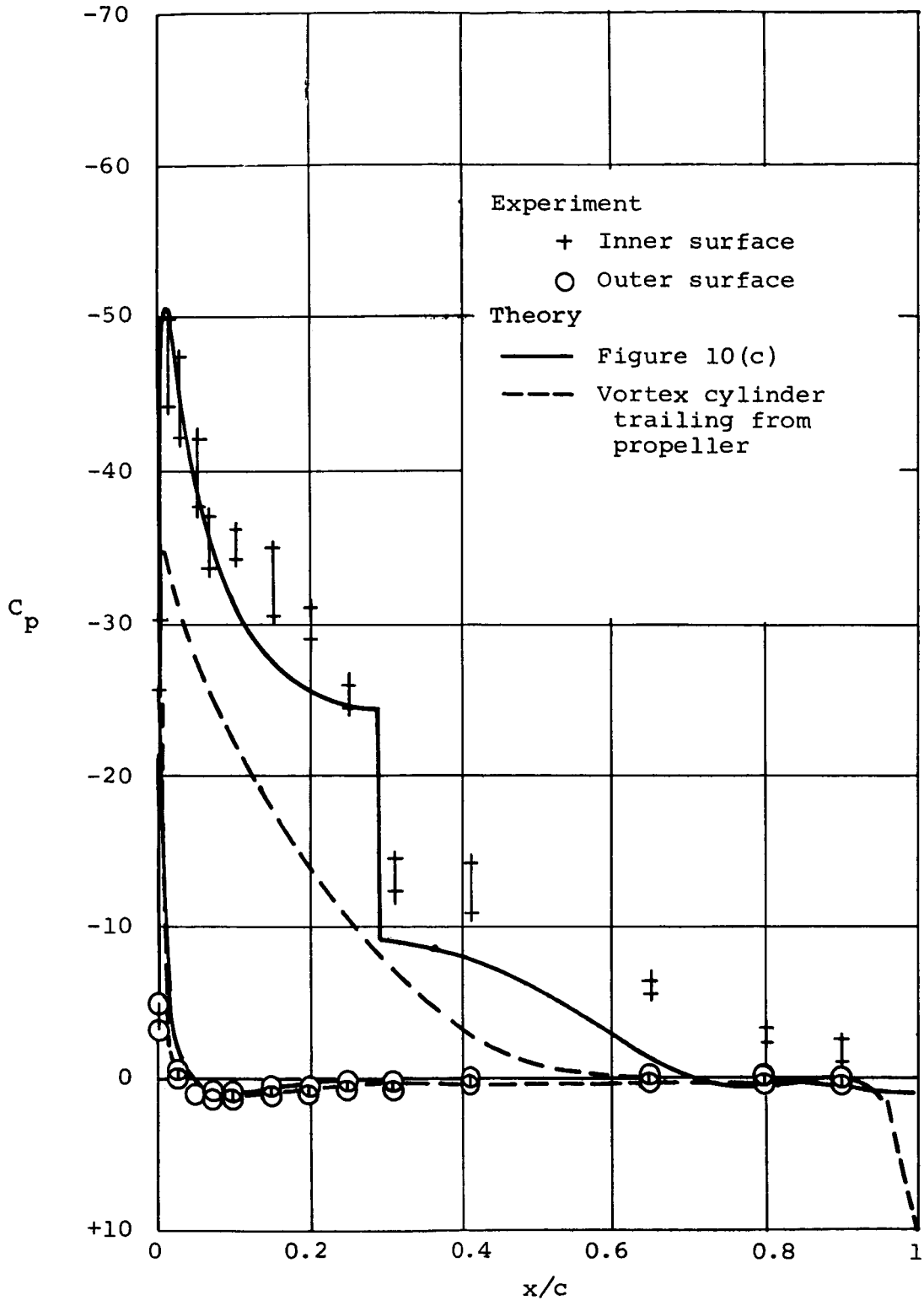

Figure A-2.- Pressure distribution for the 4-foot model duct with a vortex cylinder trailing from the propeller blade tips at $\alpha = 0$, $J = 0.178$.

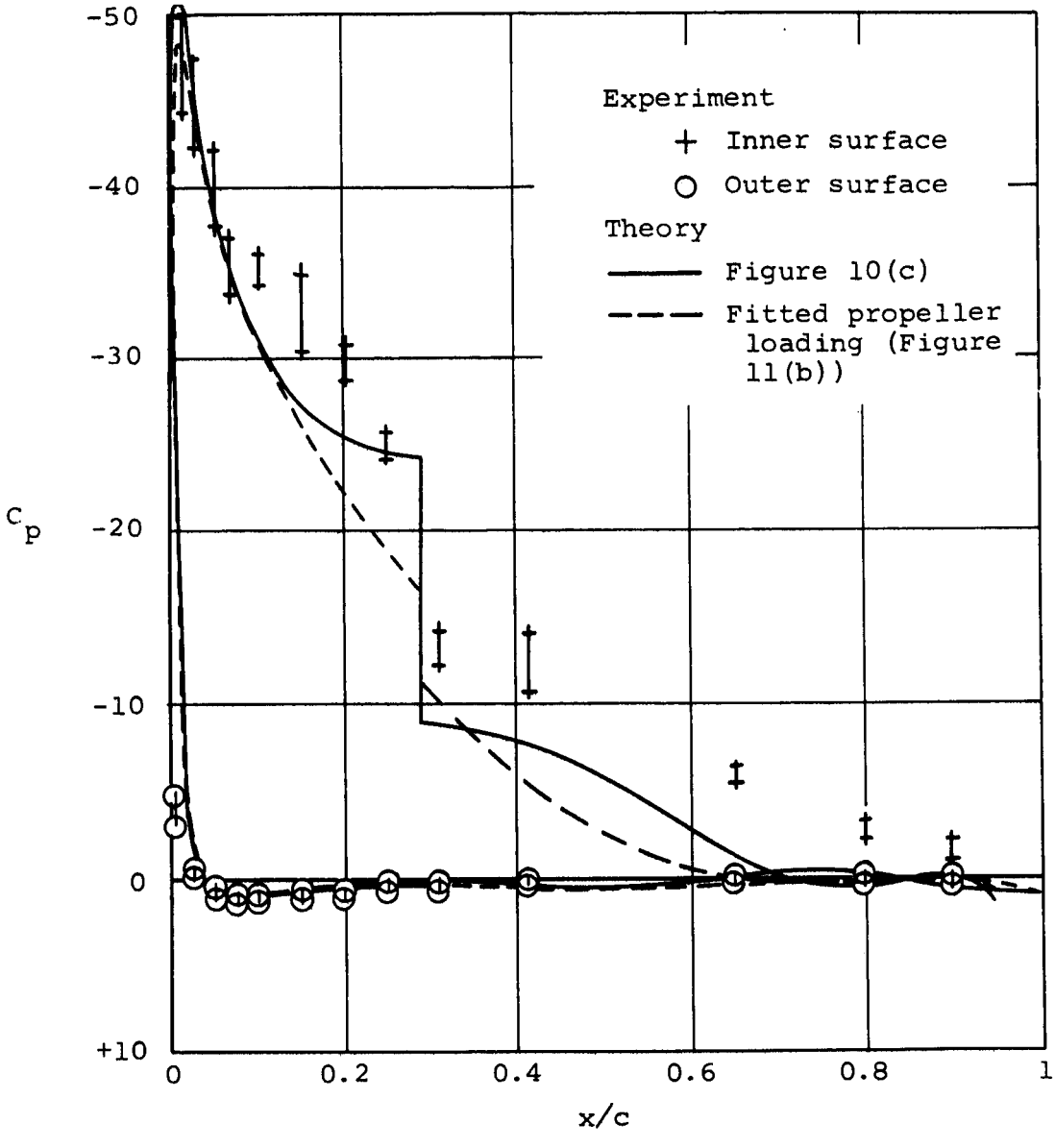

Figure A-3.- Pressure distribution for the 4-foot model duct with multiple vortex cylinders trailing from the propeller at $\alpha = 0$, $J = 0.178$.

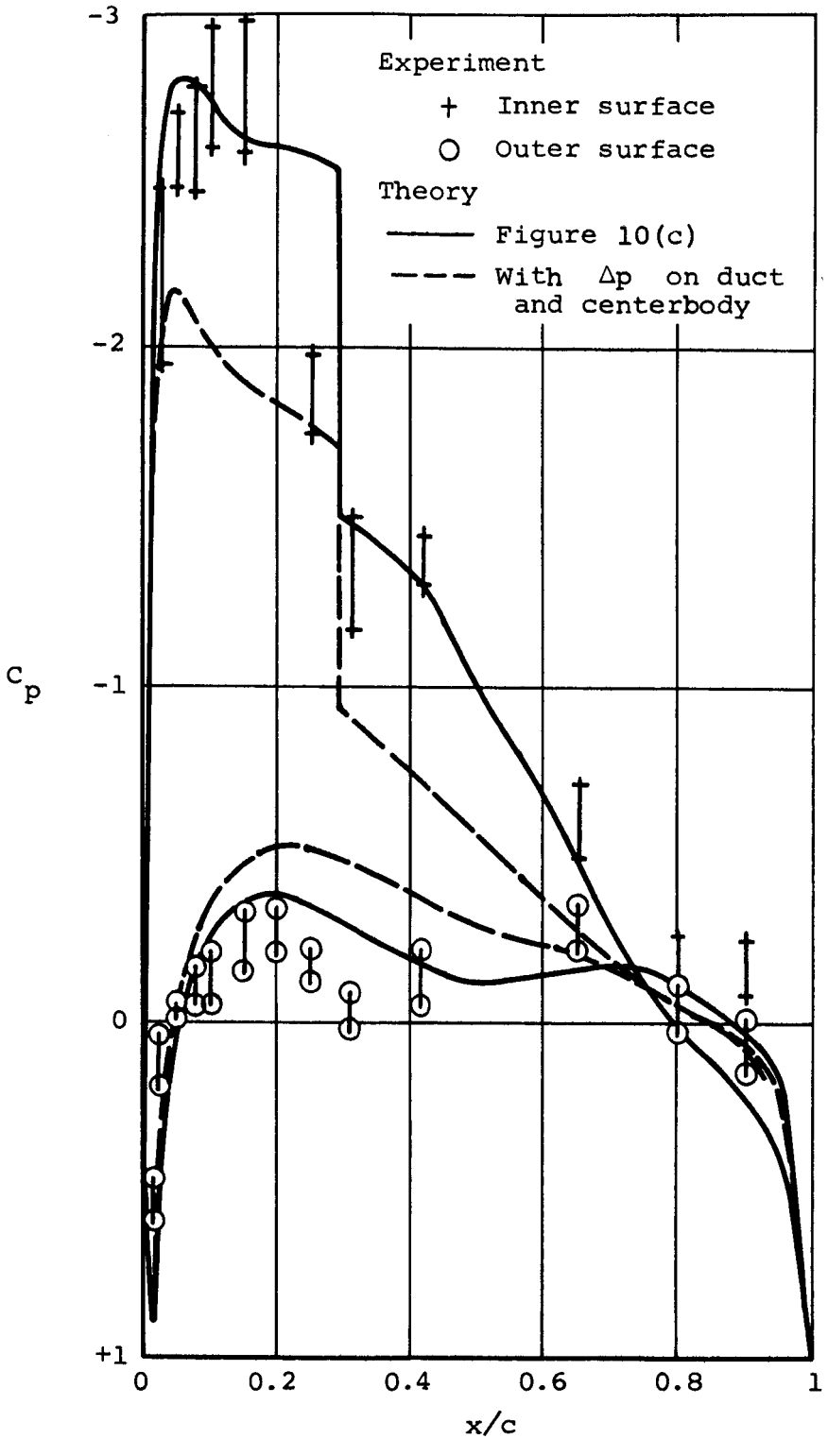

Figure A-4.- Pressure distribution for the 4-foot model duct with Δp acting on duct and centerbody at $\alpha = 0$, $J = 0.541$.

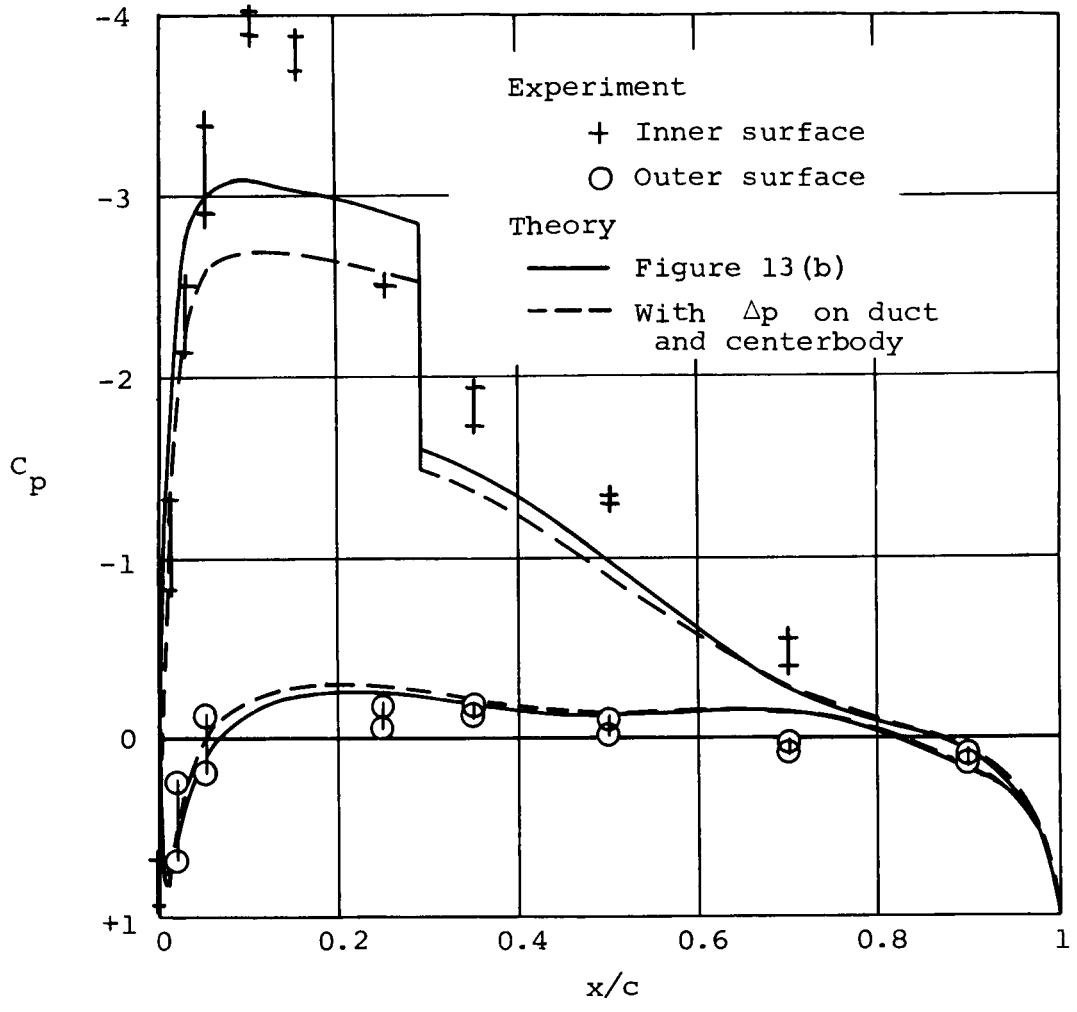

Figure A-5.- Pressure distribution for the 7-foot model duct with Δp acting on duct and centerbody at $\alpha = 0$, $J = 0.438$.

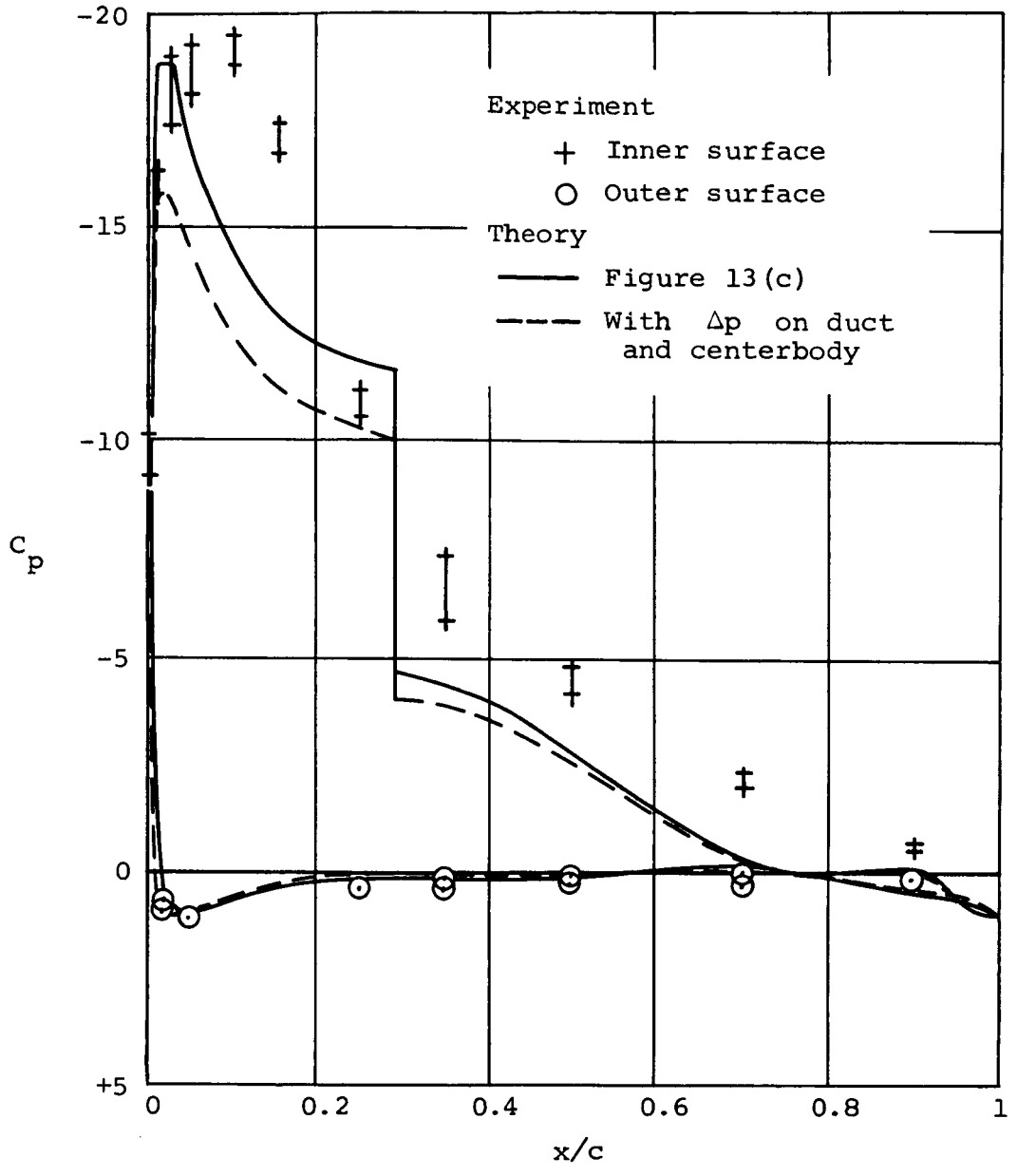

Figure A-6.- Pressure distribution for the 7-foot model duct with Δp acting on duct and centerbody at $\alpha = 0$, $J = 0.219$.

APPENDIX B

DUCT FRICTIONAL DRAG ESTIMATION

Here we estimate the total drag force on the duct due to its boundary layer for axially symmetric flow. For this purpose, we represent the duct as a thin cylinder with unseparated turbulent boundary layers on the inner and outer surfaces. We approximate the surface velocity distribution on each side by a constant gradient profile with free-stream V at the trailing edge as shown in the sketch below.

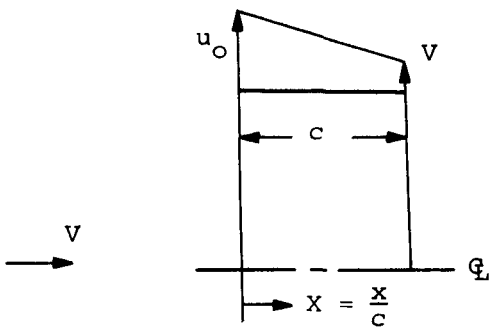

Sketch B-1.- Approximate velocity distribution on one side of duct.

Thus, the surface velocity on each side is given by

$$Y \equiv \frac{u}{V} = \frac{u_o}{V} - X\left(\frac{u_o}{V} - 1\right) \tag{B-1}$$

where

$$Y = Y_o = \frac{u_o}{V} \quad \text{at} \quad X = 0, \quad Y = 1 \quad \text{at} \quad X = 1$$

Using the Truckenbrodt solution for a turbulent boundary layer, the momentum thickness is given by (Eq. (22.20), Ref. 10)

$$\frac{\theta}{c} = \frac{c_f}{2}\left(\frac{u}{V}\right)^{-3}\left[\int_0^X \left(\frac{u}{V}\right)^{10/3} dX\right]^{6/7} \tag{B-2}$$

where c_f is the flat plate drag coefficient when $u = V$. Hence,

$$\left(\frac{2\theta}{c_f c}\right)^{7/6} = (Y)^{-18/7} \int_0^X Y^{10/3} dX$$

$$= (Y)^{-18/7} \int_{Y_o}^{Y} Y^{10/3} \frac{dY}{1 - \frac{u_o}{V}}$$

$$= \frac{3}{13(1 - Y_o)} (Y)^{-18/7} \left(Y^{13/3} - Y_o^{13/3}\right)$$

$$= \frac{3(Y_o)^{37/21}}{13(Y_o - 1)} \left[1 - \left(\frac{Y}{Y_o}\right)^{13/3}\right] \left(\frac{Y_o}{Y}\right)^{18/7} \qquad \text{(B-3)}$$

Now at the duct trailing edge (where $Y = 1$ and $\theta = \theta_c$) we have

$$\left(\frac{2\theta_c}{c_f c}\right)^{7/6} = \frac{3}{13(Y_o - 1)} Y_o^{37/21} \left(1 - Y_o^{-13/3}\right) Y_o^{18/7}$$

$$= \frac{3\left(Y_o^{13/3} - 1\right)}{13(Y_o - 1)} \qquad \text{(B-4)}$$

Using the result for a 1/7 power profile (p. 443, Ref. 10) we have for each side of the duct

$$c_f \equiv \frac{F_o}{q\pi Dc} = 0.072(Re_c)^{-1/5} \qquad \text{(B-5)}$$

where

$$Re_c = \frac{Vc}{\nu} \qquad \text{(B-6)}$$

and F_o is the flat plate drag when $v = V$.

Assuming free-stream pressure across the duct exit plane, we have the total drag on each side of the duct given by θ_c as

$$F = c_D q\pi Dc \qquad \text{(B-7)}$$

where

$$c_D = \frac{2\theta_c}{c} \tag{B-8}$$

Hence, using Equation (B-4), we can write

$$\frac{c_D}{c_f} = \frac{2\theta_c}{c_f c} = \left\{ \frac{3\left[\left(\frac{u_o}{V}\right)^{13/3} - 1\right]}{13\left(\frac{u_o}{V} - 1\right)} \right\}^{6/7} \tag{B-9}$$

$$\simeq 1 + \frac{10}{7}\left(\frac{u_o}{V} - 1\right) \quad \text{if} \quad \frac{u_o}{V} \simeq 1 \tag{B-10}$$

The following values from Equation (B-9) show that the duct drag increases rapidly with adverse velocity ratio:

u_o/V	c_D/c_f
1.25	1.42
1.67	2.45
2.0	3.55
4.0	18.9
6.0	54.0
7.0	82.2
8.0	119.0

Now to estimate the duct drag for the 4-foot model at $J = 0.541$, $\alpha = 0$, we have the free-stream velocity

$$V = nD_pJ = \frac{4600}{60}(4)(0.5415) = 166 \text{ fps}$$

The Reynolds number based on duct chord is

$$Re_c = \frac{10^4 Vc}{1.8} = \frac{10^4(166)\left(\frac{33}{12}\right)}{1.8} = 25.4\times10^5$$

$$Re_c^{1/5} = 19.1$$

Using Figure 10(a), we approximate the surface velocity as $u = V$ on the outer duct surface. On the inner surface, we use Equation (B-1) with $u_o = 2V$. From Equation (B-5) the drag coefficient on the outer surface is

$$c_f = 0.072(Re_c)^{-1/5} = \frac{0.072}{19.1} = 0.0038$$

From Equation (B-9) the drag coefficient on the inner surface is

$$c_D = 3.55\ c_f = 3.55(0.0038) = 0.0135$$

The total drag coefficient based on the duct exit plane area is

$$C_D = \frac{(c_f + c_D)(\pi cD)}{\frac{\pi}{4} D^2} = 4\ \frac{c}{D}\ (c_f + c_D) = 4(0.608)(0.0173) = 0.042$$

From Table III, the measured thrust coefficients for the duct and the entire configuration are

$$C_{T_{D(P)}} = 0.186$$

$$C_{T_{DP}} = 0.890$$

Hence, the estimated duct drag is small compared with the measured duct thrust.

Similarly, for $J = 0.178$ and $\alpha = 0$, we have

$$V = nD_pJ = \frac{2800}{60}\ (4)(0.1784) = 33.3 \text{ fps}$$

$$Re_c = \frac{10^4 Vc}{1.8} = \frac{10^4(33.3)\left(\frac{33}{12}\right)}{1.8} = 5.09\times10^5$$

$$Re_c^{1/5} = 13.8$$

From Figure 10(c), we shall take $u = V$ on the outer surface and $u_o = 6V$ on the inner surface. The drag coefficient on the outer surface is then

$$c_f = \frac{0.072}{13.8} = 0.00522$$

and on the inner surface

$$c_D = 54.0\ c_f = 0.282 = \frac{2\theta_c}{c}$$

The total drag coefficient based on the duct exit plane area is

$$C_D = 4(0.608)(c_f + c_D) = 0.70$$

The measured thrust coefficients are

$$C_{T_{D(P)}} = 7.98$$

$$C_{T_{DP}} = 19.4$$

In this case, the estimated boundary-layer momentum thickness inside the duct trailing edge ($\theta_c = 0.14\ c = 4.6$ in.) is so large that the boundary-layer equations are inaccurate. (Furthermore, the boundary layer is probably separated aft of the propeller, see Fig. 11(b).) However, these results indicate that the duct skin friction drag is small compared with the total thrust at all advance ratios.

At high advance ratio, the estimated duct drag coefficient based on exit area A is (for $u \simeq V$)

$$C_D \simeq 4\,\frac{c}{D}\,(2c_f) \simeq 0.02$$

Hence the duct drag can be large compared with the duct thrust when the advance ratio is high and the duct thrust coefficient is very small.

REFERENCES

1. Kriebel, A. R., Sacks, A. H., and Nielsen, J. N.: Theoretical Investigation of Dynamic Stability Derivatives of Ducted Propellers. Vidya Rpt. 63-95, Jan. 9, 1963, AD 403 146.

2. Kriebel, A. R.: Theoretical Investigation of Static Coefficients, Stability Derivatives, and Interference for Ducted Propellers. Vidya Rpt. No. 112, Mar. 31, 1964, AD 602 269 (published in part in Jour. of Aircraft, AIAA, vol. 1, no. 4, July-Aug. 1964).

3. Weissinger, J.: Remarks on Ring Airfoil Theory. Institute für Angewandts Mathematick der Technischen Hochschule Karlsruhe, Jan. 1958, European Office Air Research and Development Command, Contract AF 61(514)-1207, Air Force Office of Scientific Research, AFOSR TN 58-224, AD 154 127.

4. Ordway, D. E., Sluyter, M. M., and Sonnerup, B. O. U.: Three-Dimensional Theory of Ducted Propellers. TAR-TR-602, Therm Advanced Research Div. of Therm, Ithaca, New York, Aug. 1960.

5. Mort, K. W. and Yaggy, P. F.: Aerodynamic Characteristics of a 4-Foot-Diameter Ducted Fan Mounted on the Tip of a Semispan Wing. NASA TN D-1301, April 1962.

6. Hough, G. R.: The Aerodynamic Loading on Streamlined Ducted Bodies. TAR-TR-625, Therm Advanced Research Div. of Therm, Ithaca, New York, Dec. 1962.

7. Kuchemann, D. and Weber, J.: Aerodynamics of Propulsion. McGraw-Hill Book Co., Inc., New York, 1953.

8. Abbott, I. H. and von Doenhoff, A. E.: Theory of Wing Sections. Dover Publications, Inc., New York, 1959.

9. Truckenbrodt, E.: A Method of Quadrature for Calculation of the Laminar and Turbulent Boundary Layer in Case of Plane and Rotationally Symmetrical Flow. NACA TM 1379, May 1955.

10. Schlichting, H.: Boundary-Layer Theory. McGraw-Hill Book Co., Inc., New York, 1955.

11. von Doenhoff, Albert E. and Tetervin, Neal: Determination of General Relations for the Behavior of Turbulent Boundary Layers. NACA Rpt. No. 772, July 1943.

12. Bureau Technique Zborowski: Theoretical Investigation and Examination by Measuring Tests in What Degree the Economy of Flying Vehicles is Influenced by Pre-Cambered Skeletons of Airfoils Closed in Themselves. Contract DA-91-508-EUC-393, Aug. 10, 1959.

13. Kriebel, A. R. and Mendenhall, M. R.: Interference Between a Hull and a Stern-Mounted Ducted Propeller. Vidya Rpt. No. 204, Oct. 30, 1965.

TABLE I

EFFECT OF PROFILE THICKNESS ON
SURFACE VELOCITY DISTRIBUTION

x/c	$\frac{\gamma_D}{2V} = \frac{1}{2\pi} \cot \frac{\theta}{2}$ $t = 0$, $c_\ell = 1$ (Eq. (24))	$\frac{\gamma_D}{2V}$ NACA 0018, $c_\ell = 1$ (p. 325, Ref. 8)	$\frac{u_s}{V} = F(x)$ NACA 0018, $\alpha = 0$ (p. 325, Ref. 8)
0	∞	1.342	0
0.005	2.25	1.178	0.682
.025	.994	.861	1.103
.05	.695	.662	1.228
.1	.478	.479	1.276
.2	.319	.320	1.275
.4	.195	.184	1.205
.6	.130	.113	1.116
.8	.079	.063	1.025
1.0	0	0	0

TABLE II

SHAPE PARAMETERS FOR THE TWO DUCTED PROPELLERS

Parameter	4-foot model	7-foot model
D_p (in.)	48.0	84.7
$D_{H_{max}}$ (in.)	16.0	17.5
D (in.)	54.3	93.3
c (in.)	33.0	49.0
t_{max} (in.)	5.2	8.4
$(t/c)_{max}$	0.158	0.172
x_p/c	.293	.286
A_p/A	.70	.79
c/D	.608	.525
f_1	3.30	3.10
f_2	0.54	0.53
f_3	1.95	1.90
f_4	0.93	0.92
f_5	.29	.22
f_6	1.49	1.50
f_7	1.92	1.87
$f_5 f_6 + f_7$	2.35	2.20
R_o	-0.007	-0.040
R_1	- .007	- .068
R_2	- .040	- .058
R_3	.039	- .013
R_o*	- .008	- .041
R_1*	- .047	- .108
R_2*	- .053	- .071
R_3*	.040	- .012

TABLE III

MEASURED AND PREDICTED THRUST COEFFICIENTS FOR AXIAL FLOW

(a) 4-foot model.

J	$C_{T_{DP}}$ Measured	$C_{T_{P(D)}}$ Measured	$C_{T_{D(P)}}$ Measured	γ/V (Eq. (10))	$C_{T_{D(P)}}$ from measured $C_{T_{DP}}$ (Eq. (5))	γ/V (Eqs. (1),(3))	$C_{T_{D(P)}}$ from measured $C_{T_{P(D)}}$ (Eq. (5))
0.541	0.890	0.766	0.186	0.425	0.168	0.447	0.186
.471	1.53	1.15	.403	.630	.367	.623	.360
.419	2.25	1.62	.671	.820	.625	.820	.625
.342	4.15	2.74	1.39	1.22	1.38	1.22	1.38
.220	12.7	7.52	5.03	2.39	5.32	2.42	5.45
.178	19.4	10.8	7.98	3.05	8.62	3.06	8.70
0	306.0	142.0	147.0	13.3	164.0	13.3	164.0

TABLE III.- CONCLUDED.

(b) 7-foot model.

Elevon β°	J	$C_{T_{DP}}$ Measured	$C_{T_{D(P)}}$ Measured	γ/V (Eq. (10))	$C_{T_{D(P)}}$ from measured $C_{T_{DP}}$ (Eq. (5))
Aligned 19°	0.682	0.0826	-0.030	0.049	0.0022
	.525	.684	.099	.322	.095
	.437	1.21	.279	.500	.230
	.311	3.46	1.07	1.04	.99
	.214	8.80	3.70	1.86	3.19
Out 19°	.617	0.220	0.025	0.130	0.016
	.438	1.19	.335	.495	.225
	.219	8.46	3.47	1.82	3.05
Out 29°	.432	3.26	1.34	0.995	0.912
	.216	18.1	10.26	2.83	7.38
	.077	173.0	104.4	9.62	85.2

TABLE IV

COMPARISON OF MEASURED TOTAL NORMAL FORCE $C_{N_{DP}}$ AND MEASURED DUCT NORMAL FORCE $C_{N_{D(P)}}$ FOR THE 4-FOOT MODEL

J	α (deg)	$C_{N_{DP}}$ Measured	$C_{N_{D(P)}}$ Measured
0.542	20	1.28	0.66
.540	40	2.29	1.20
.542	60	2.65	1.53
0.178	20	1.55	1.16
.178	40	3.39	1.83
.176	60	5.42	2.06

TABLE V

COMPUTED FOURIER COEFFICIENTS FOR THE TWO DUCTS

Parameter	4-foot model duct	7-foot model duct
B_0	-0.2305	-0.2487
B_1	.2850	.2910
B_2	-.1630	-.1625
B_3	.1068	.1065
B_4	-.0795	-.0796
B_5	.0638	.0640
B_0^*	.1427	.1509
B_1^*	-.0821	-.0774
B_2^*	.0170	.0147
B_3^*	-.0042	-.0035
B_4^*	.0016	.0014
B_5^*	-.0008	-.0007

Parameter (for $R_n^* = 0$)	4-foot model duct	7-foot model duct
C_0	0.4922	0.5259
C_1	.7402	.7270
C_2	-.3142	-.3154
C_3	.2107	.2107
C_4	-.1589	-.1591
C_5	.1277	.1280
c_0	.955	.995
c_1	-.280	-.247
c_2	-.027	-.020
c_3, c_4, c_5	0	0

TABLE VI

$P_{k\ell}$ COEFFICIENTS FOR 4-FOOT MODEL DUCT (EQ. (19))

k \ ℓ	0	1	2	3	4	5	6
0	0.09287	0	0.04638	0	0.00006	0	0.00000
1	.18573	0.11179	0	-0.01906	0	0.00012	0
2	.03786	0	.02539	0	-.00650	0	.00004
3	.00022	-.00635	0	.00958	0	-.03314	0
4	-.00026	0	-.00325	0	.00497	0	-.00185
5	-.00002	.00003	0	-.00188	0	.00306	0
6	.00000	0	.00001	0	-.00122	0	.00208

TABLE VII

$P_{k\ell}$ COEFFICIENTS FOR 7-FOOT MODEL DUCT (EQ. (19))

k \ ℓ	0	1	2	3	4	5	6
0	0.07745	0	0.03874	0	-0.00002	0	0.00000
1	.15490	0.09140	0	-0.01403	0	0.00008	0
2	.02791	0	.01860	0	- .00466	0	.000025
3	-.00007	-.00468	0	.00690	0	- .00226	0
4	-.00016	0	-.00234	0	.00359	0	-.00134
5	-.000005	.00002	0	-.00136	0	.00222	0
6	.0000	0	.00001	0	-.00088	0	.00151

(a) 4-foot model.

Figure 1.- Ducted propellers mounted in the Ames 40- by 80-foot wind tunnel.

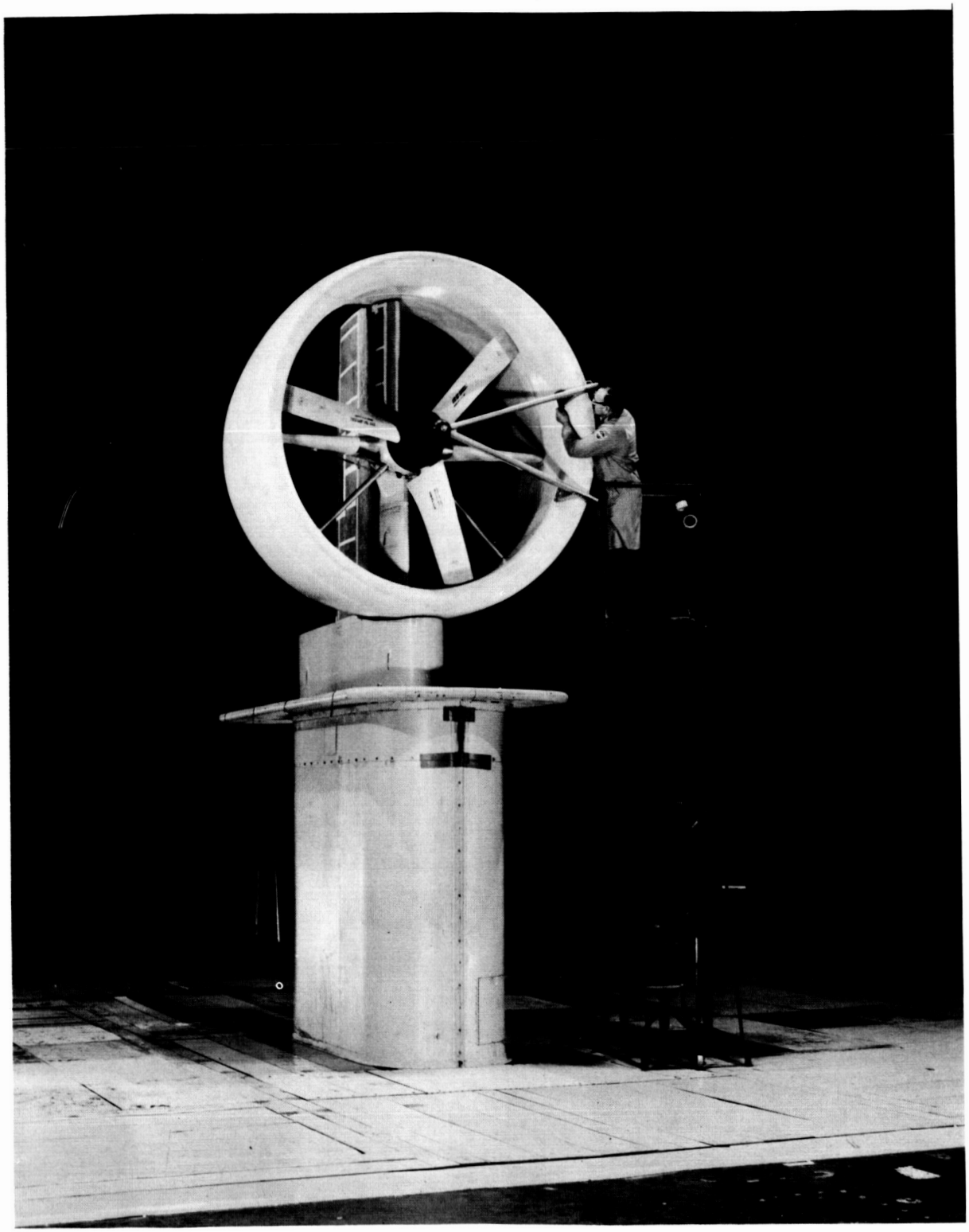

(b) 7-foot model.

Figure 1.- Concluded.

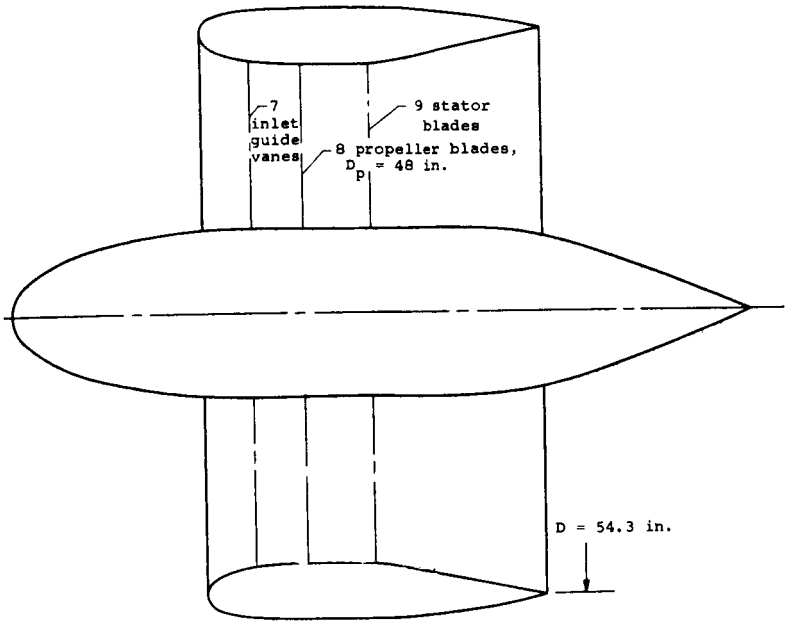

(a) 4-foot model.

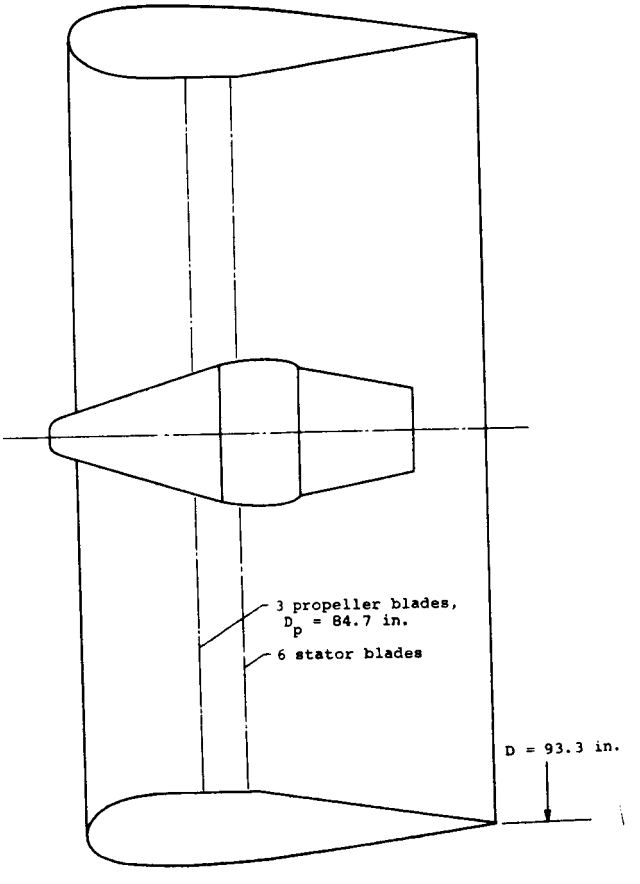

(b) 7-foot model.

Figure 2.- Ducted propeller cross sections.

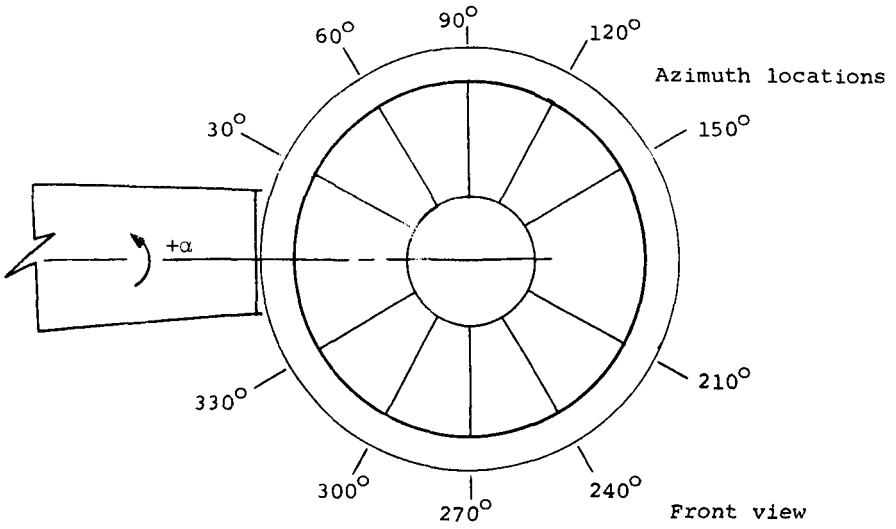

x/c	X, in.	Sta.	Y_U	Sta.	Y_L
0	0	1	2.90	28	2.90
1.25	0.412	2	3.37	27	1.37
2.5	.825	3	3.76	26	1.08
5.0	1.650	4	4.22	25	0.94
7.5	2.475	5	4.52	24	.51
10	3.30	6	4.75	23	.34
15	4.95	7	5.05	22	.14
20	6.60	8	5.18	21	.02
25	8.25	9	5.24	20	0
31	10.24	10	5.24	19	0
41.5	13.70	11	5.24	18	0
65	21.45	12	4.45	17	.22
80	26.40	13	3.48	16	.89
90	29.70	14	2.83	15	1.43

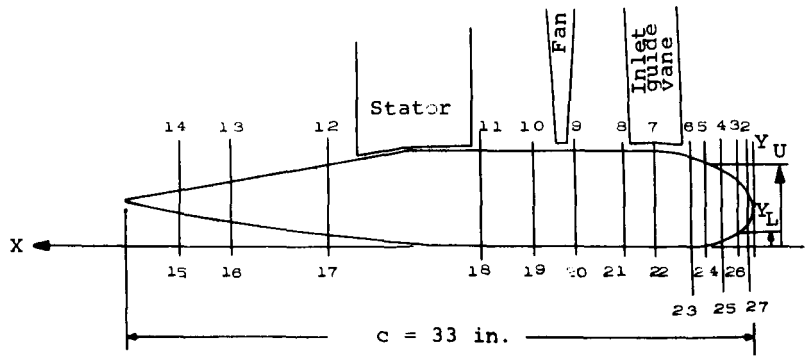

(a) Four-foot model, configuration and duct pressure orifices.

Figure 3.- Ducted propeller configurations and locations of measured pressures.

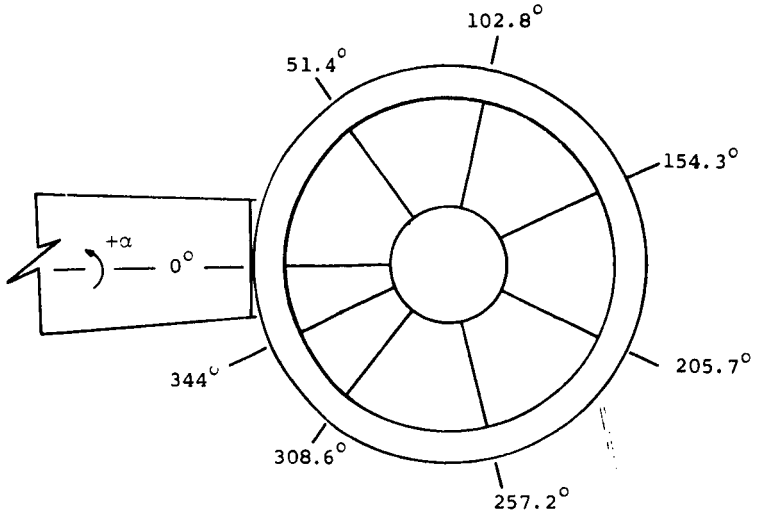

Azimuth Locations

Rake c	
Ctrbody Rad. = 7.25	
Duct Rad. R = 27.10	
	r/R
1	0.30
2	.40
3	.50
4	.60
5	.70
6	.80
7	.90
8	.95
9	.99

Rakes a and b	
Ctrbody Rad. = 8	
Duct Rad. r_s = 24	
	r/r_s
1	0.40
2	.50
3	.60
4	.70
5	.80
6	.90
7	.95
8	.99

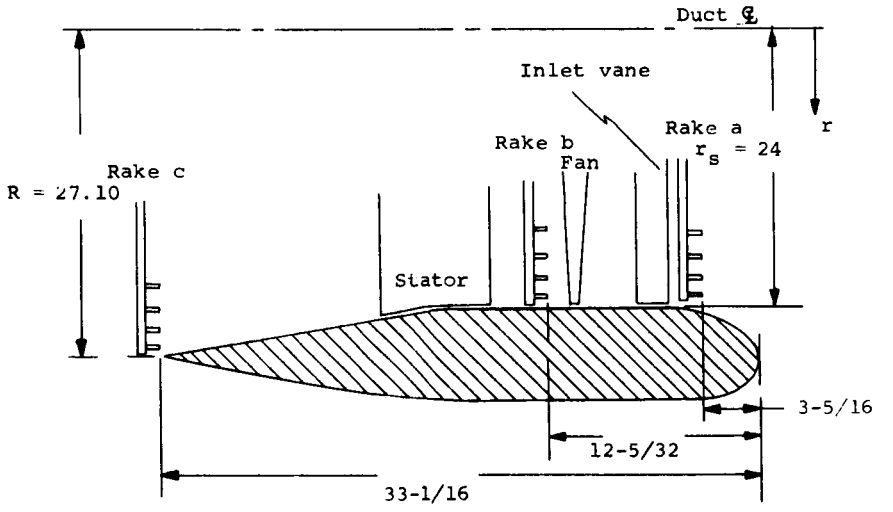

Longitudinal Section

(b) Four-foot model, details of rake installations.

Figure 3.- Continued.

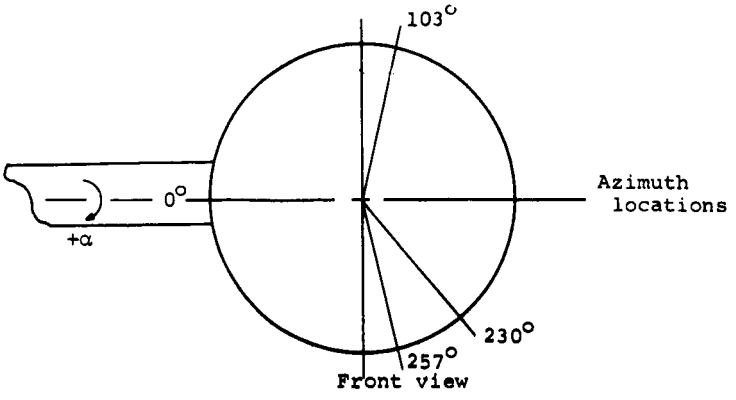

Duct Outer Ordinates	
X	Y
0	47.625
0.613	48.695
1.225	49.698
2.455	49.609
3.675	49.953
4.900	56.205
7.350	50.535
9.80	50.710
10.250	--
12.250	50.779
14.700	50.763
17.750	--
19.600	50.552
23.700	--
24.500	50.164
29.400	49.645
34.300	49.038
39.200	48.344
44.100	47.576
46.550	47.160
49.000	46.122

Duct Pressure Orifice Locations in Percent Chord	
Inner Surface	Outer Surface
0	2
1	5
2.5	15
10	25
15	35
25	50
35	70
50	90
70	
90	

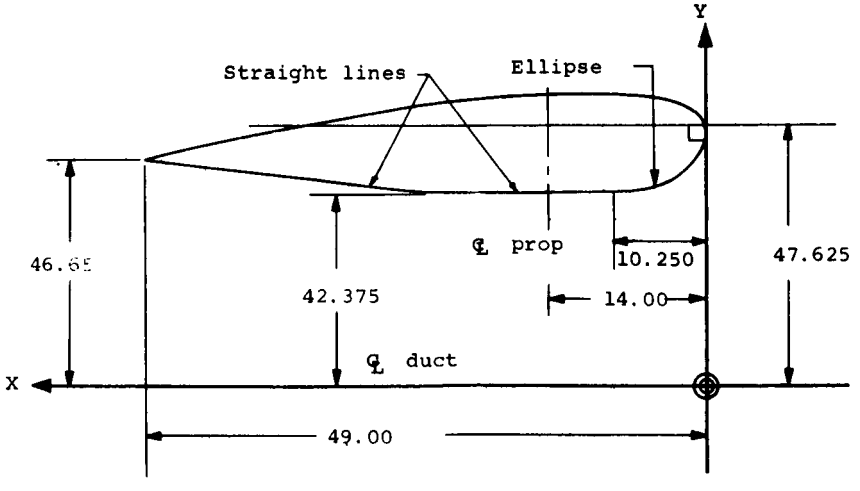

(c) Seven-foot model, configuration and duct pressure orifices.

Figure 3.- Concluded.

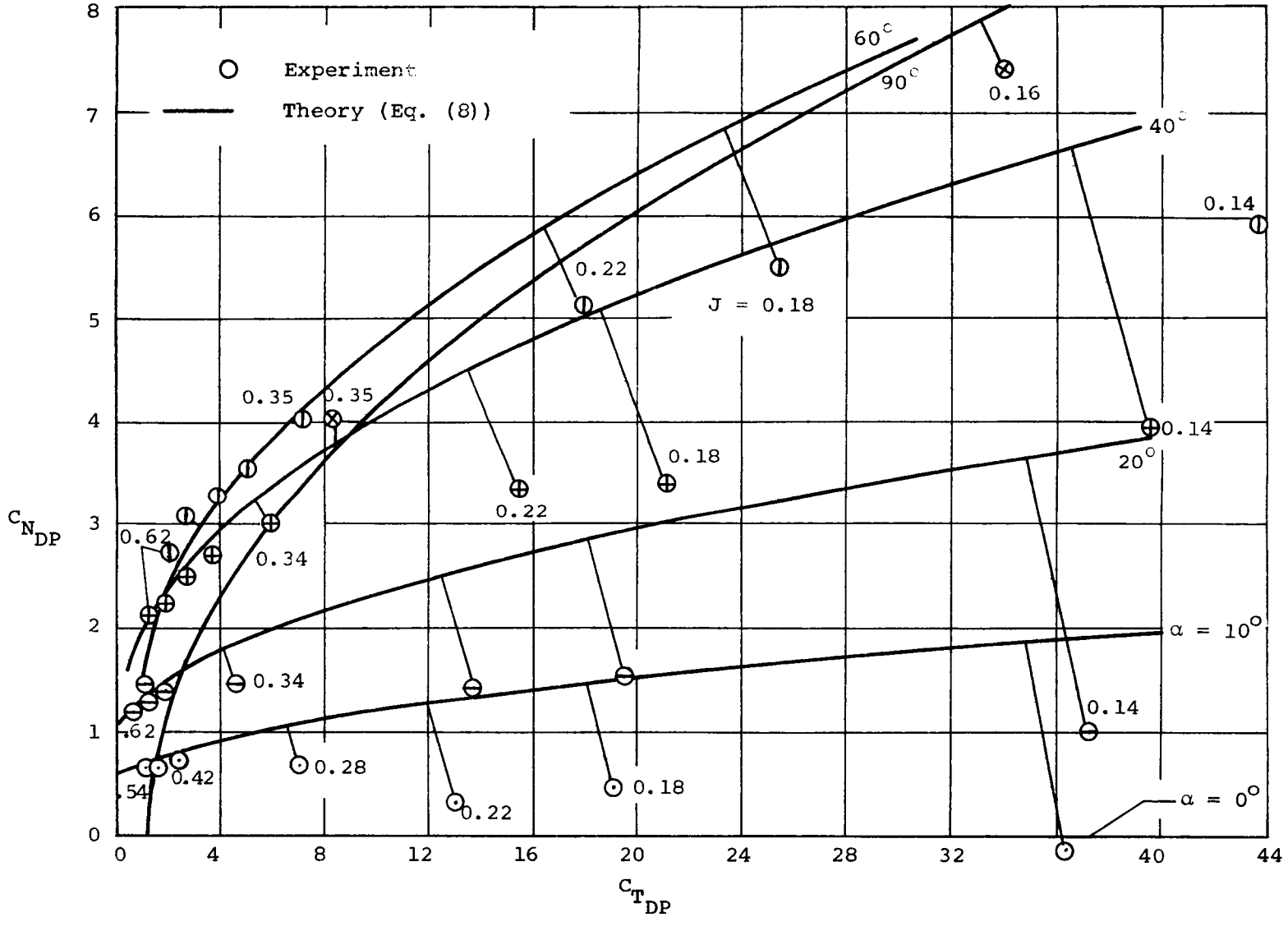

Figure 4.- Normal force versus thrust for the 4-foot model at $\alpha > 0$.

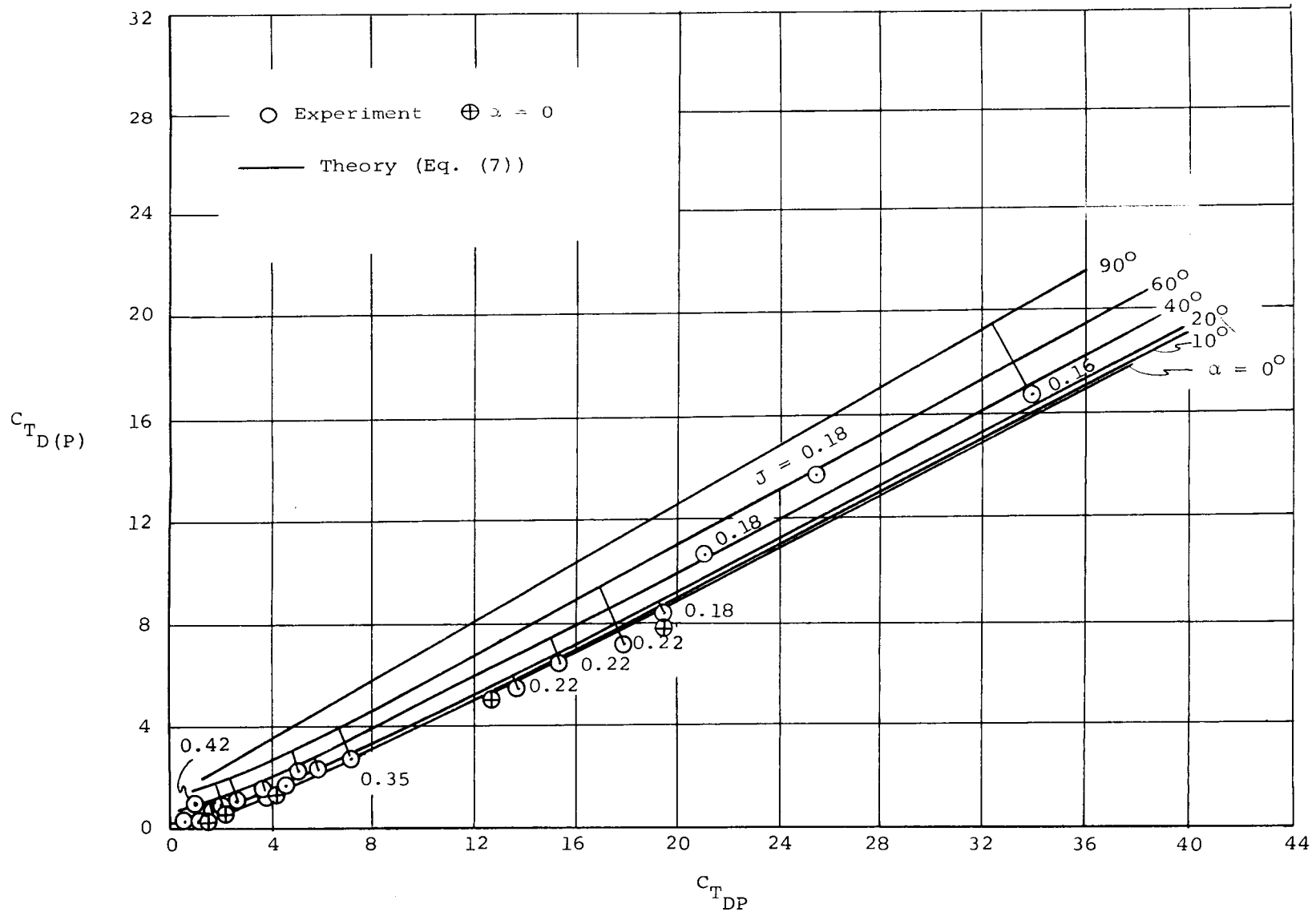

Figure 5.- Duct thrust versus total thrust for the 4-foot model at $\alpha > 0$.

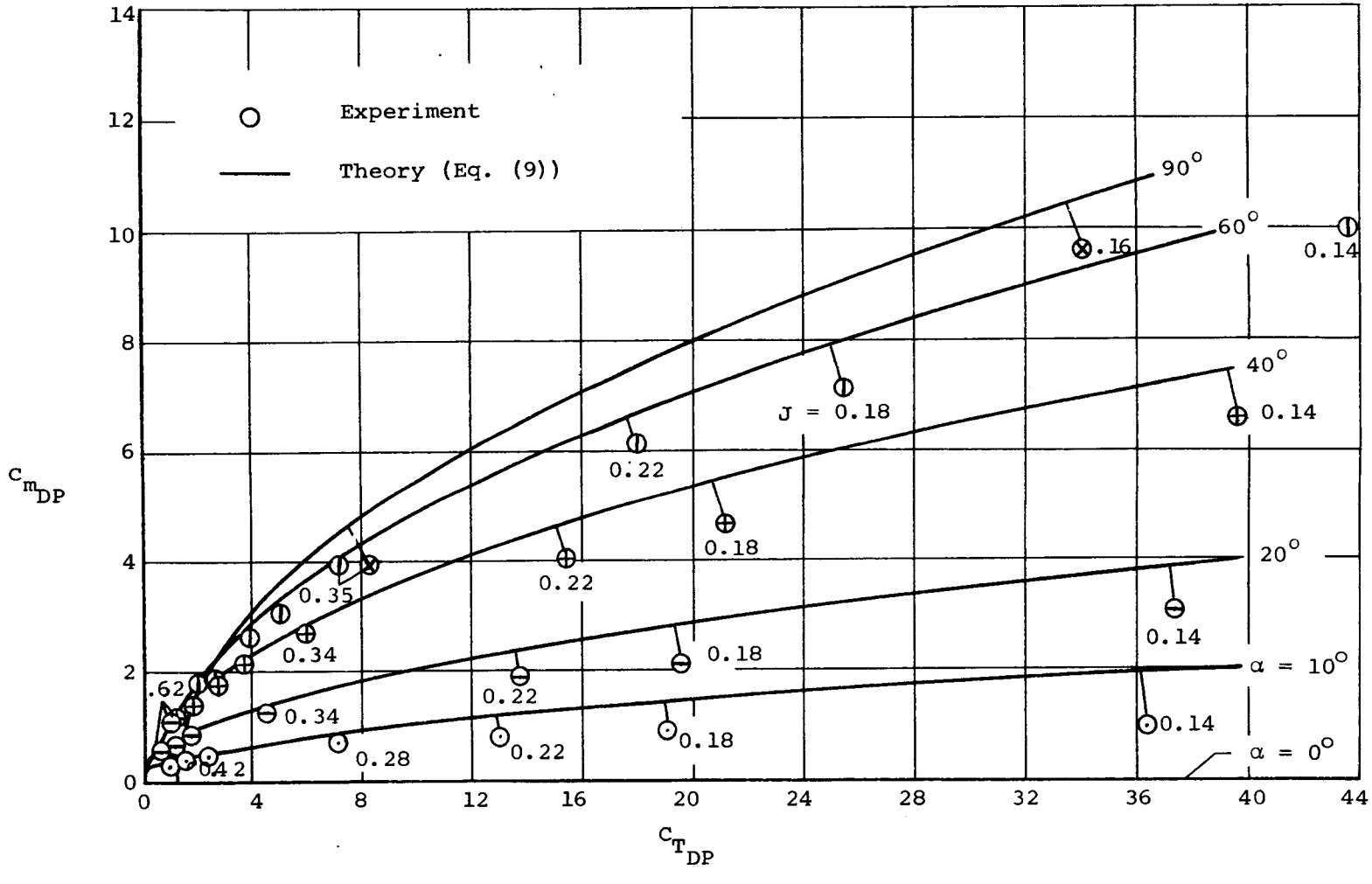

Figure 6.- Pitching moment versus thrust for the 4-foot model at $\alpha > 0$.

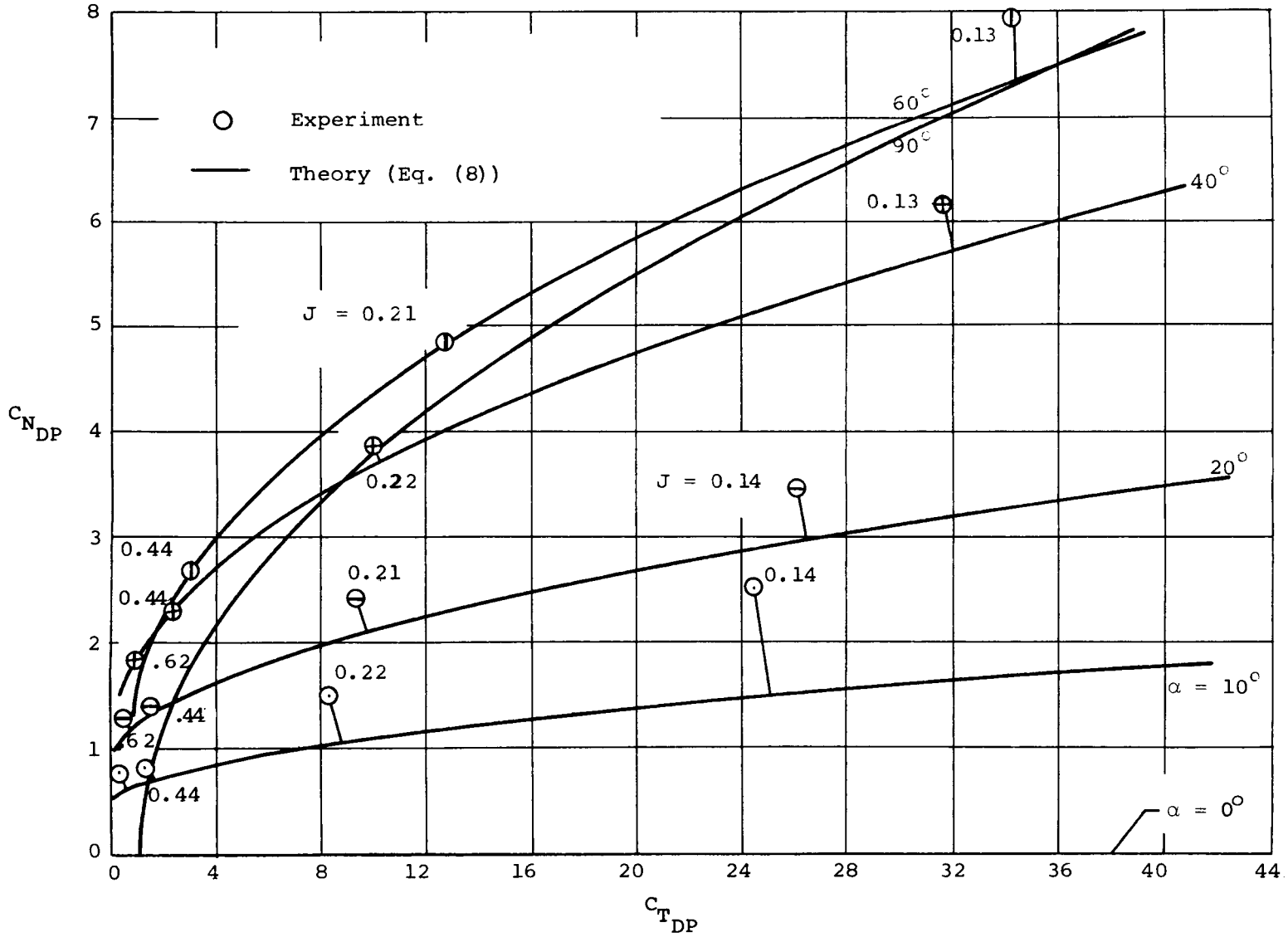

(a) Elevon off.

Figure 7.- Normal force versus thrust for the 7-foot model at $\alpha > 0$ with $\beta = 19^{\circ}$.

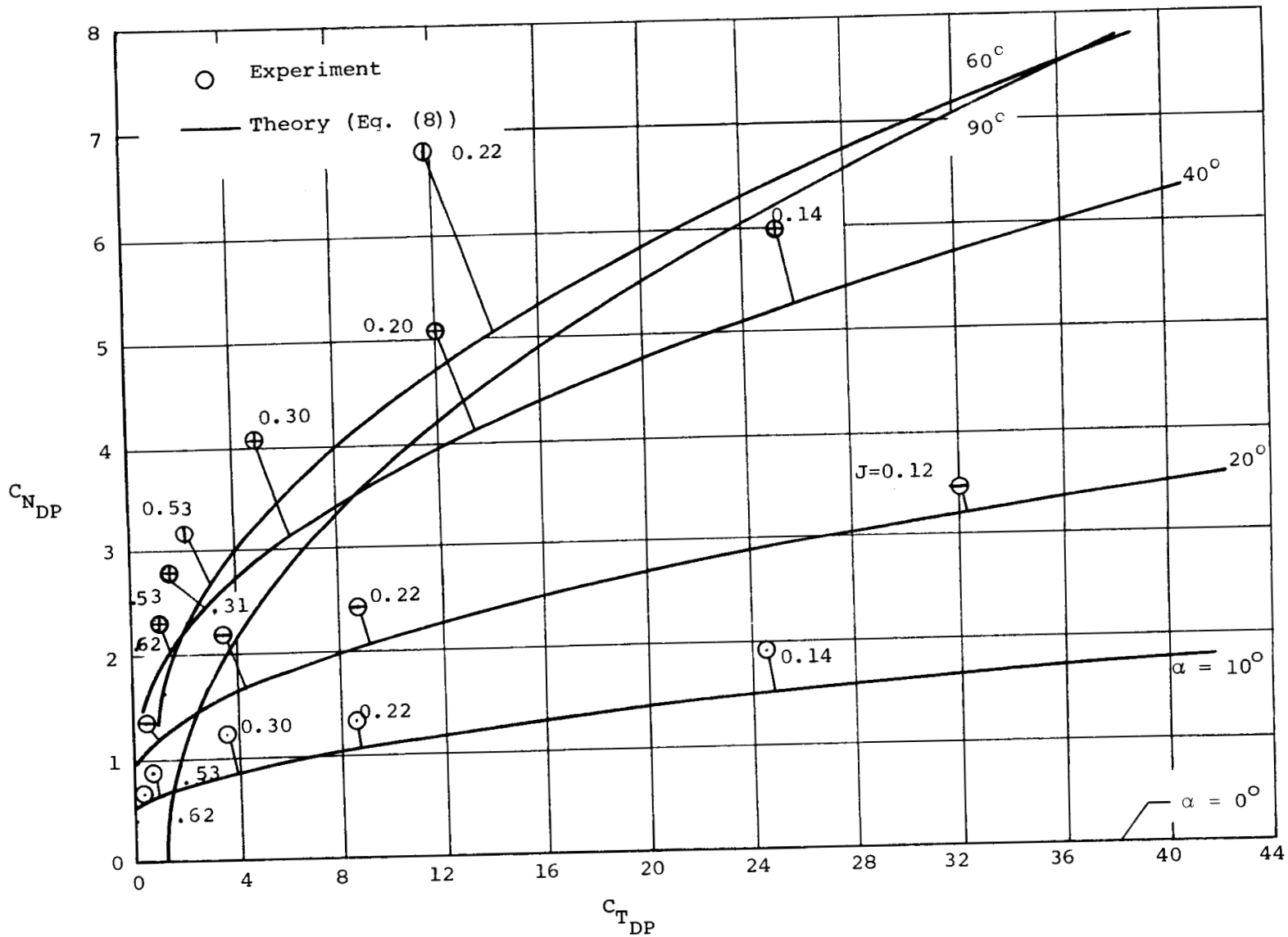

(b) $\delta_e = 0$

Figure 7.- Concluded.

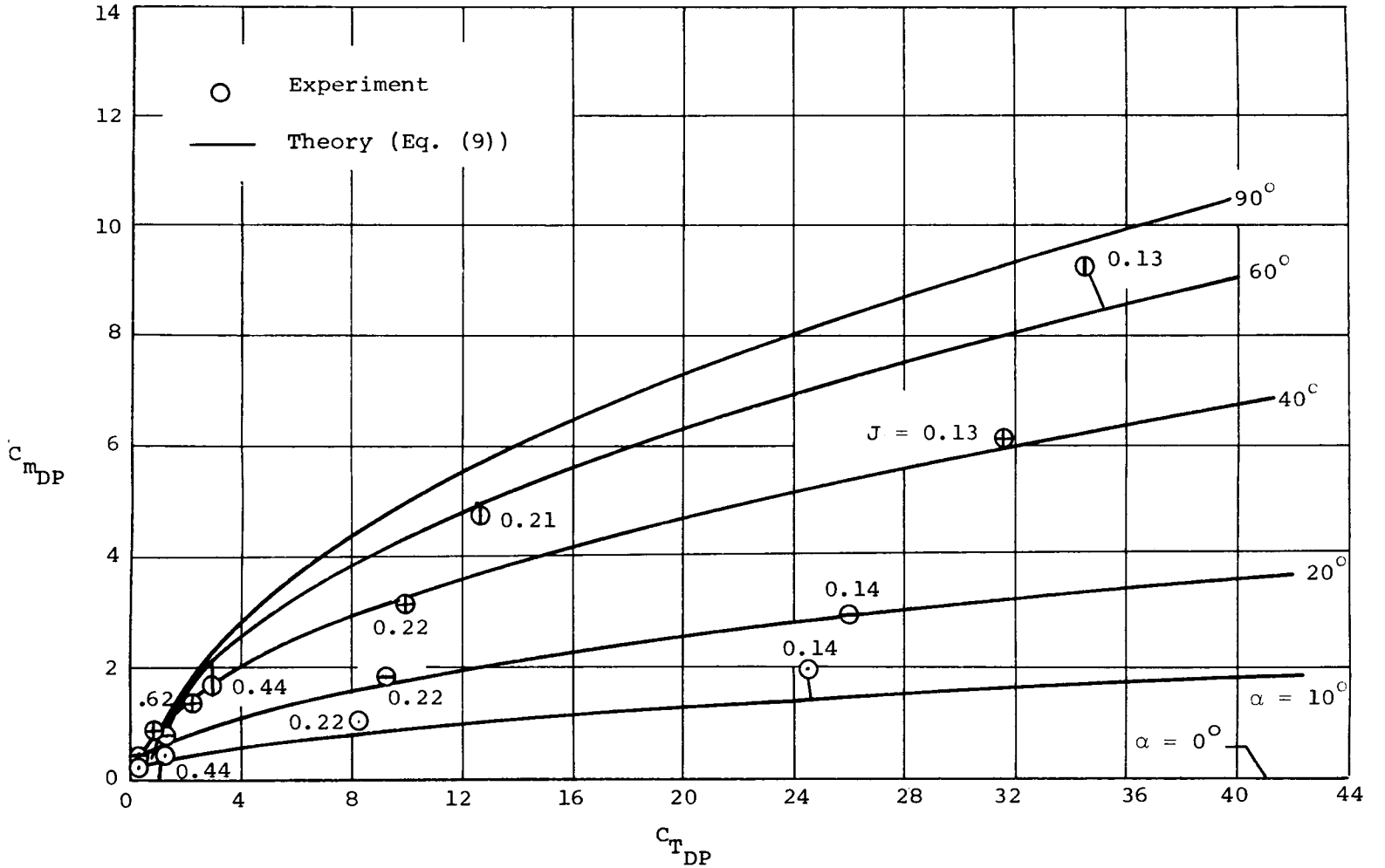

(a) Elevon off.

Figure 8.- Pitching moment versus thrust for the 7-foot model at $\alpha > 0$ with $\beta = 19^{\circ}$.

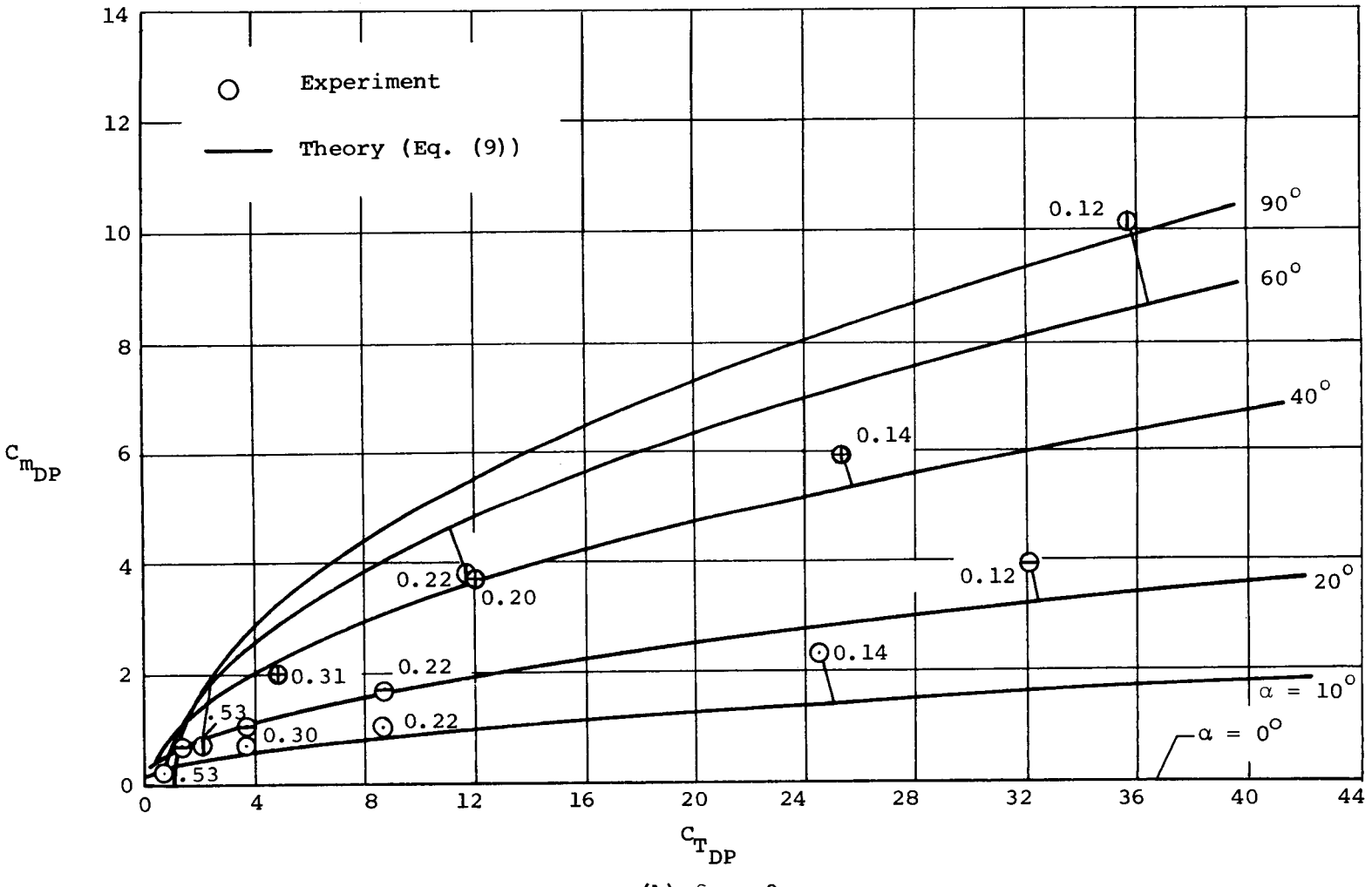

(b) $\delta_e = 0$

Figure 8.- Concluded.

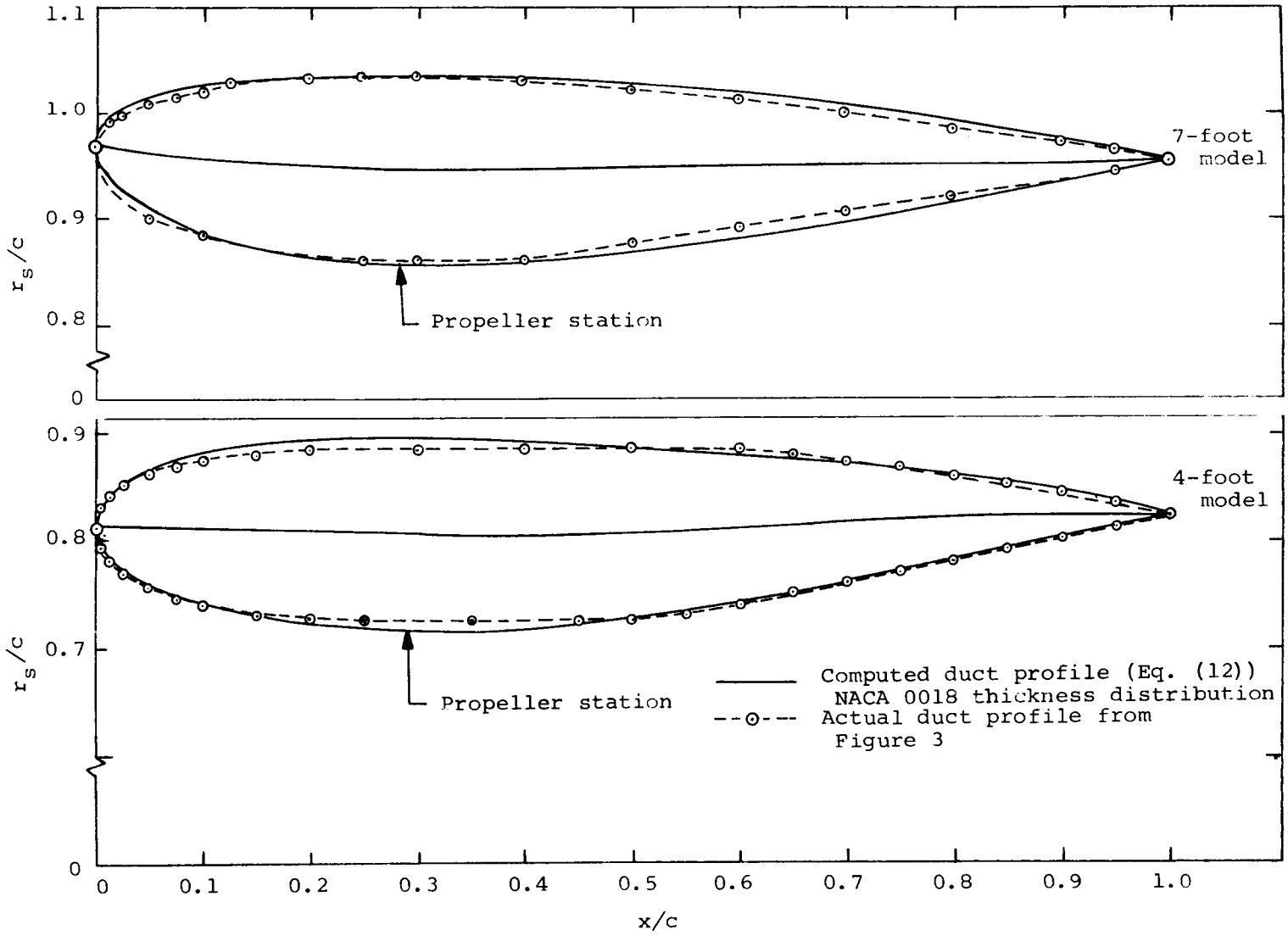

Figure 9.- Comparison of actual and computed duct profiles.

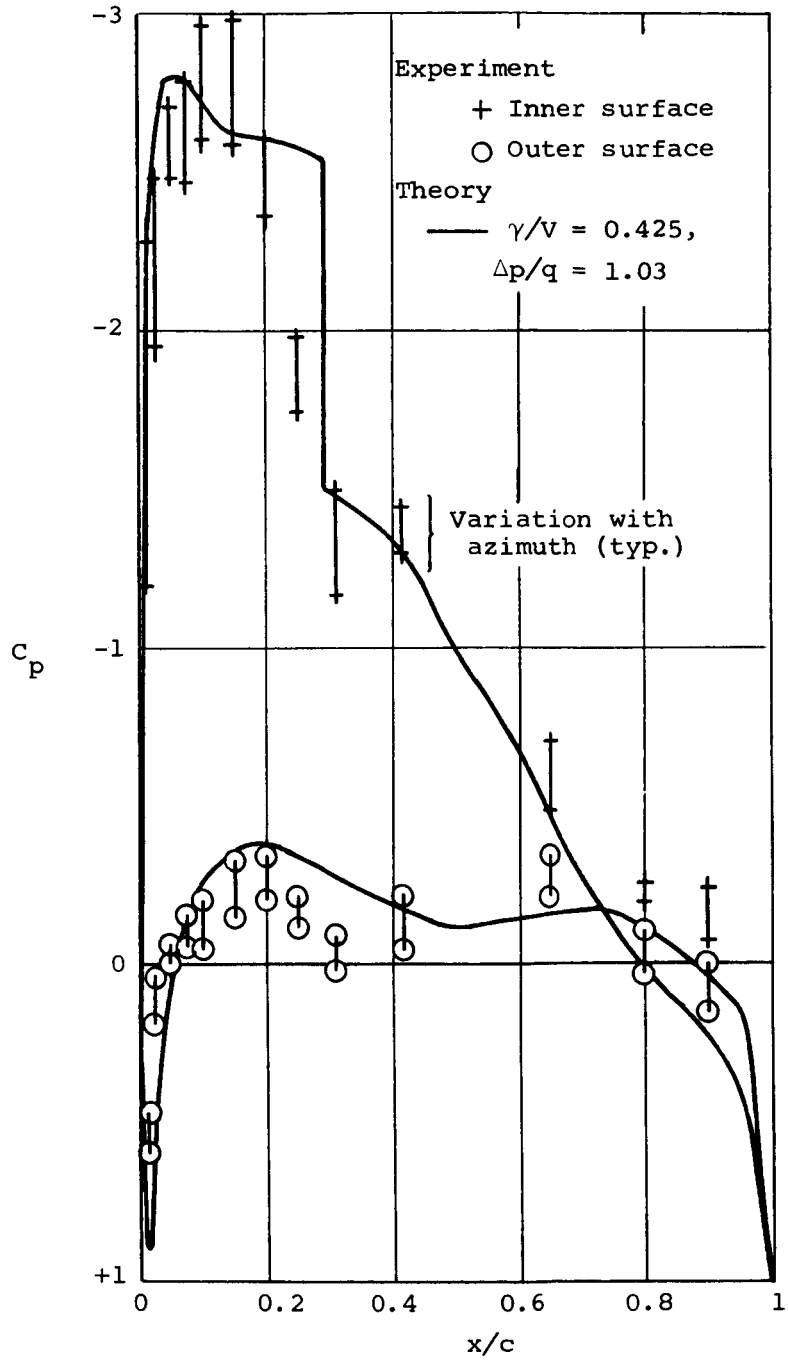

(a) J = 0.541, $C_{T_{DP}}$ = 0.890.

Figure 10.- Pressure distributions for the 4-foot model duct at α = 0.

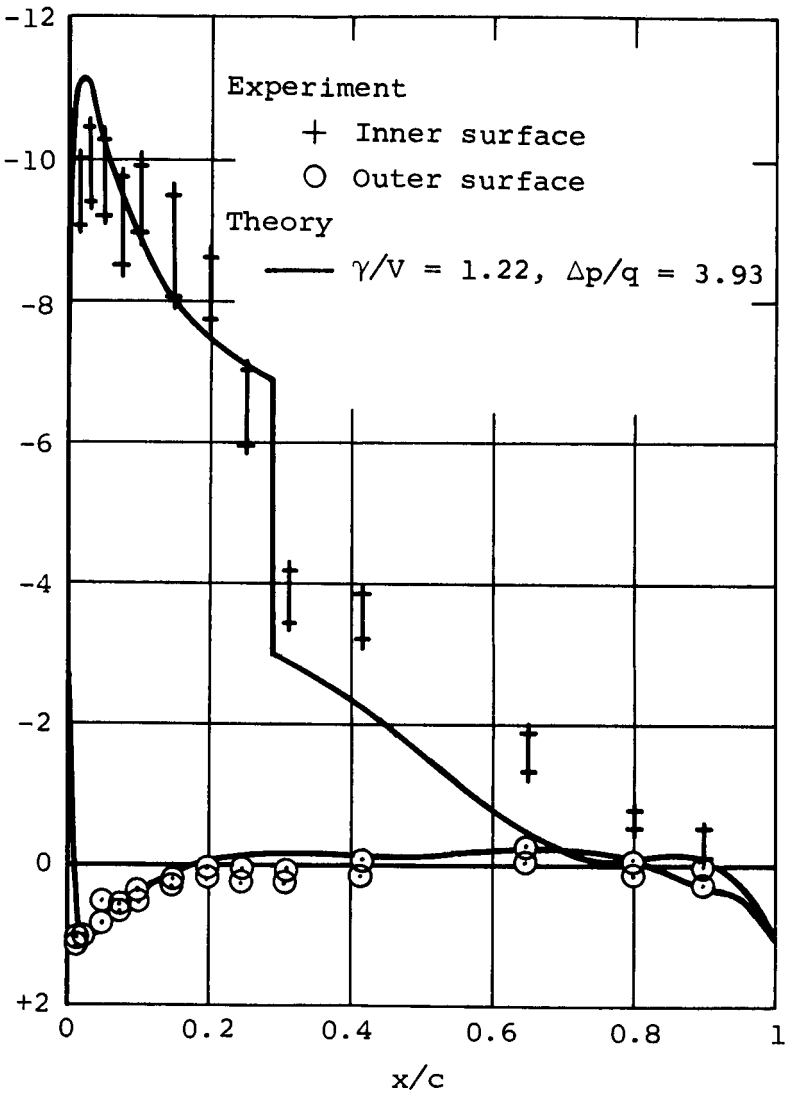

(b) $J = 0.342$, $C_{T_{DP}} = 4.14$.

Figure 10.- Continued.

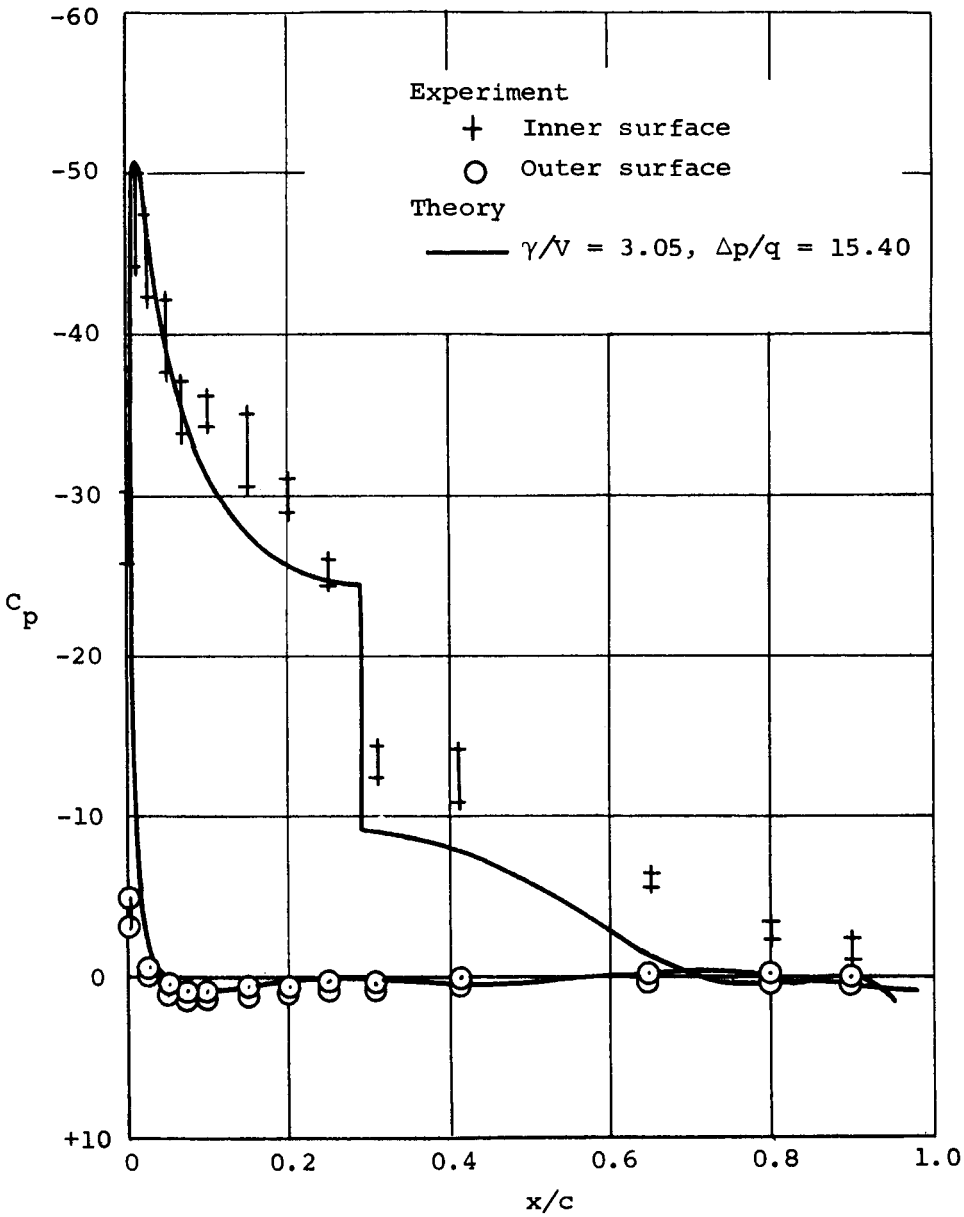

(c) J = 0.178, $C_{T_{DP}}$ = 19.4.

Figure 10.- Continued.

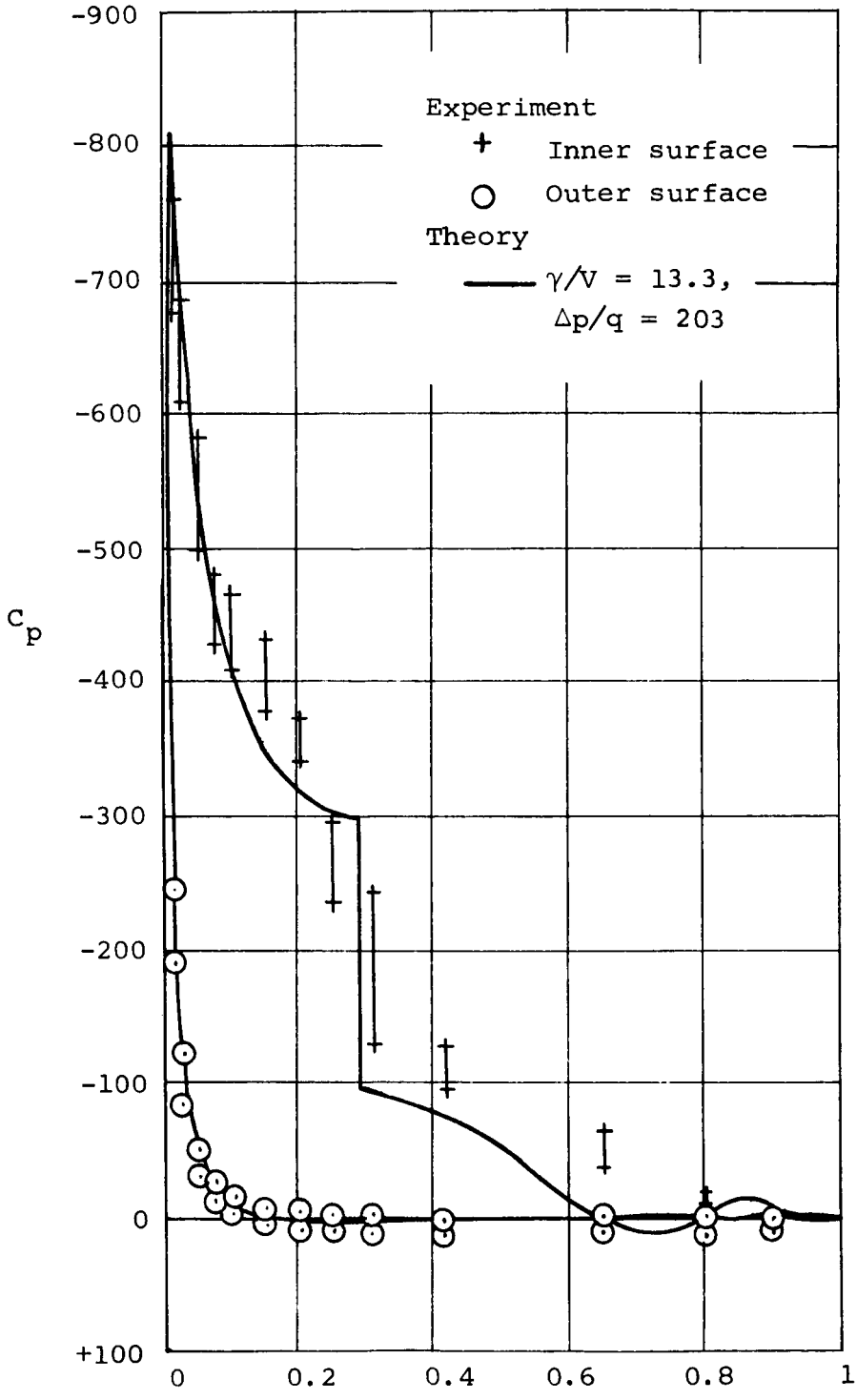

(d) $J \simeq 0$, $C_{T_{DP}} = 306.$

Figure 10.- Concluded.

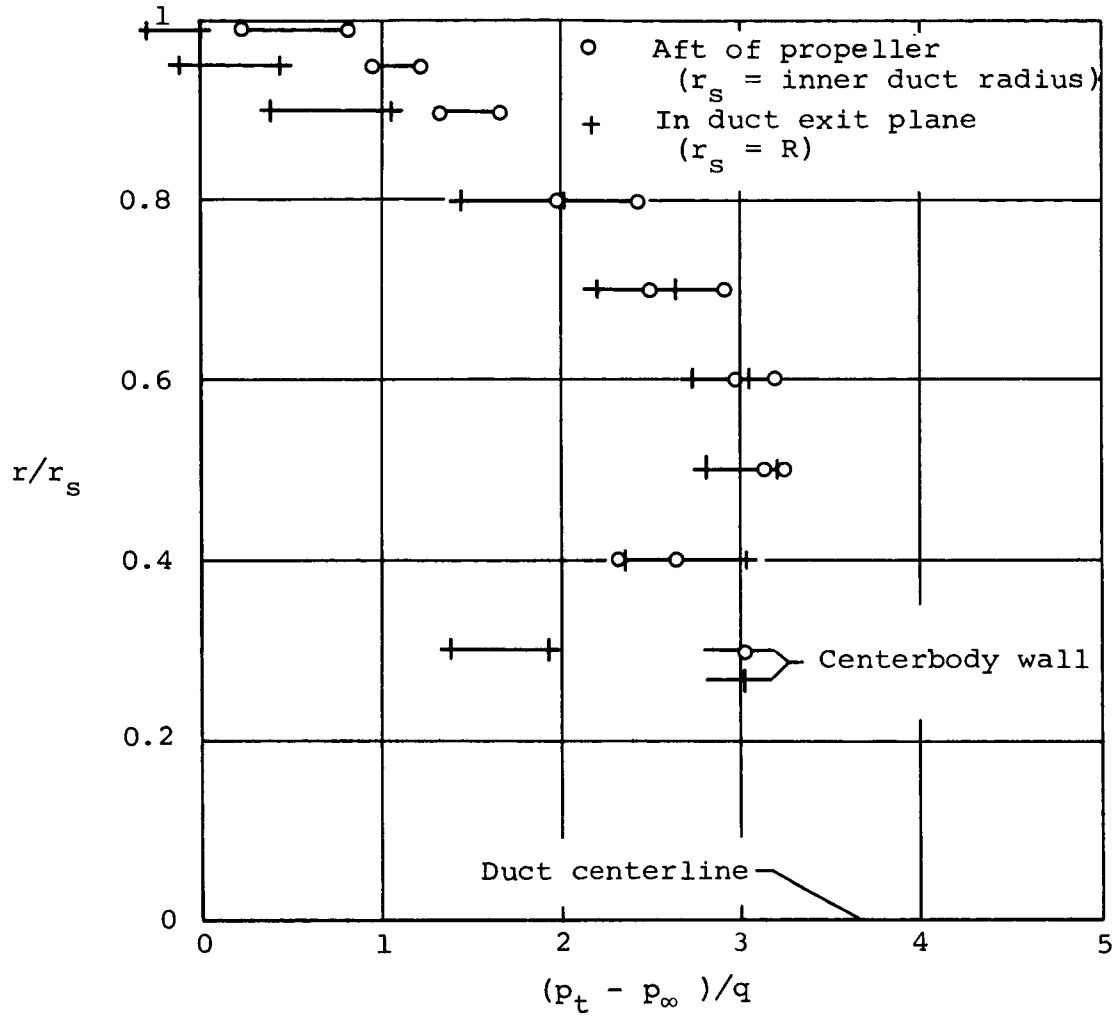

(a) J = 0.541, $C_{T_{DP}}$ = 0.890.

Figure 11.- Total pressure distributions measured across the 4-foot model duct at α = 0.

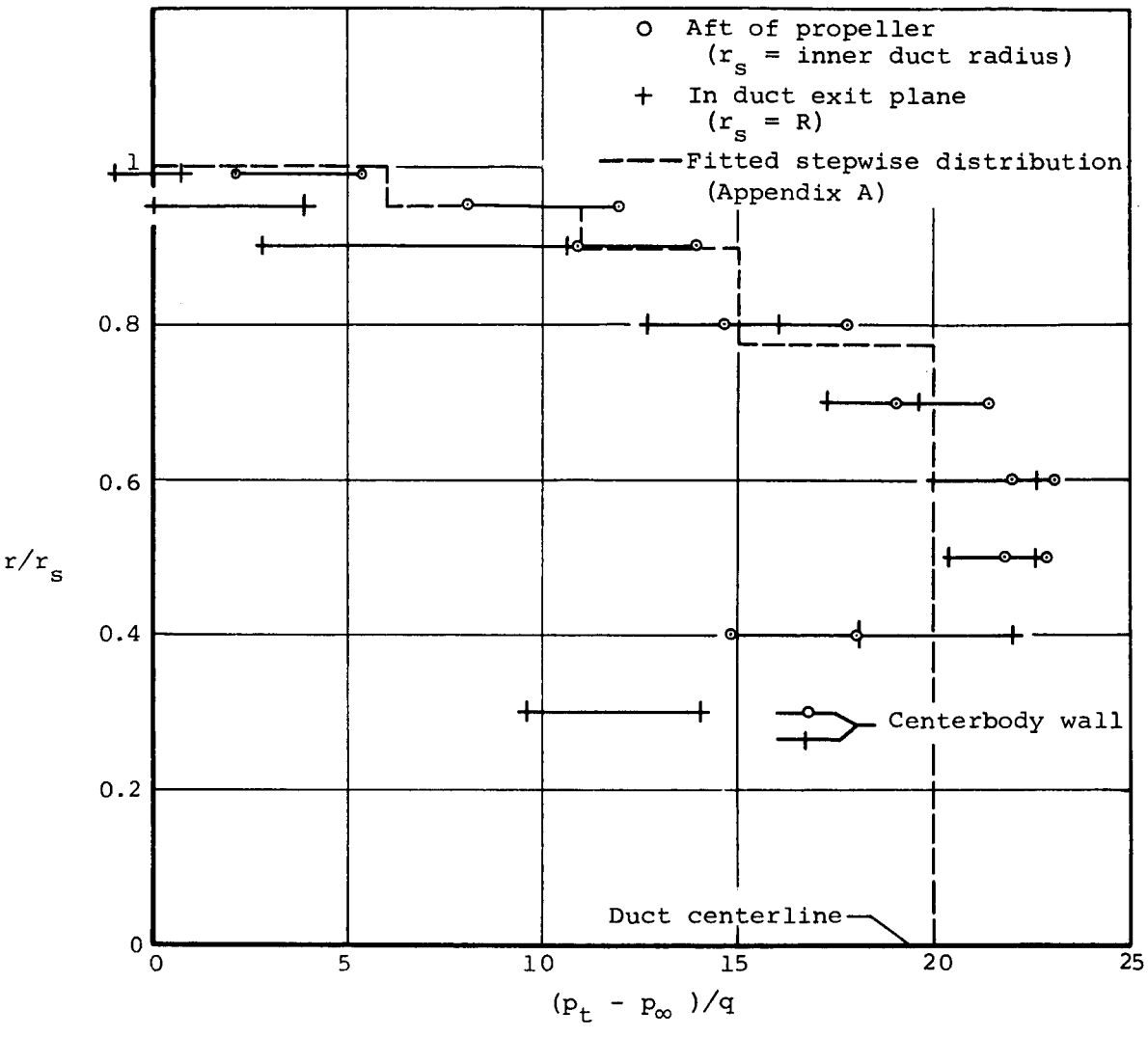

(b) $J = 0.178$, $C_{T_{DP}} = 19.4$.

Figure 11.- Concluded.

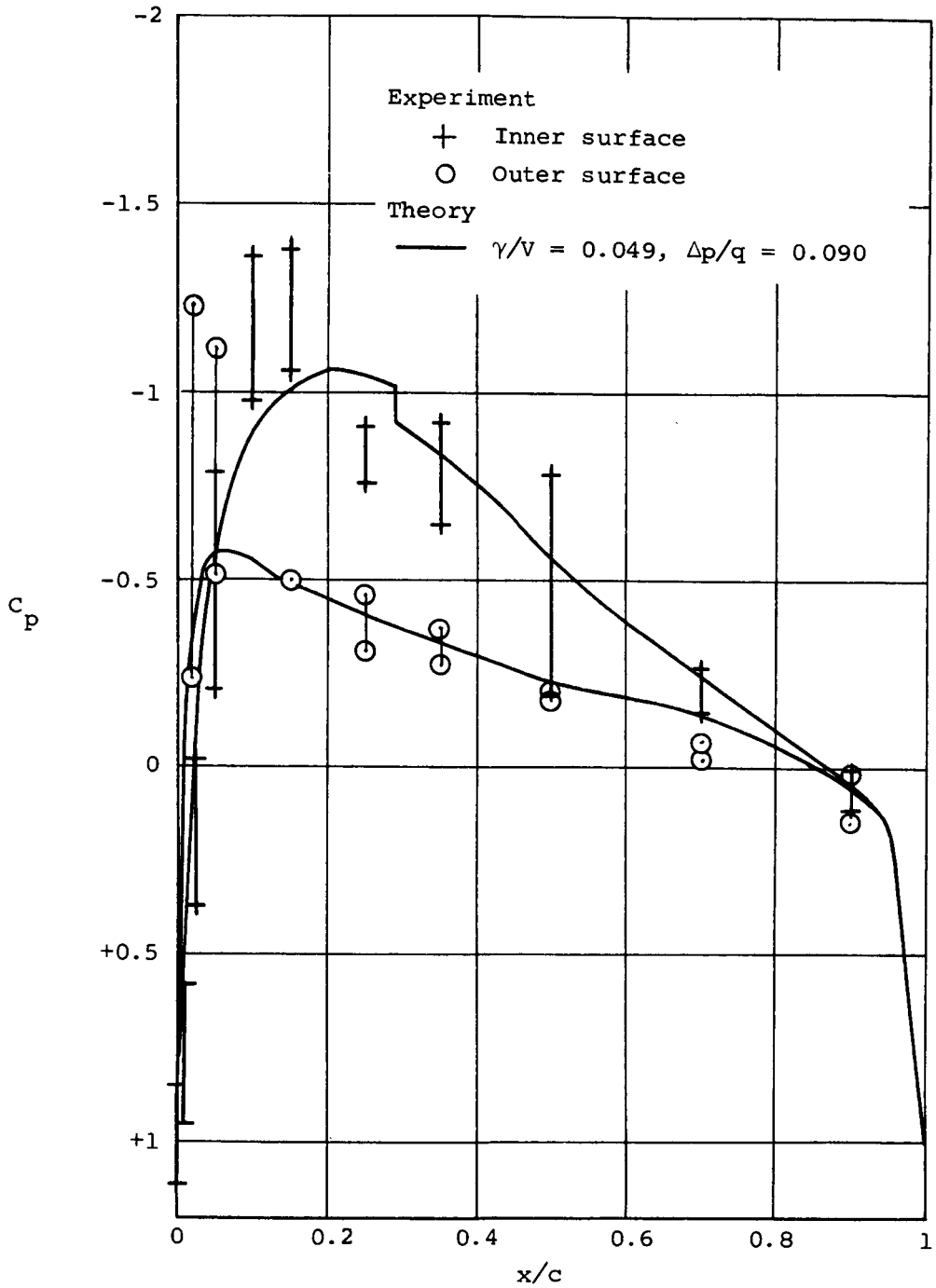

(a) J = 0.682, $C_{T_{DP}}$ = 0.083.

Figure 12.- Pressure distributions for the 7-foot model duct at $\alpha = 0^{\circ}$ with $\beta = 19^{\circ}$, $\delta_e = 0^{\circ}$.

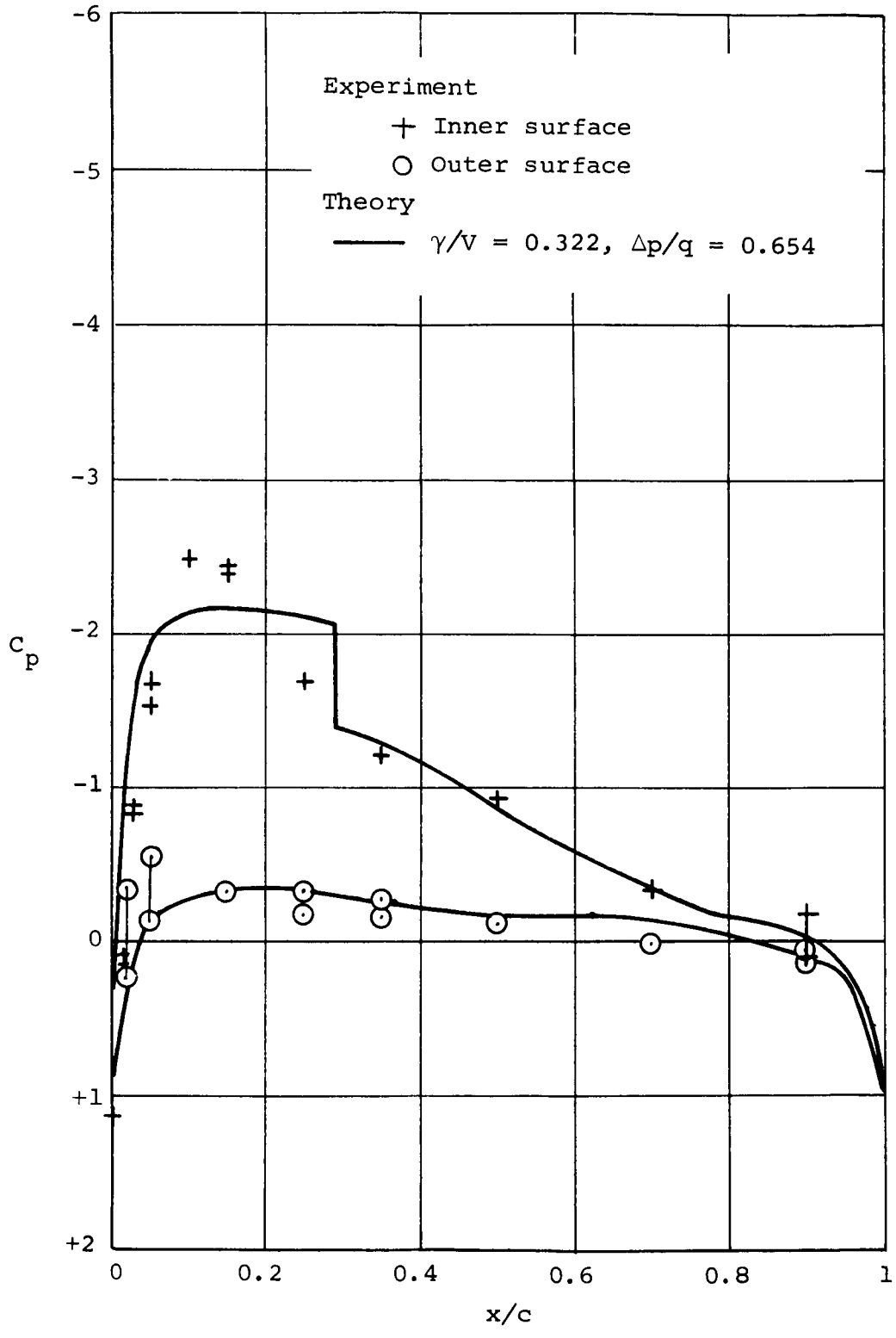

(b) J = 0.525, $C_{T_{DP}}$ = 0.682.

Figure 12.- Continued.

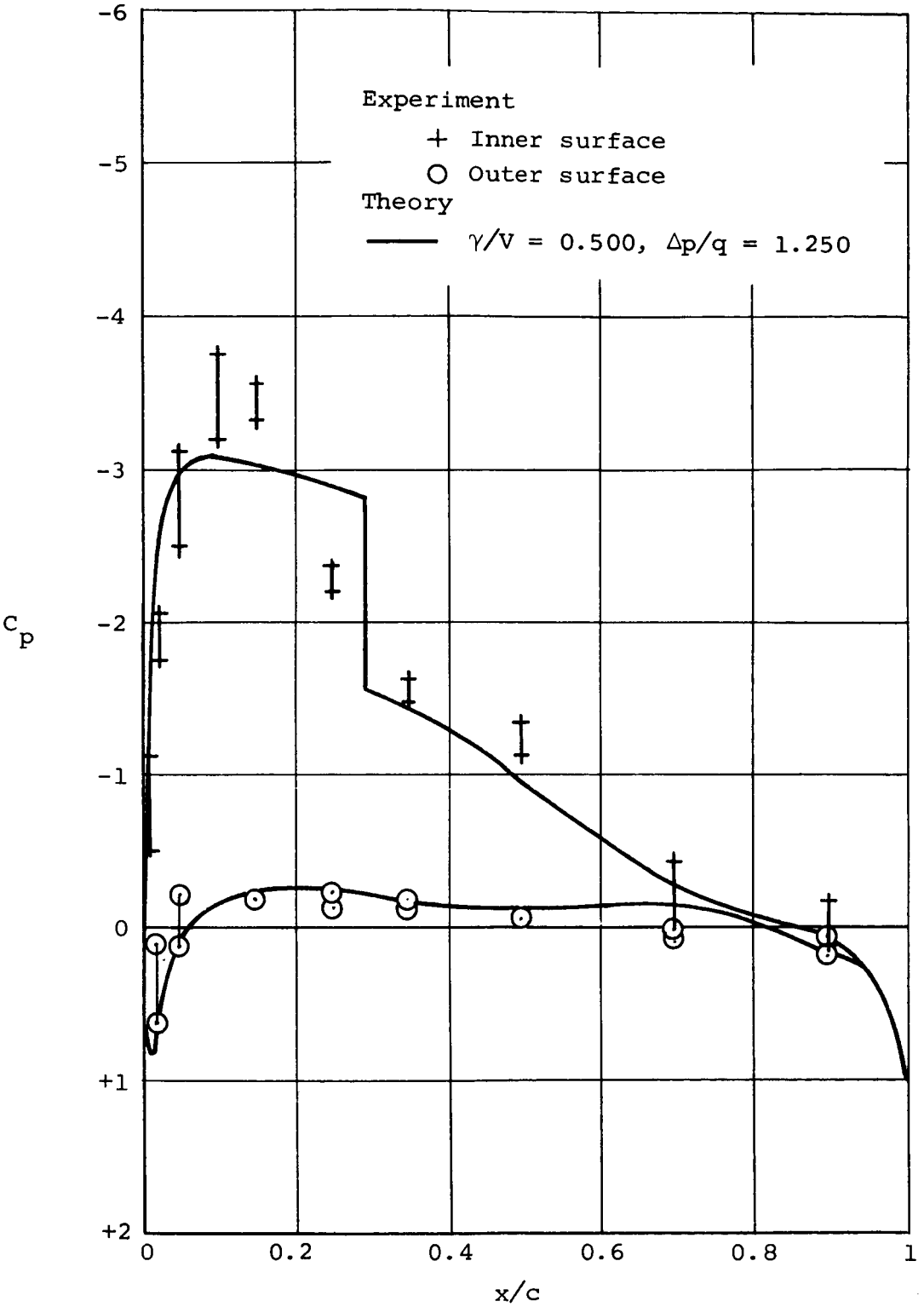

(c) J = 0.437, $C_{T_{DP}}$ = 1.21.

Figure 12.- Continued.

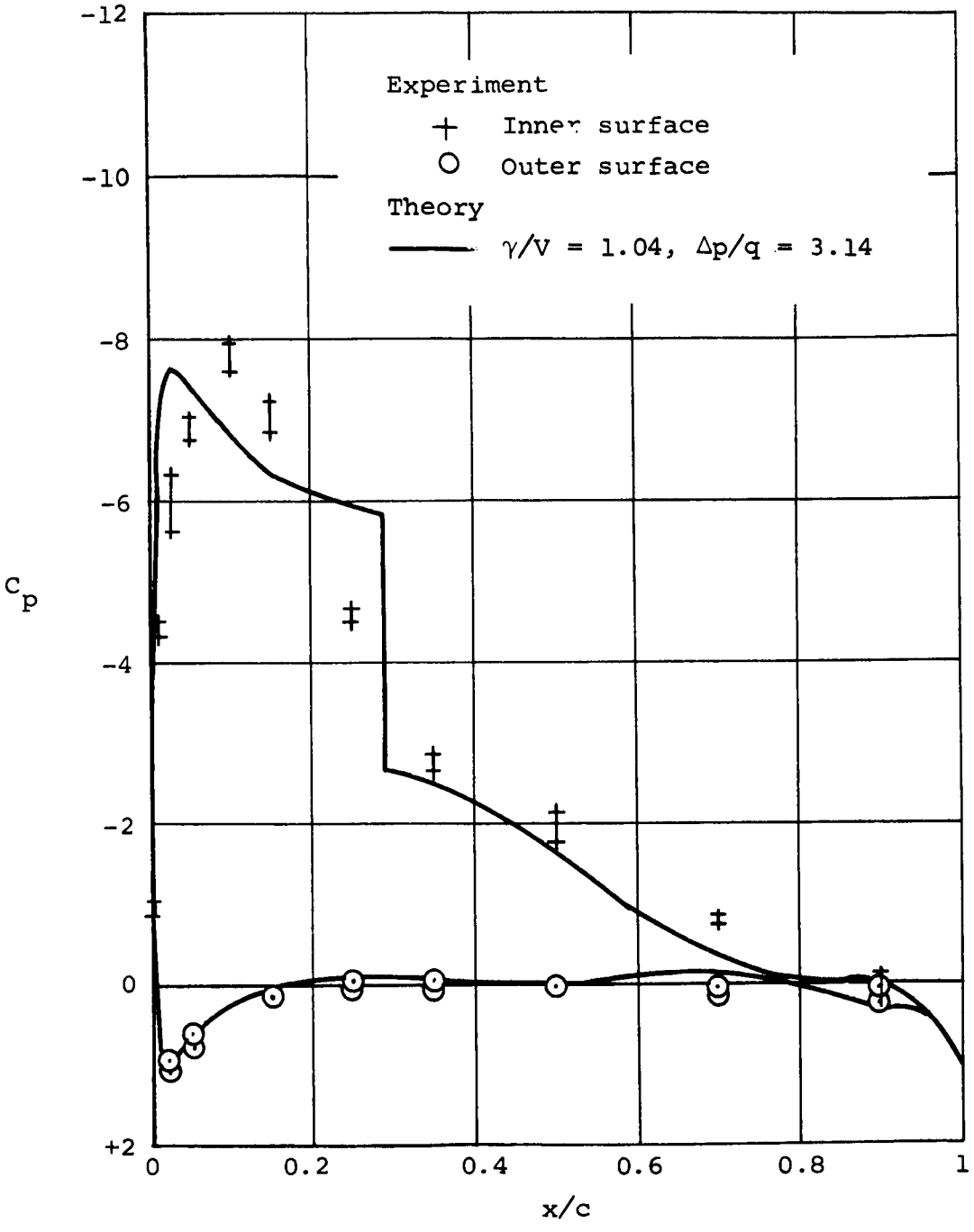

(d) J = 0.311, $C_{T_{DP}}$ = 3.46.

Figure 12.- Continued.

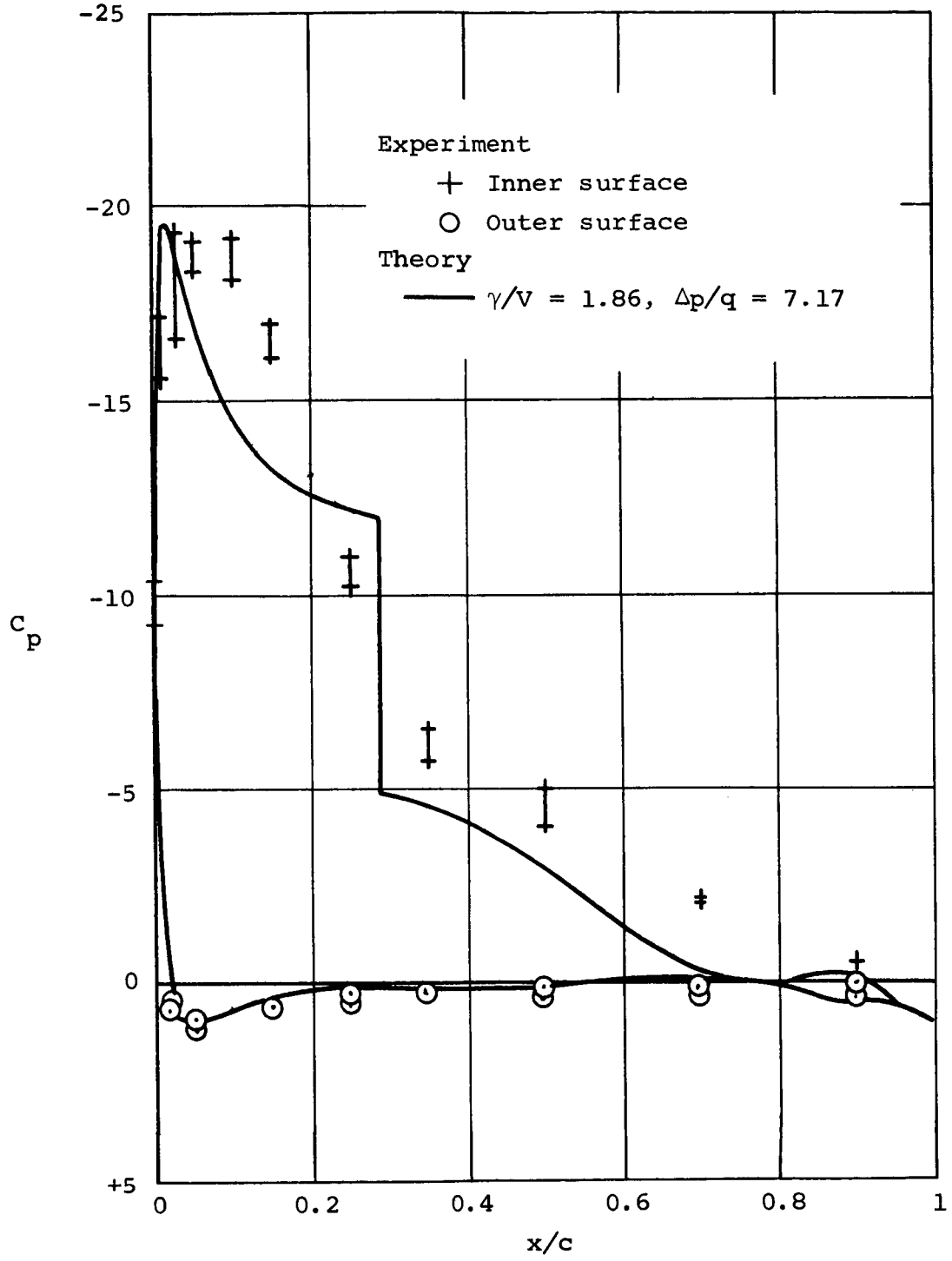

(e) J = 0.214, $C_{T_{DP}}$ = 8.80.

Figure 12.- Concluded.

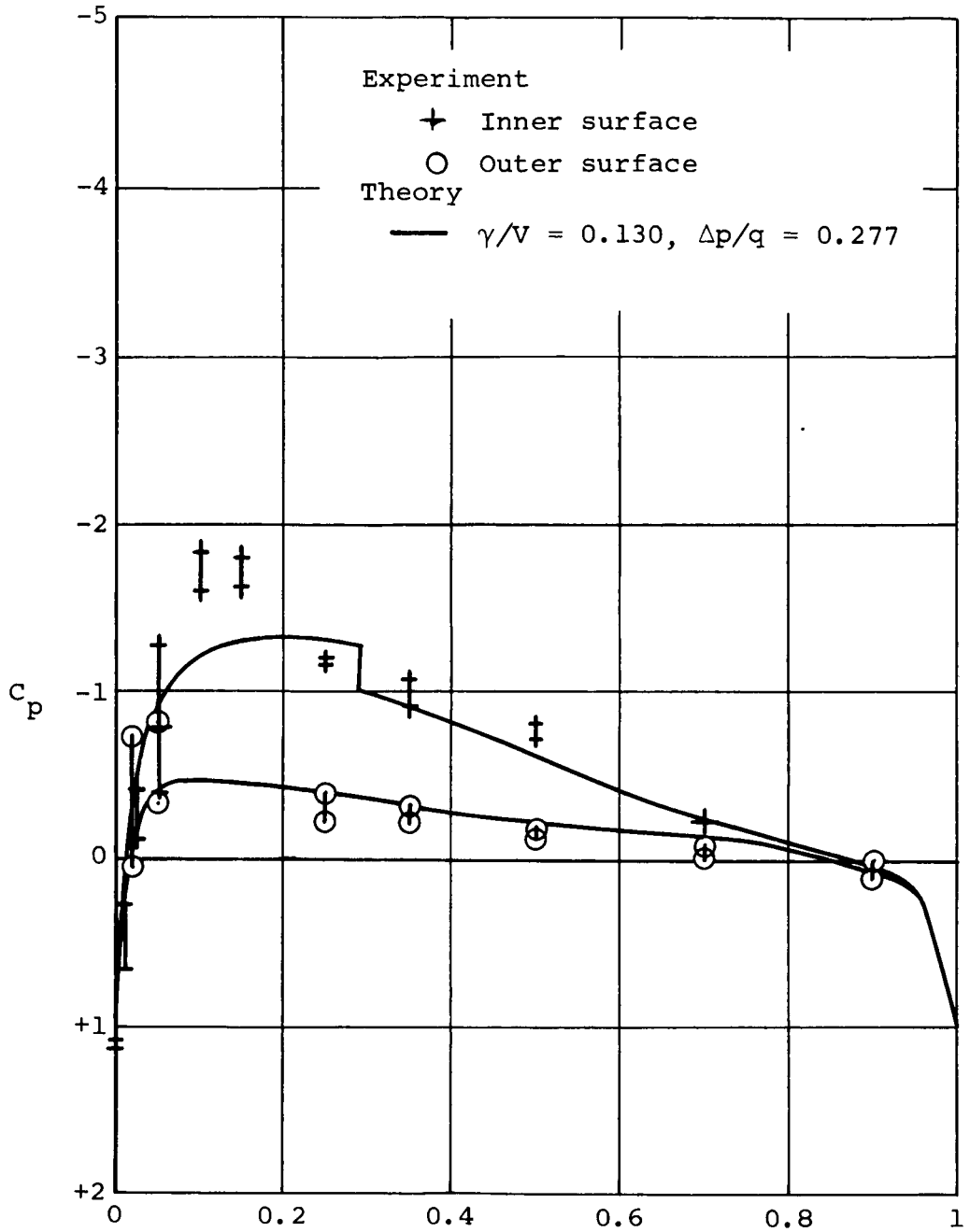

(a) J = 0.617, $C_{T_{DP}}$ = 0.220.

Figure 13.- Pressure distributions for the 7-foot model duct at $\alpha = 0^{\circ}$ with $\beta = 19^{\circ}$, elevon off.

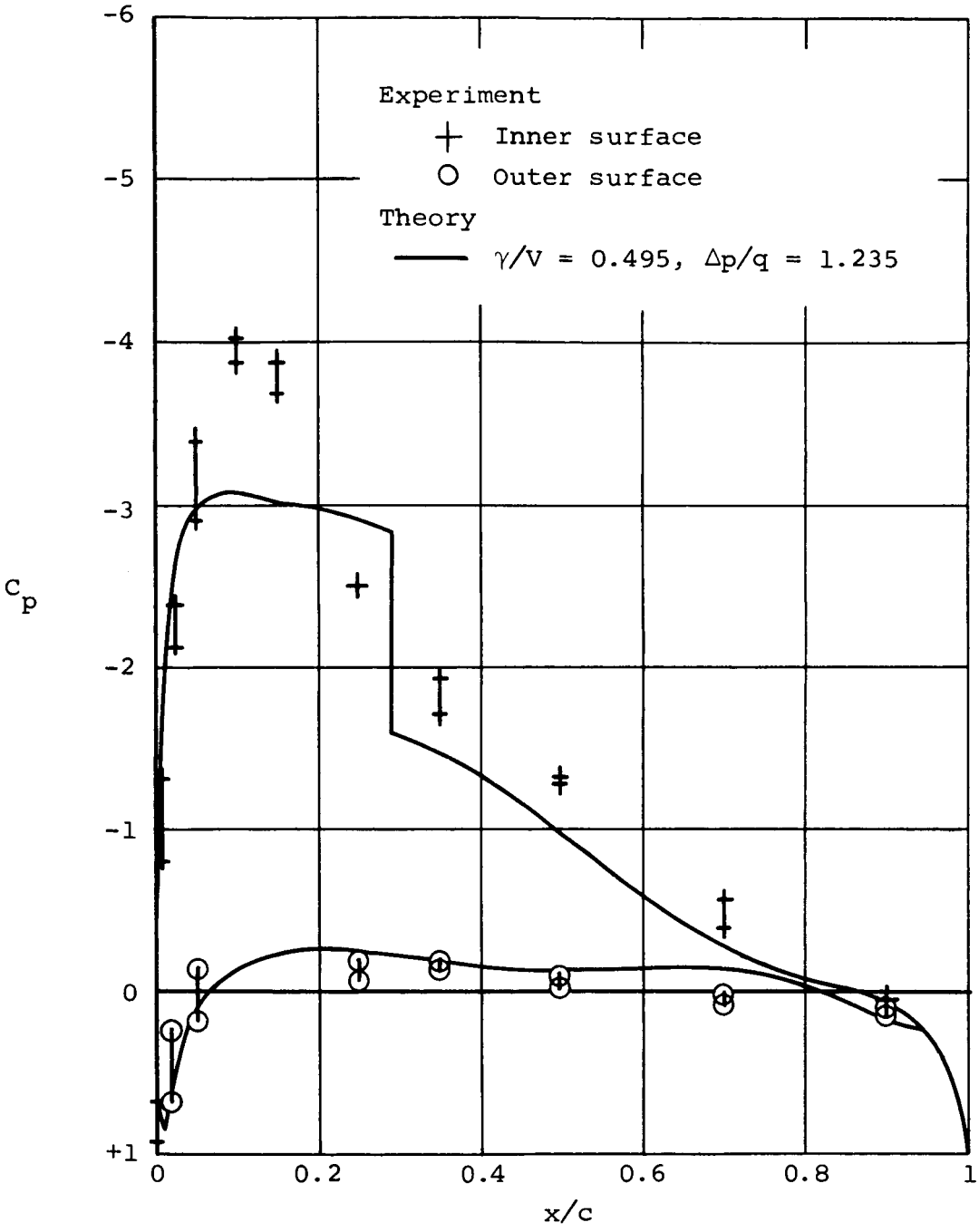

(b) J = 0.438, $C_{T_{DP}}$ = 1.19.

Figure 13.- Continued.

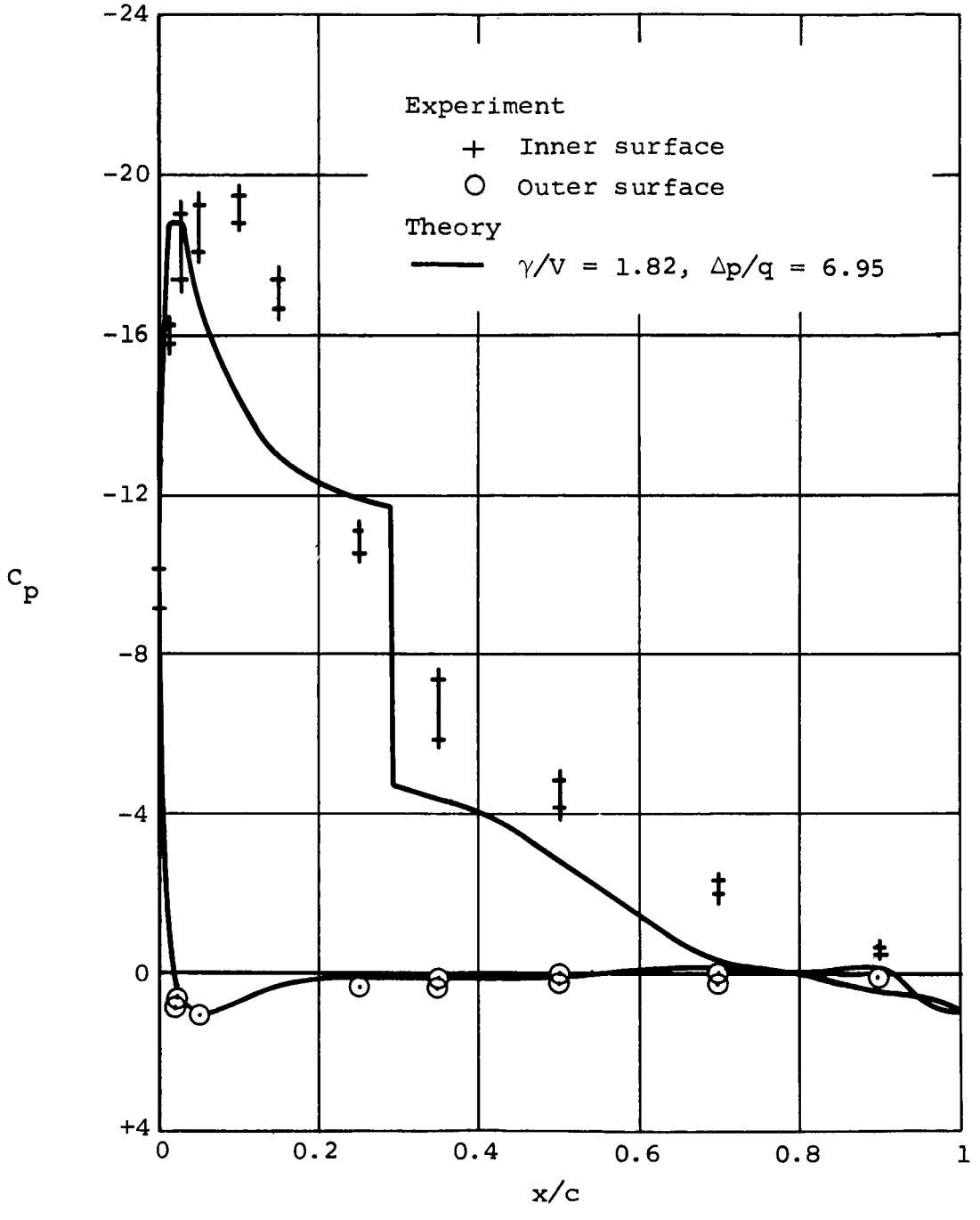

(c) J = 0.219, $C_{T_{DP}}$ = 8.46.

Figure 13.- Concluded.

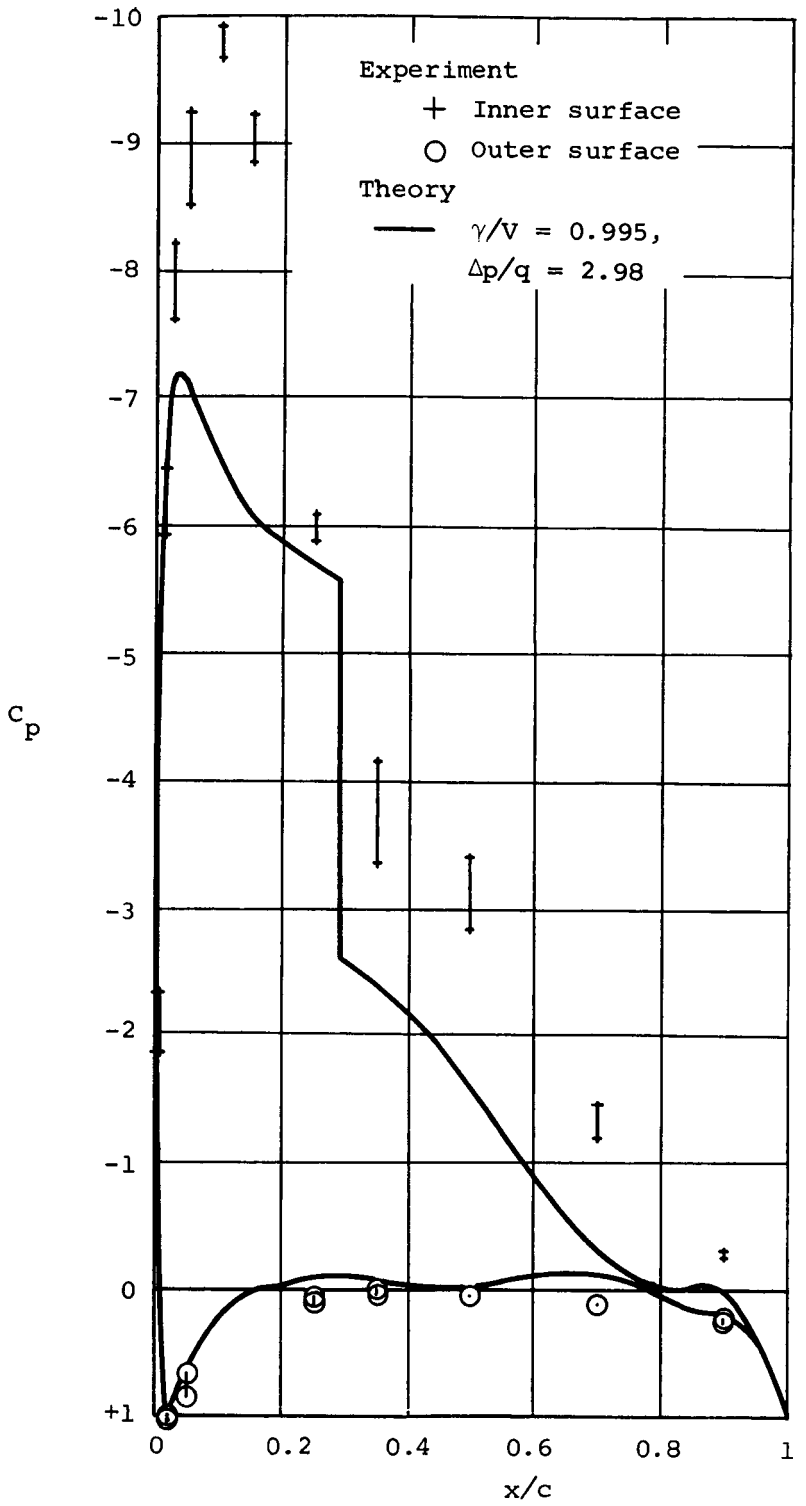

(a) J = 0.432, $C_{T_{DP}}$ = 3.26.

Figure 14.- Pressure distributions for the 7-foot model duct at $\alpha = 0^{\circ}$ with $\beta = 29^{\circ}$, elevon off.

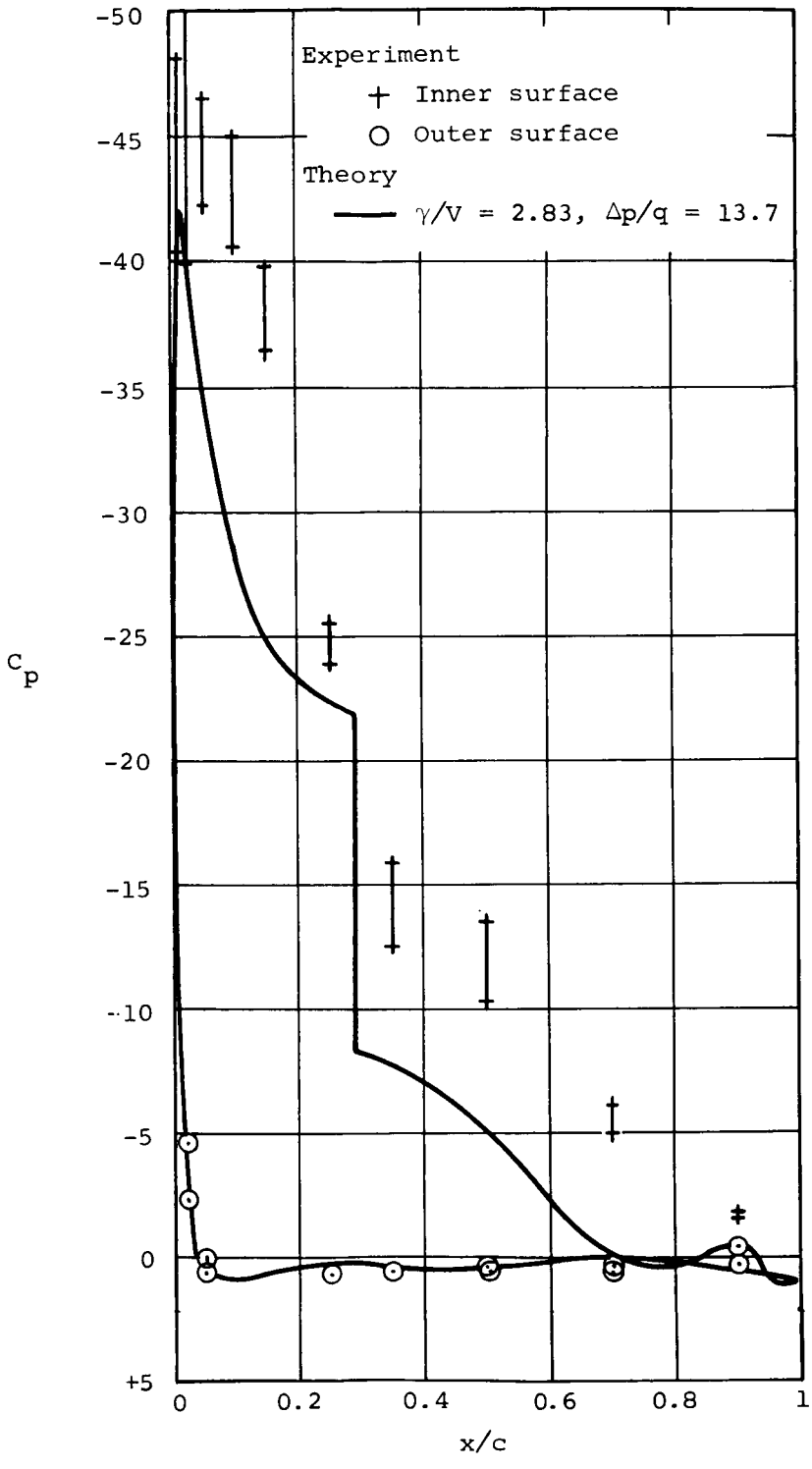

(b) J = 0.216, $C_{T_{DP}}$ = 18.1.

Figure 14.- Continued.

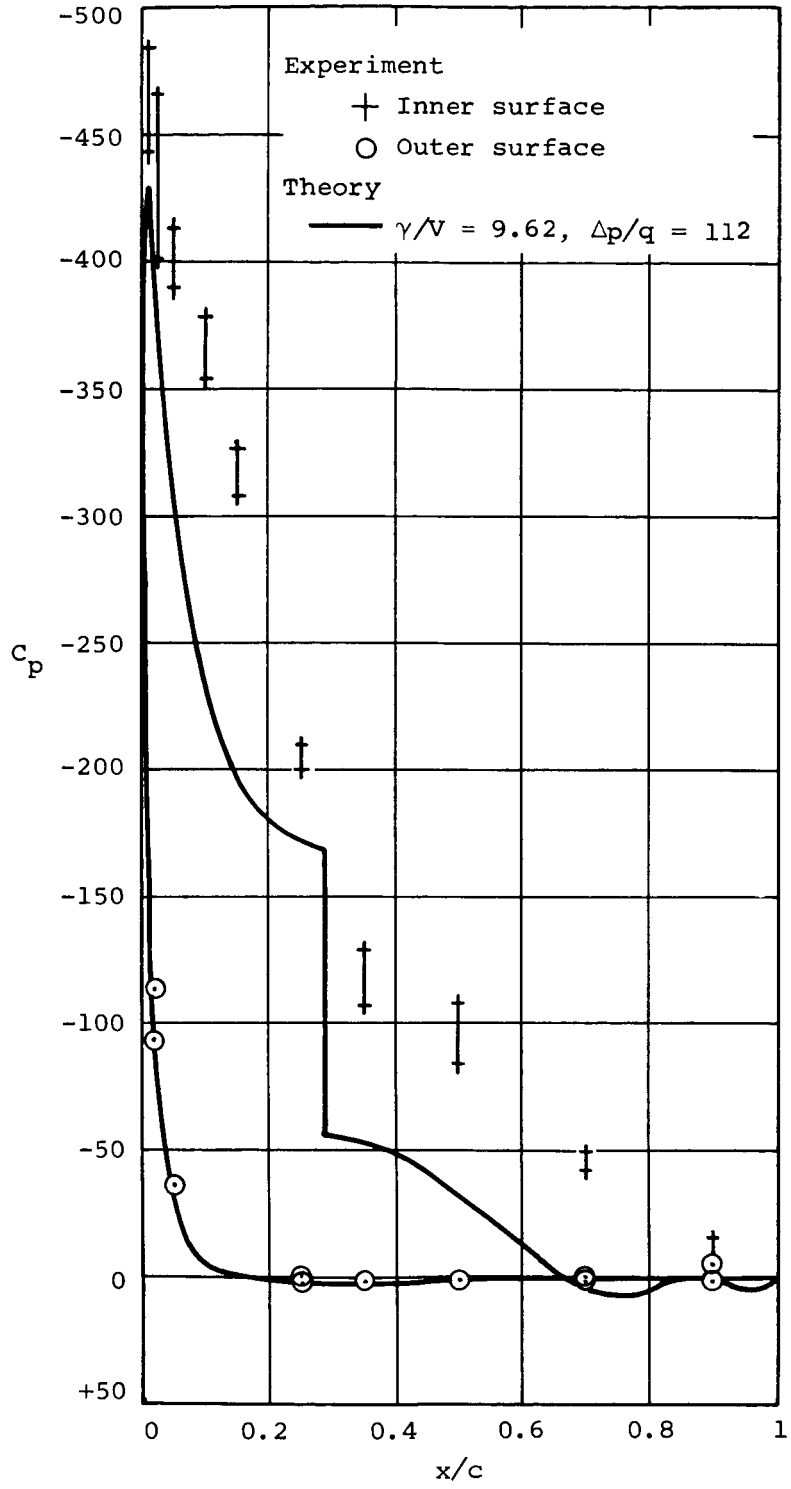

(c) J = 0.077, $C_{T_{DP}}$ = 173.

Figure 14.- Concluded.

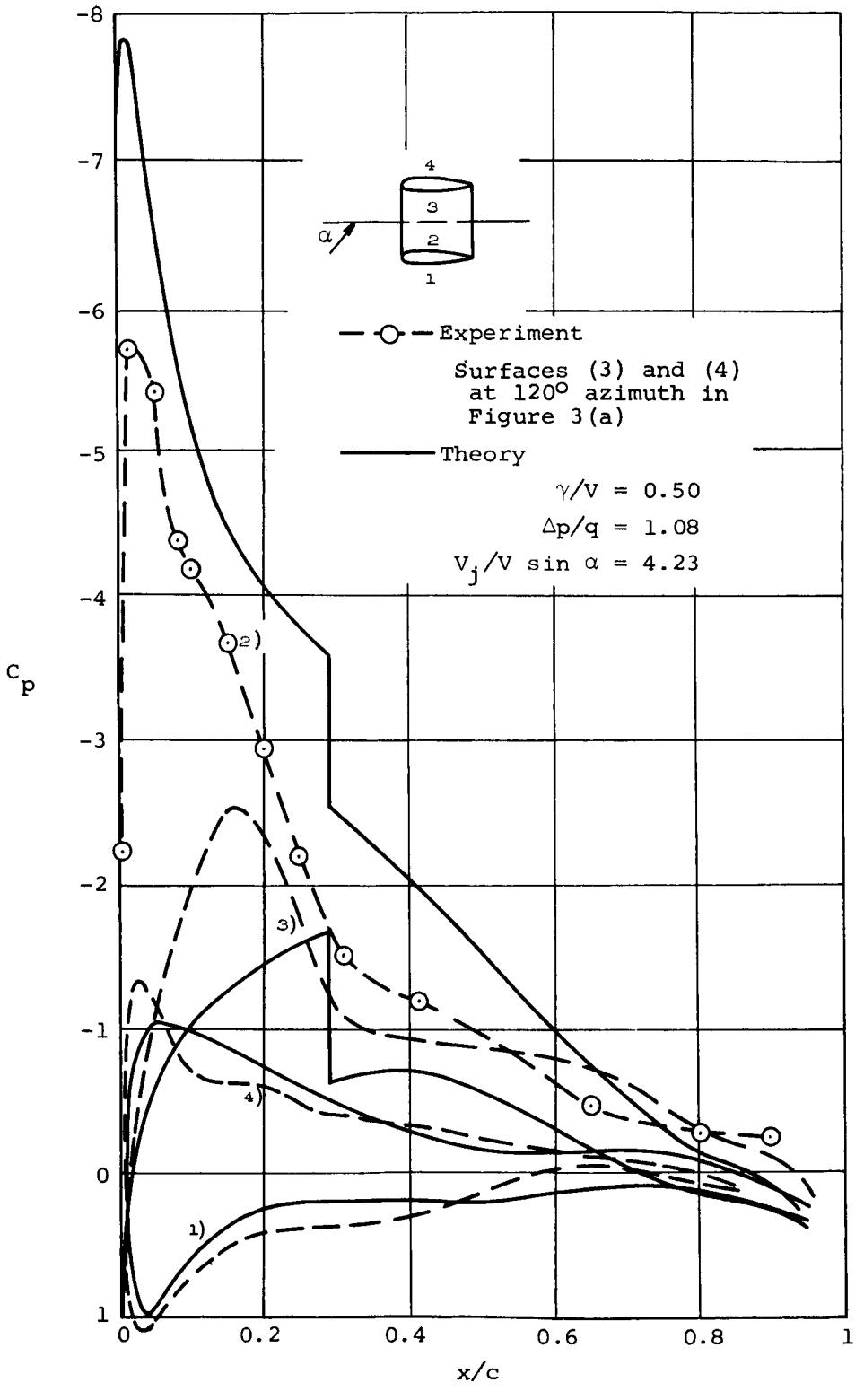

(a) $\alpha = 20^\circ$, $J = 0.542$, $C_{T_{DP}} = 1.21$.

Figure 15.- Pressure distributions for the 4-foot model duct at $\alpha > 0$, $J \simeq 0.54$.

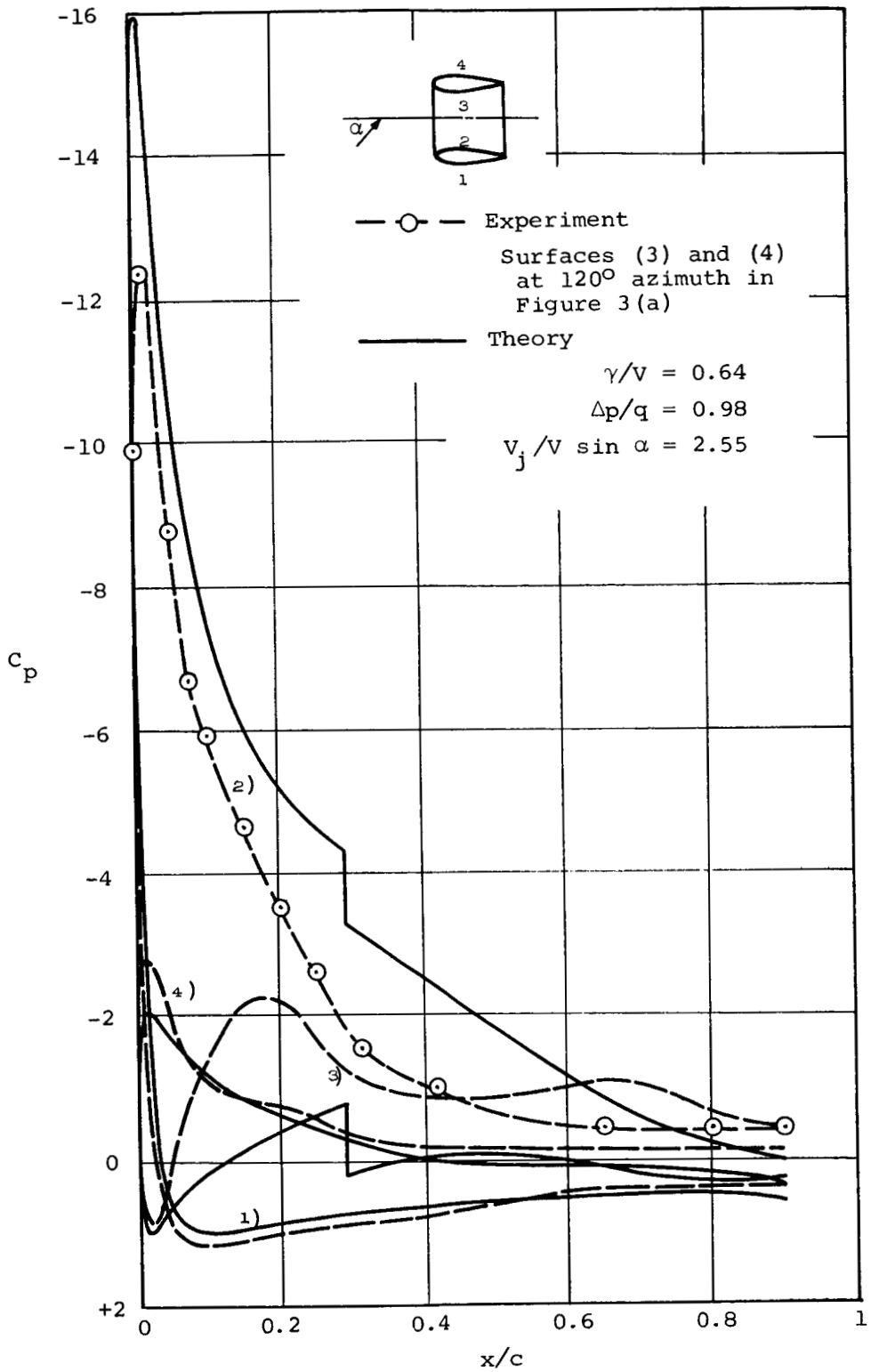

(b) $\alpha = 40^{\circ}$, $J = 0.540$, $C_{T_{DP}} = 1.87$.

Figure 15.- Concluded.

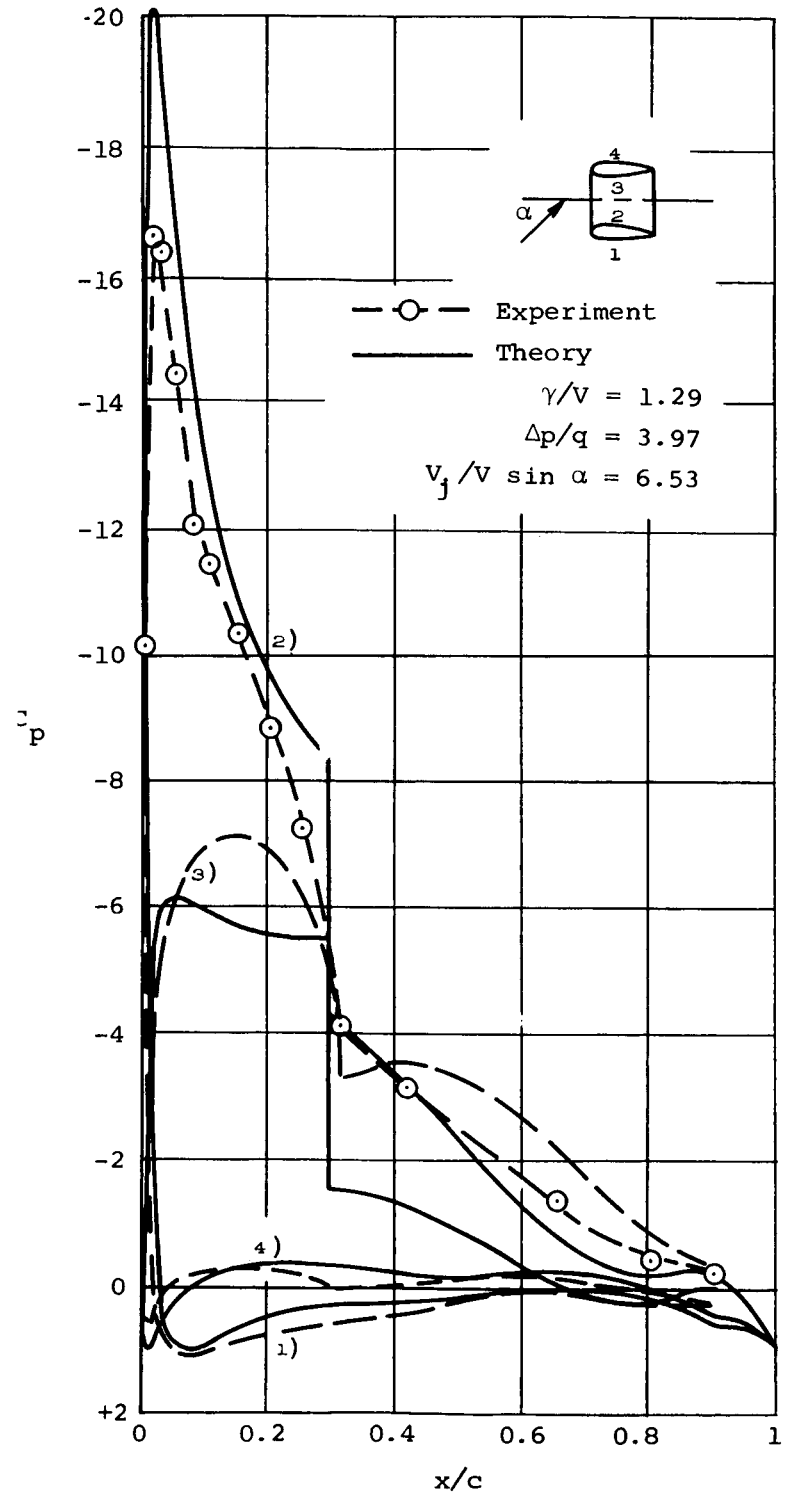

(a) $\alpha = 20^{\circ}$, $J = 0.342$, $C_{T_{DP}} = 4.56$.

Figure 16.- Pressure distributions for the 4-foot model duct at $\alpha > 0$, $J \simeq 0.34$.

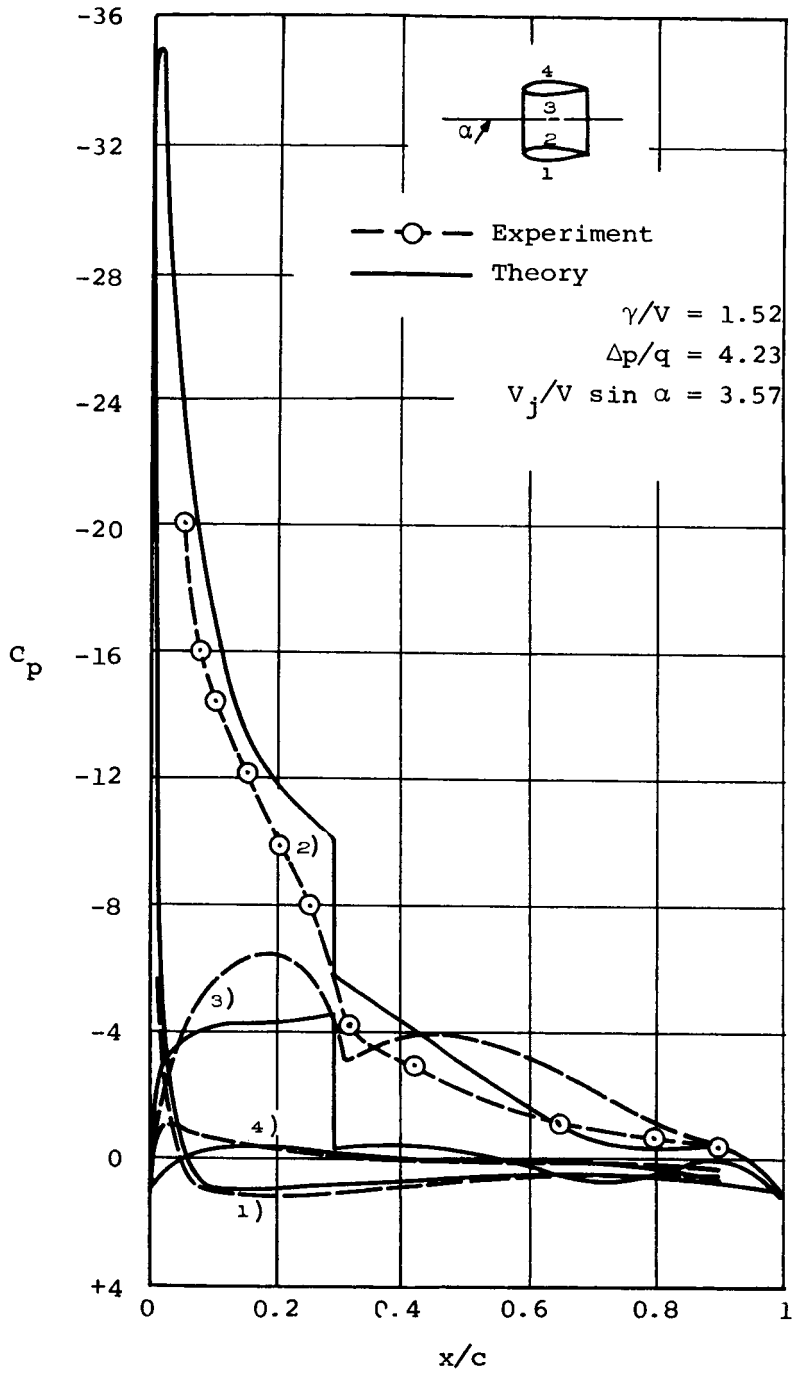

(b) $\alpha = 40^{\circ}$, $J = 0.341$, $C_{T_{DP}} = 5.93$.

Figure 16.- Continued.

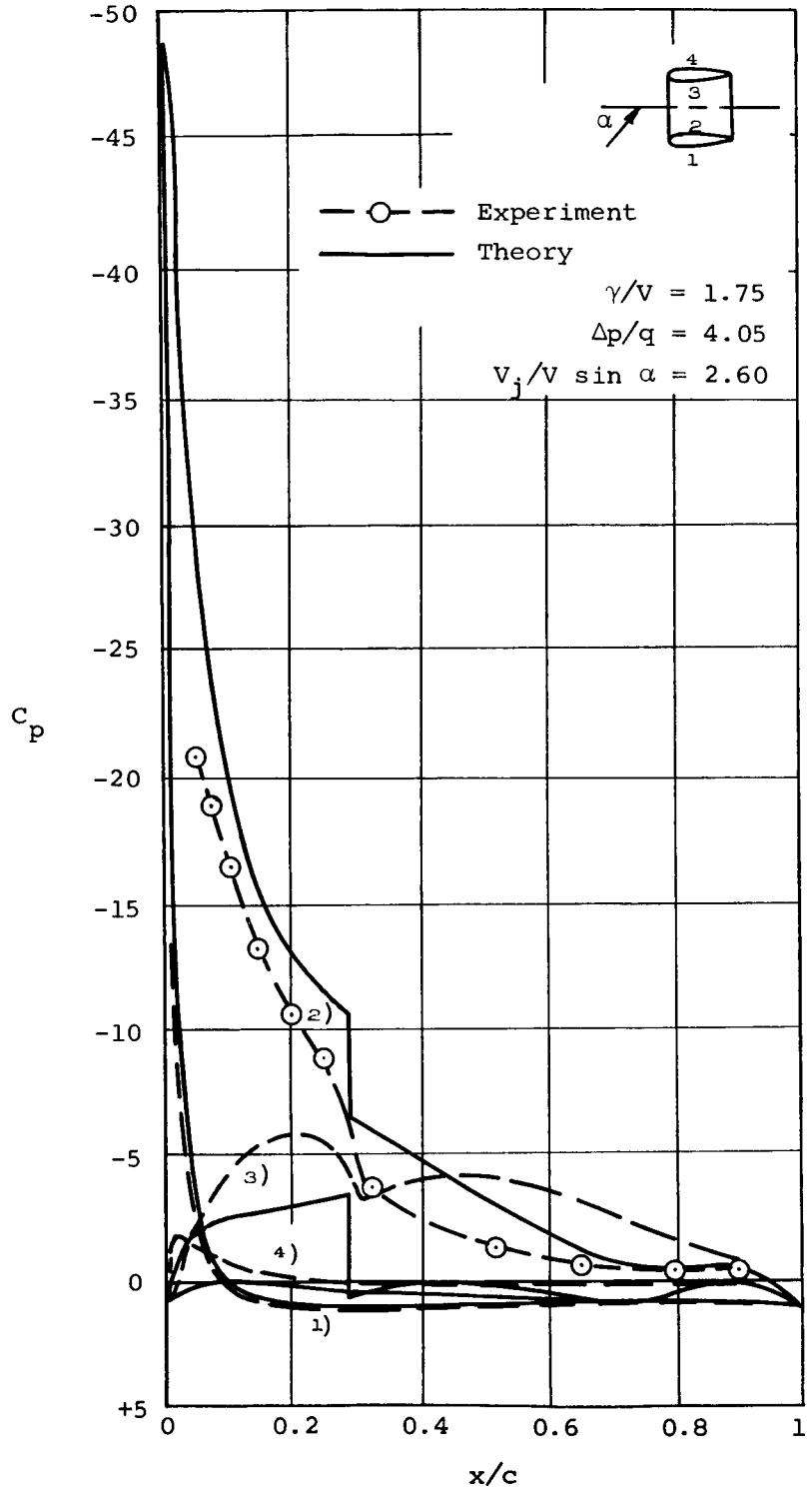

(c) $\alpha = 60^{\circ}$, $J = 0.346$, $C_{T_{DP}} = 7.15$.

Figure 16.- Concluded.

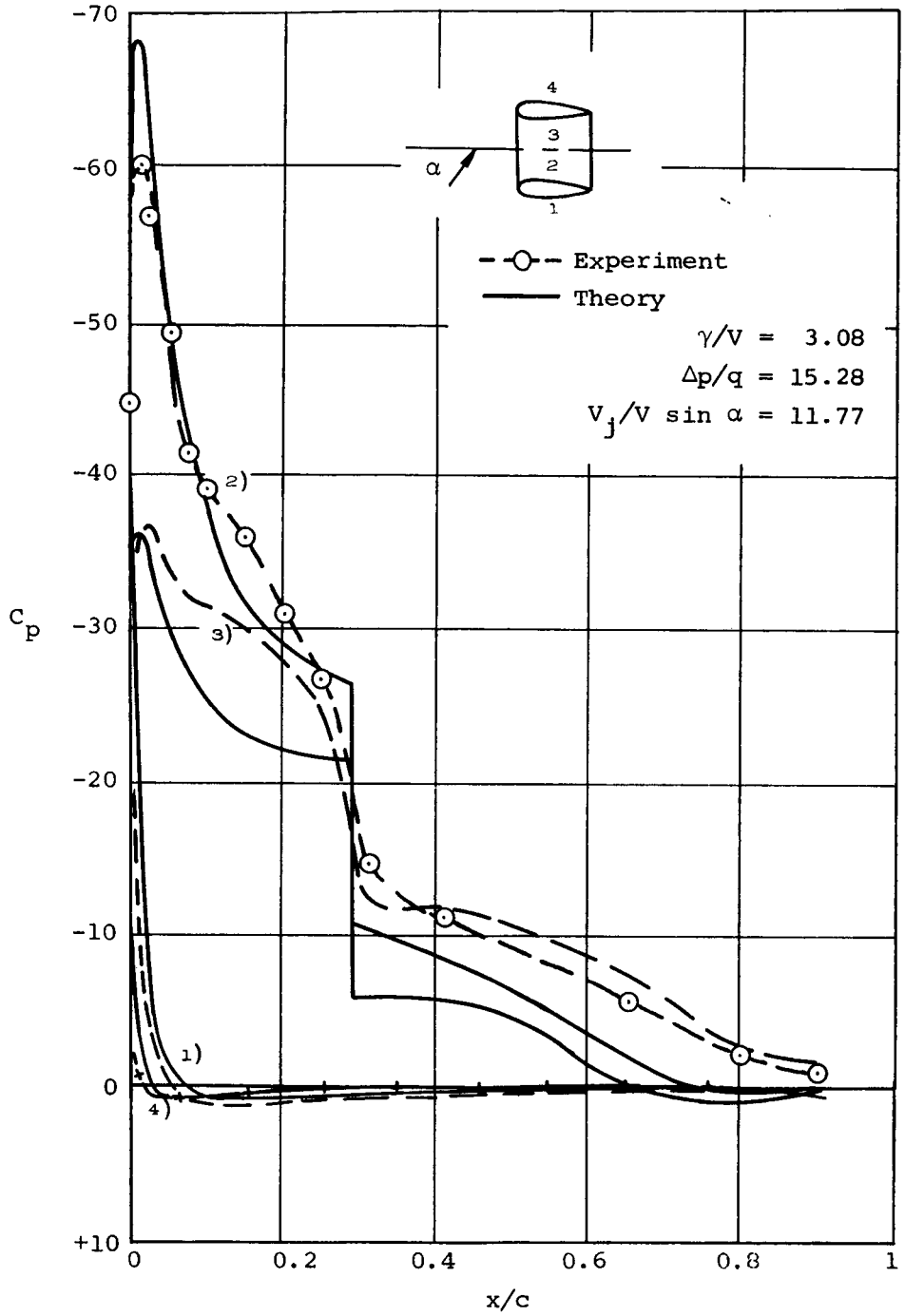

(a) $\alpha = 20^\circ$, $J = 0.178$, $C_{T_{DP}} = 19.5$.

Figure 17.- Pressure distributions for the 4-foot model duct at $\alpha > 0$, $J \simeq 0.17$.

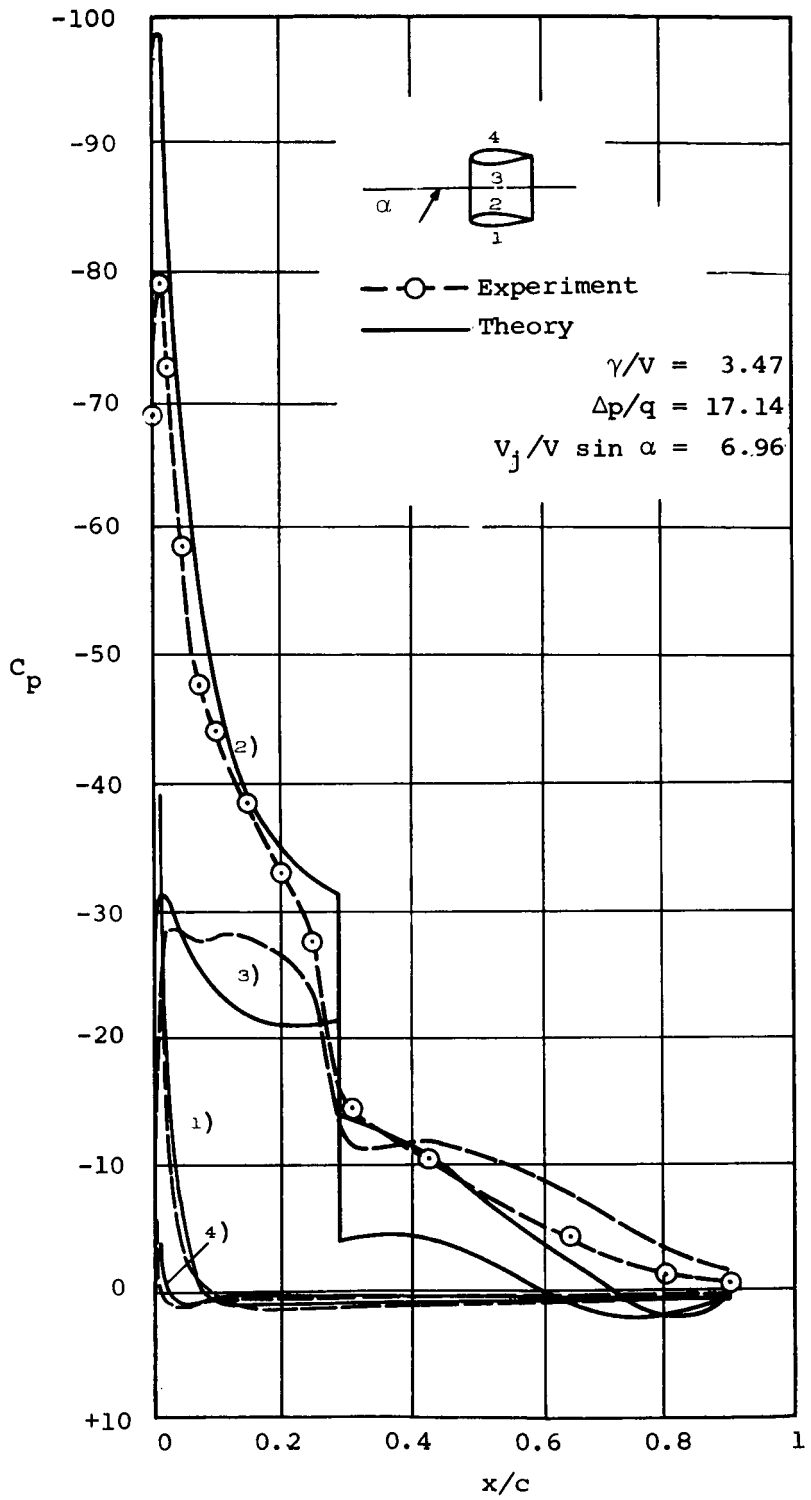

(b) $\alpha = 40^{\circ}$, J = 0.178, $C_{T_{DP}} = 21.2$.

Figure 17.- Continued.

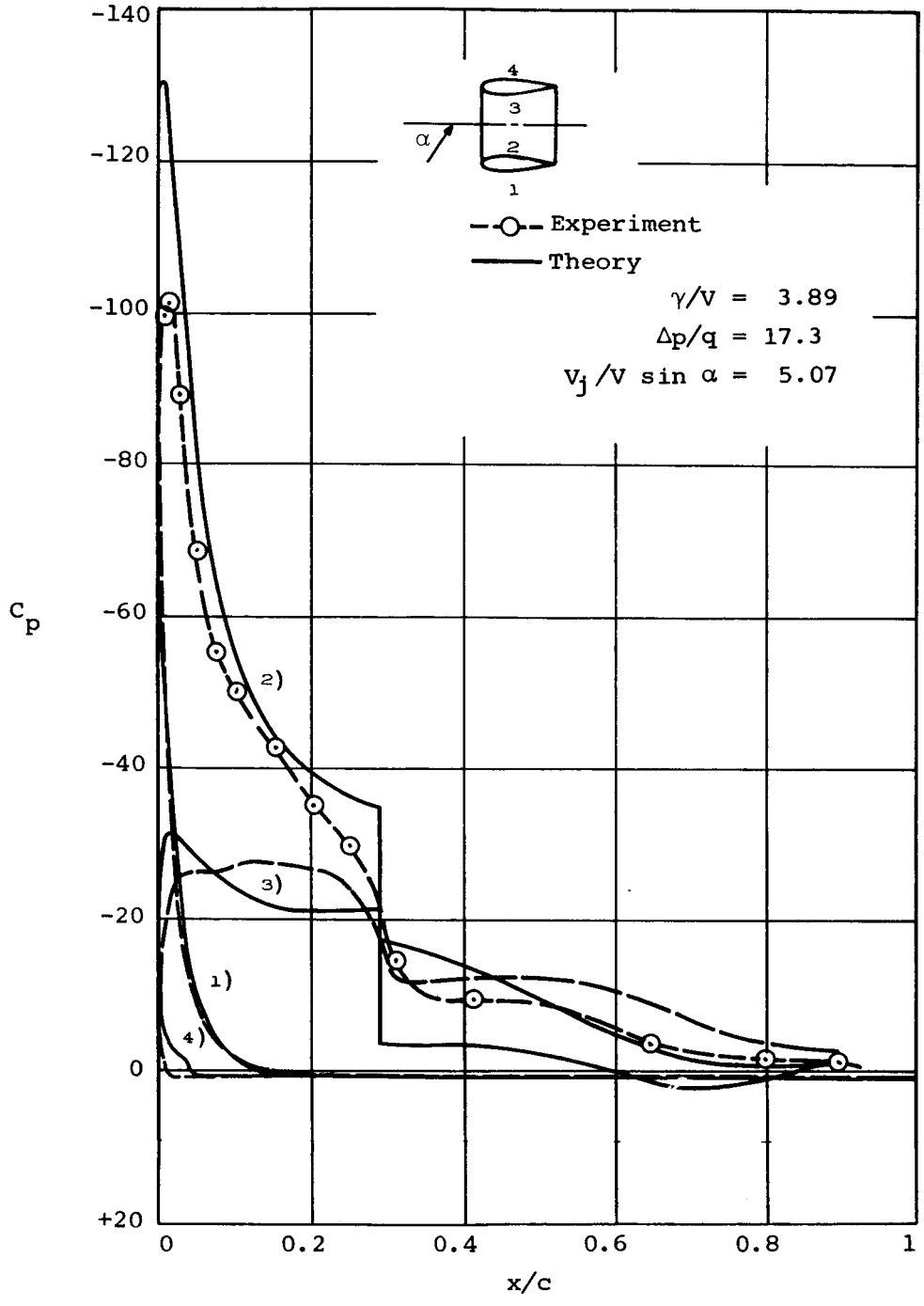

(c) $\alpha = 60^{\circ}$, $J = 0.176$, $C_{T_{DP}} = 25.5$.

Figure 17.- Continued.

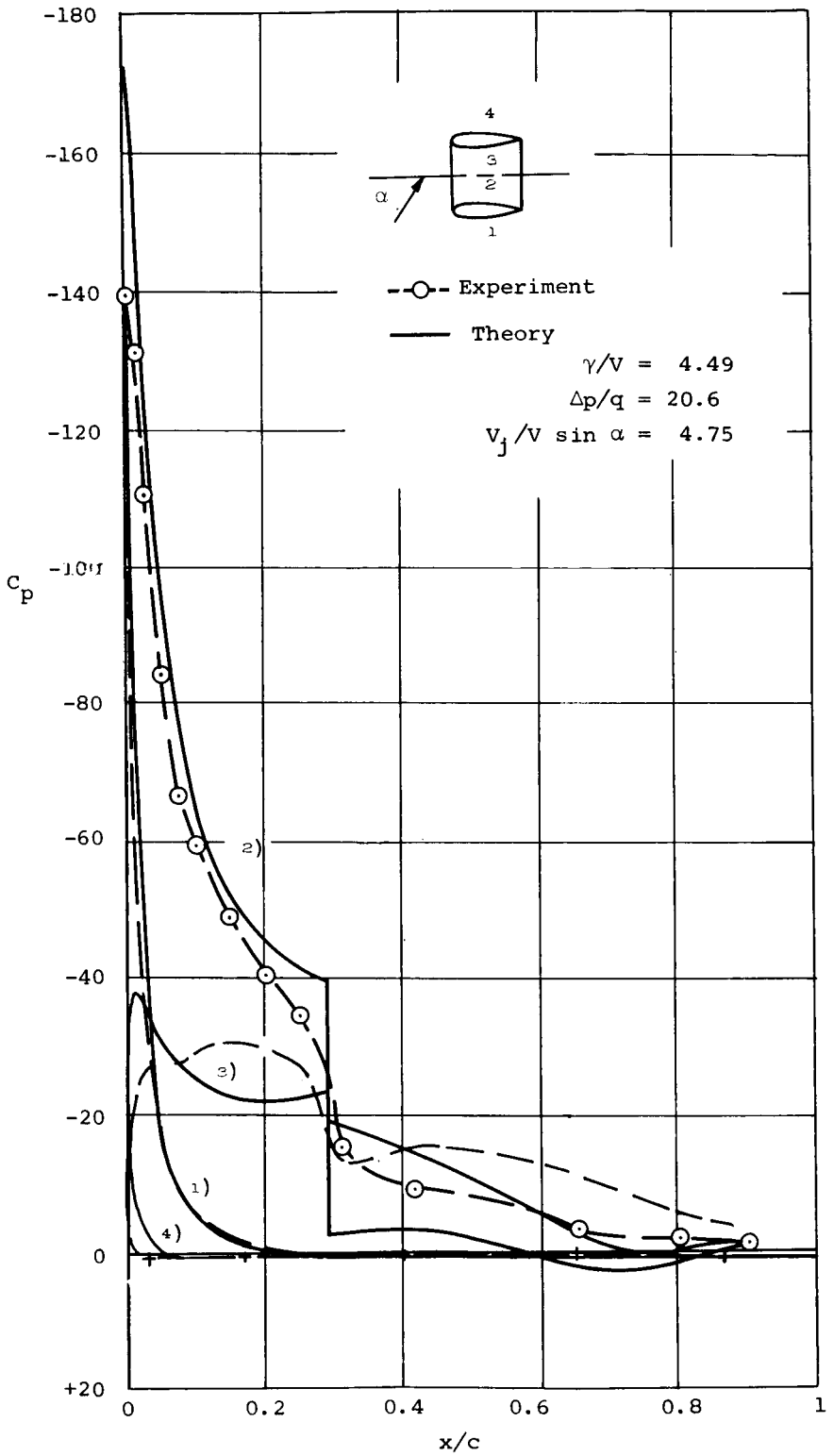

(d) $\alpha = 80^{\circ}$, $J = 0.166$, $C_{T_{DP}} = 34.1$.

Figure 17.- Concluded.

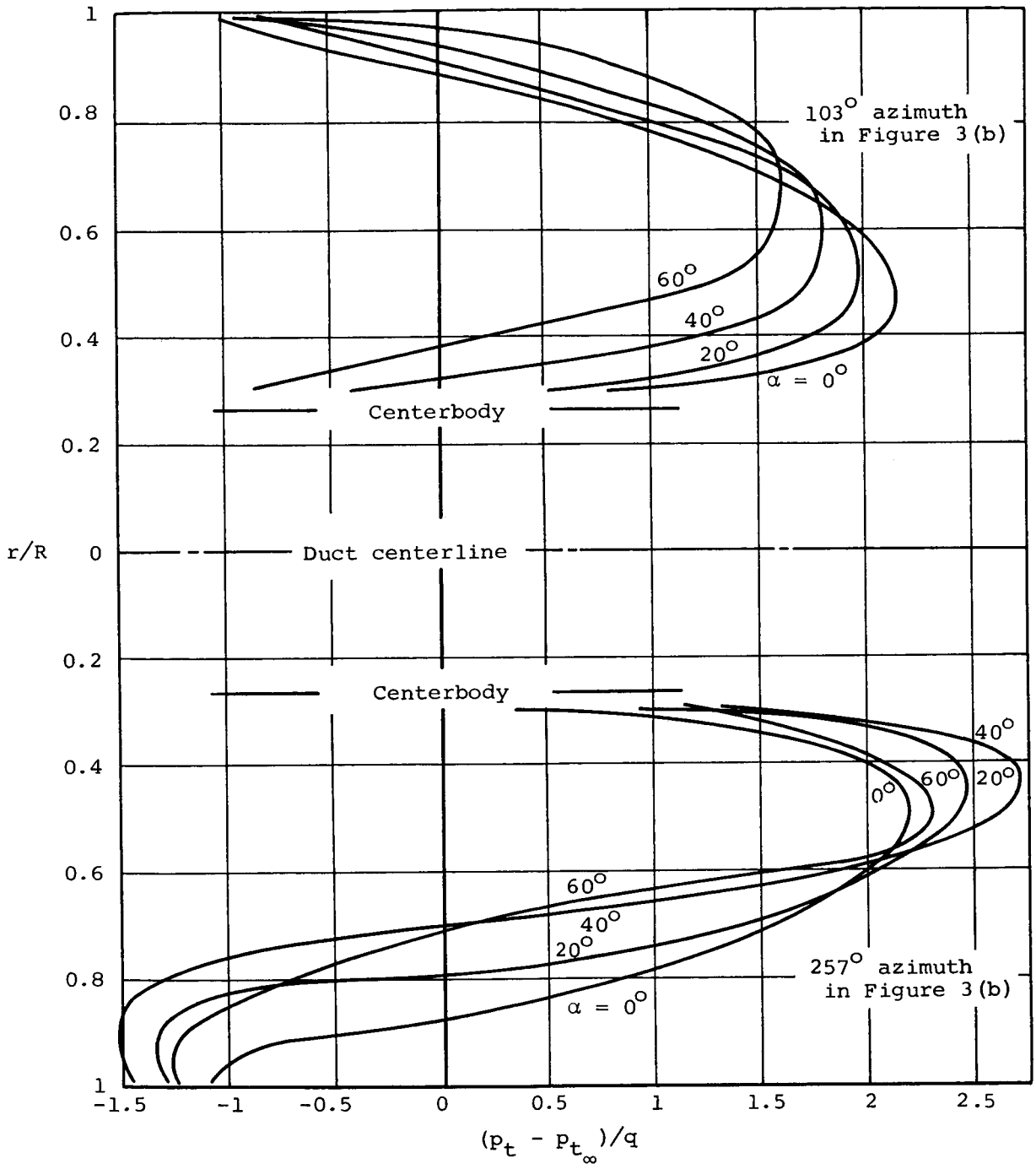

(a) $J \simeq 0.54$.

Figure 18.- Total pressure distributions measured across the exit plane of the 4-foot model duct at $\alpha > 0$.

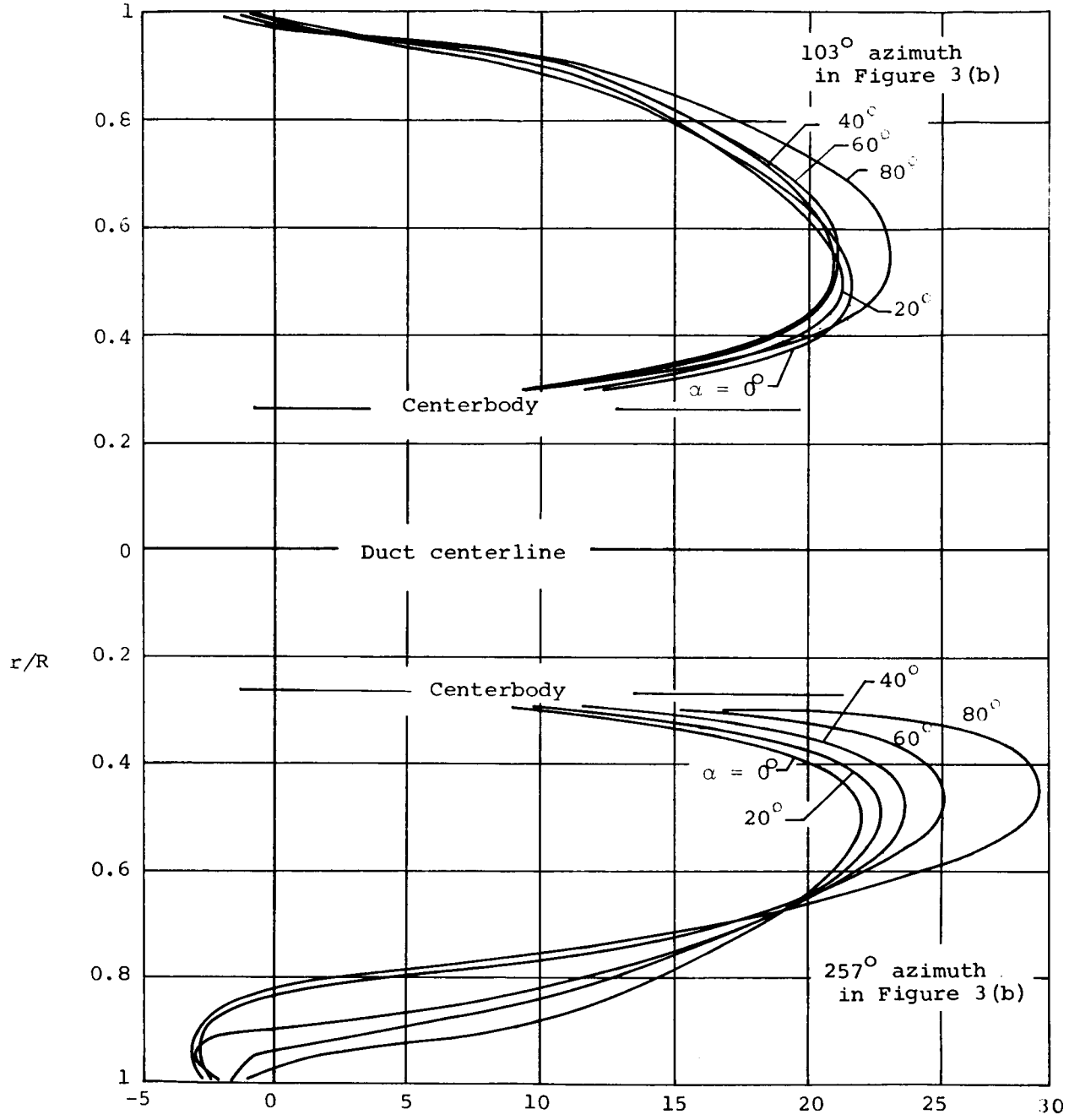

(b) $J \simeq 0.17$.

Figure 18.- Concluded.

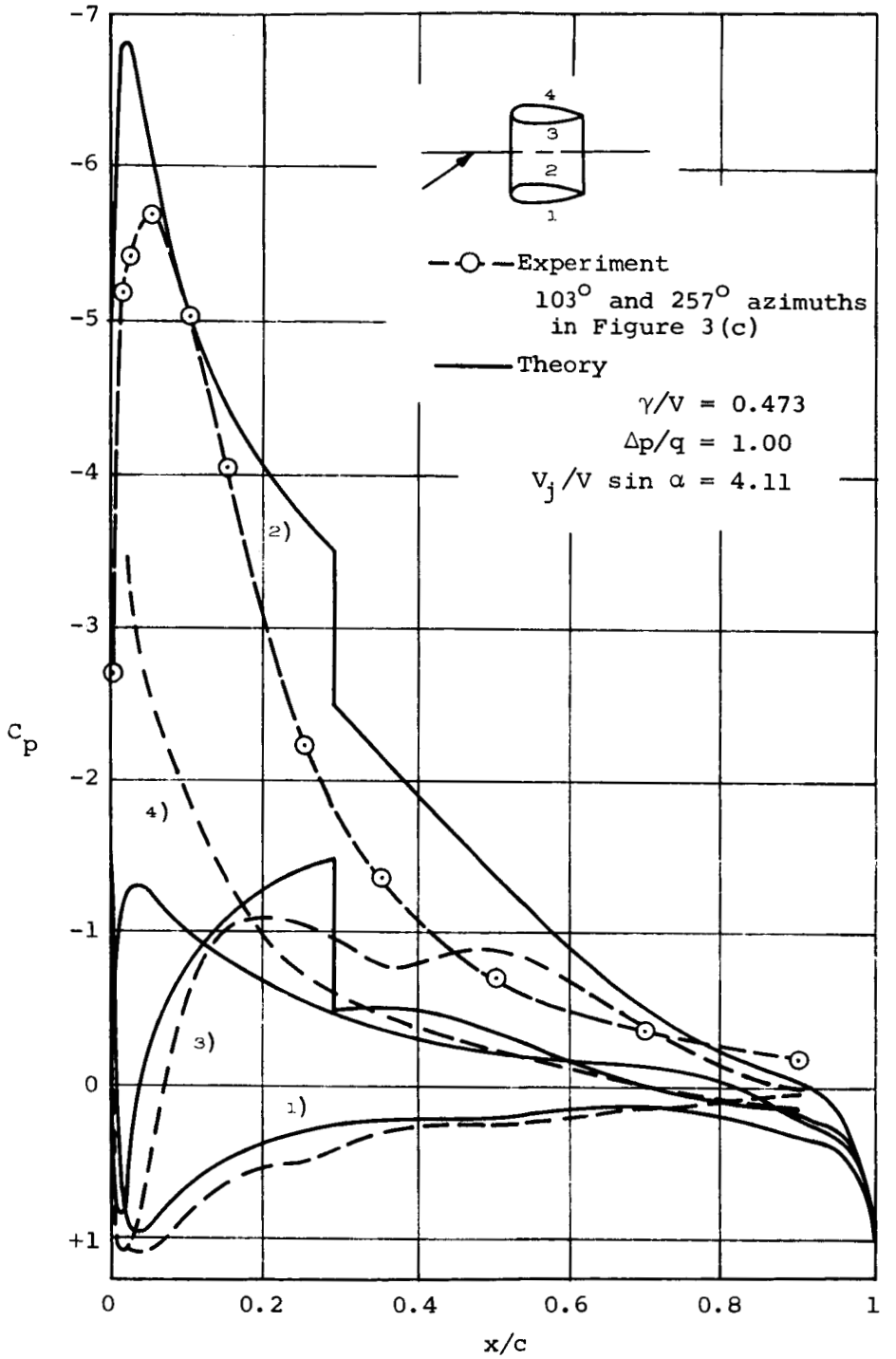

(a) $\alpha = 20^\circ$, $J = 0.521$, $C_{T_{DP}} = 1.24$.

Figure 19.- Pressure distributions for the 7-foot model duct at $\alpha > 0$ with $\beta = 19^\circ$, $\delta_e = 0$, $J \approx 0.52$.

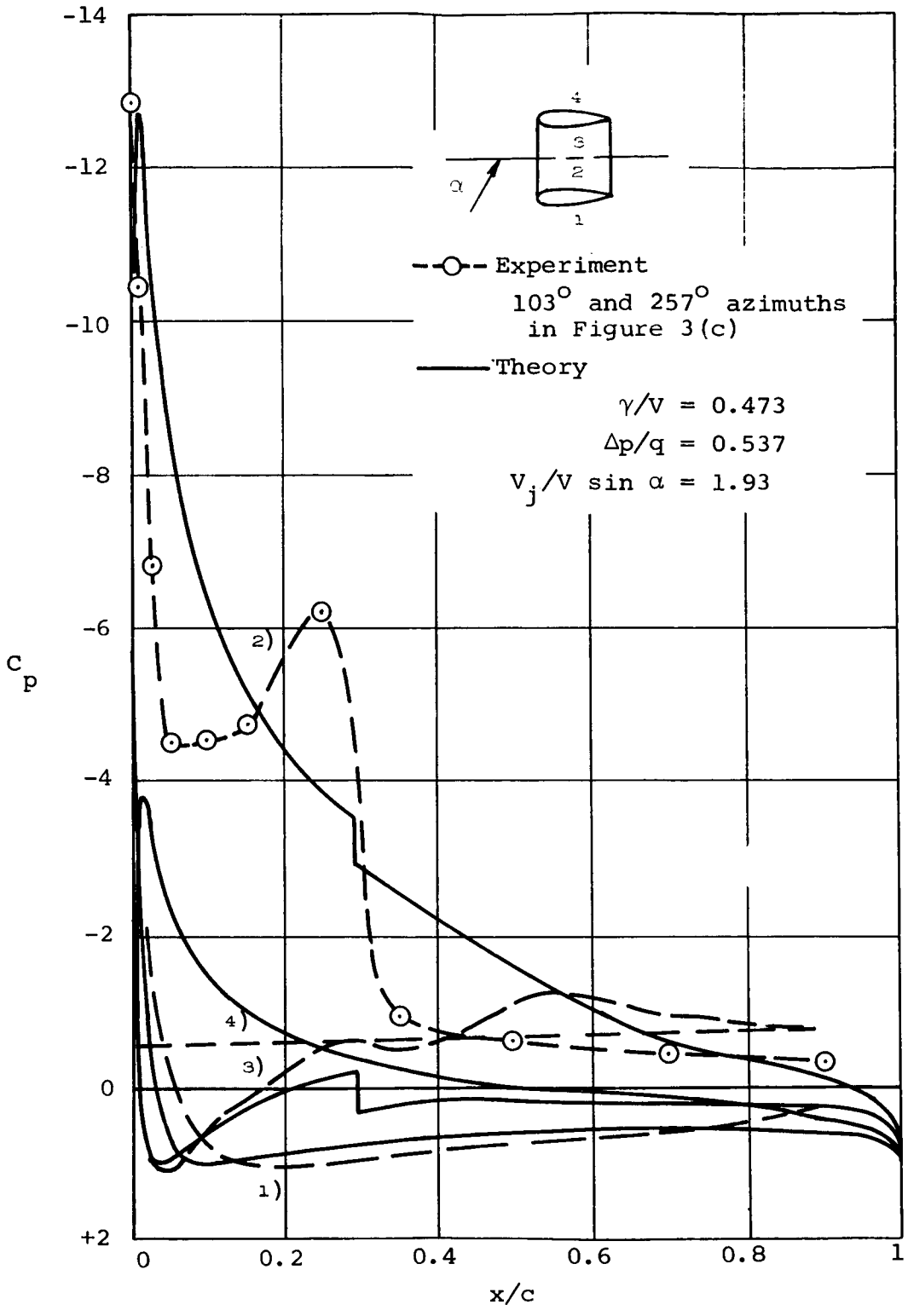

(b) $\alpha = 40^{\circ}$, $J = 0.529$, $C_{T_{DP}} = 1.53$.

Figure 19.- Concluded.

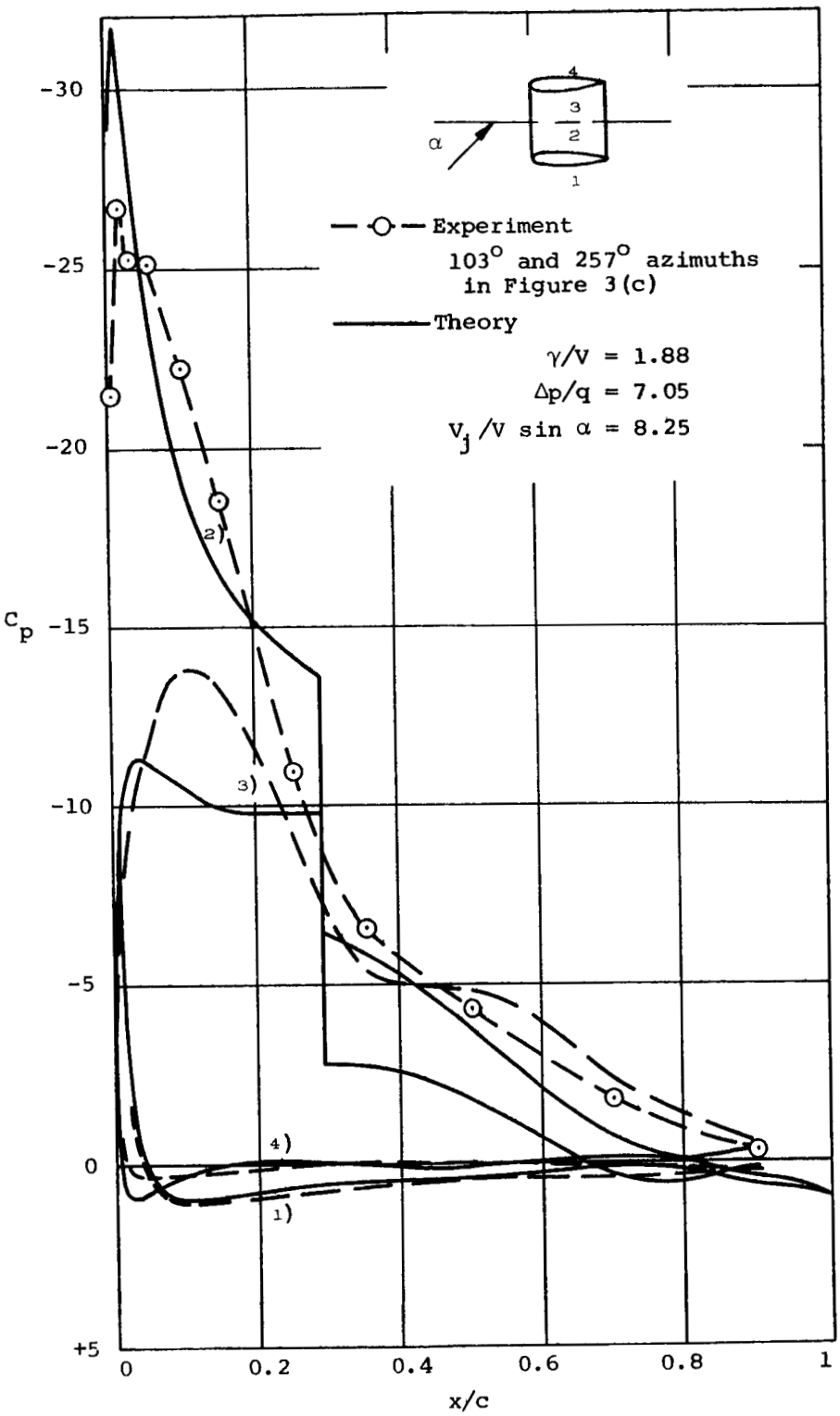

(a) $\alpha = 20^{\circ}$, $J = 0.218$, $C_{T_{DP}} = 8.77$.

Figure 20.- Pressure distributions for the 7-foot model duct at $\alpha > 0$ with $\beta = 19^{\circ}$, $\delta_e = 0$, $J \approx 0.20$.

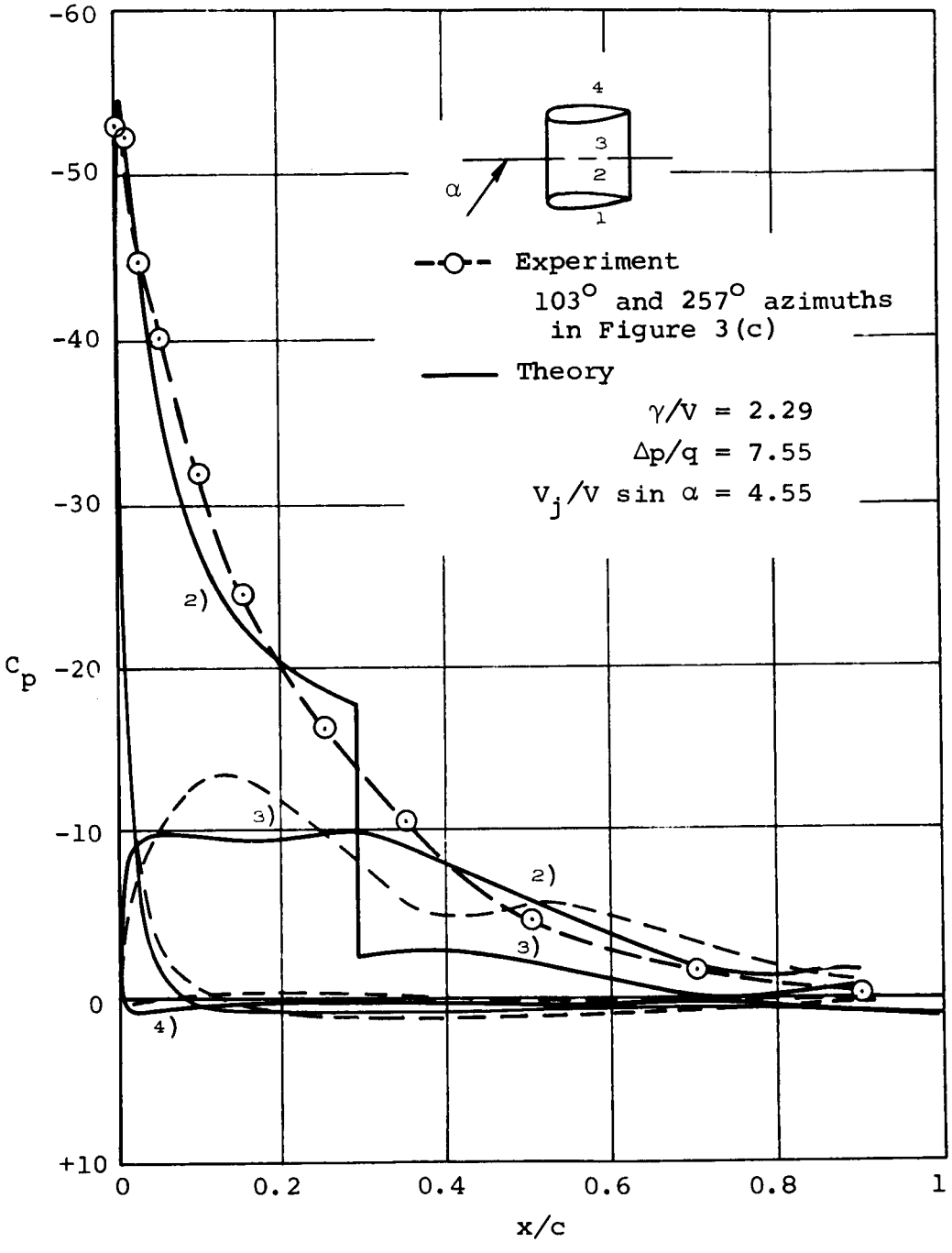

(b) $\alpha = 40^\circ$, $J = 0.199$, $C_{T_{DP}} = 12.0$.

Figure 20.- Concluded.

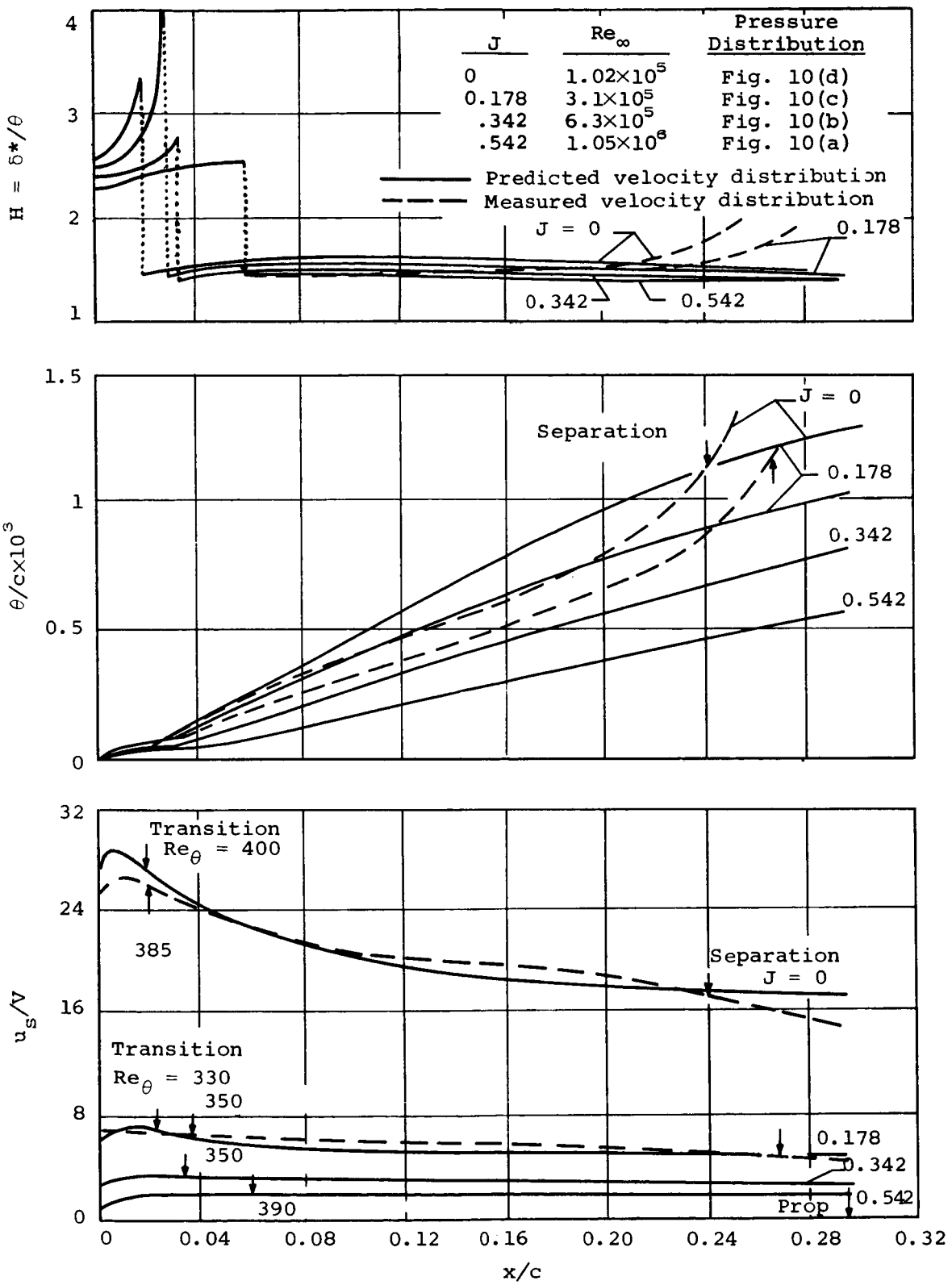

Figure 21.- Computed boundary layers for the 4-foot model duct at $\alpha = 0$.

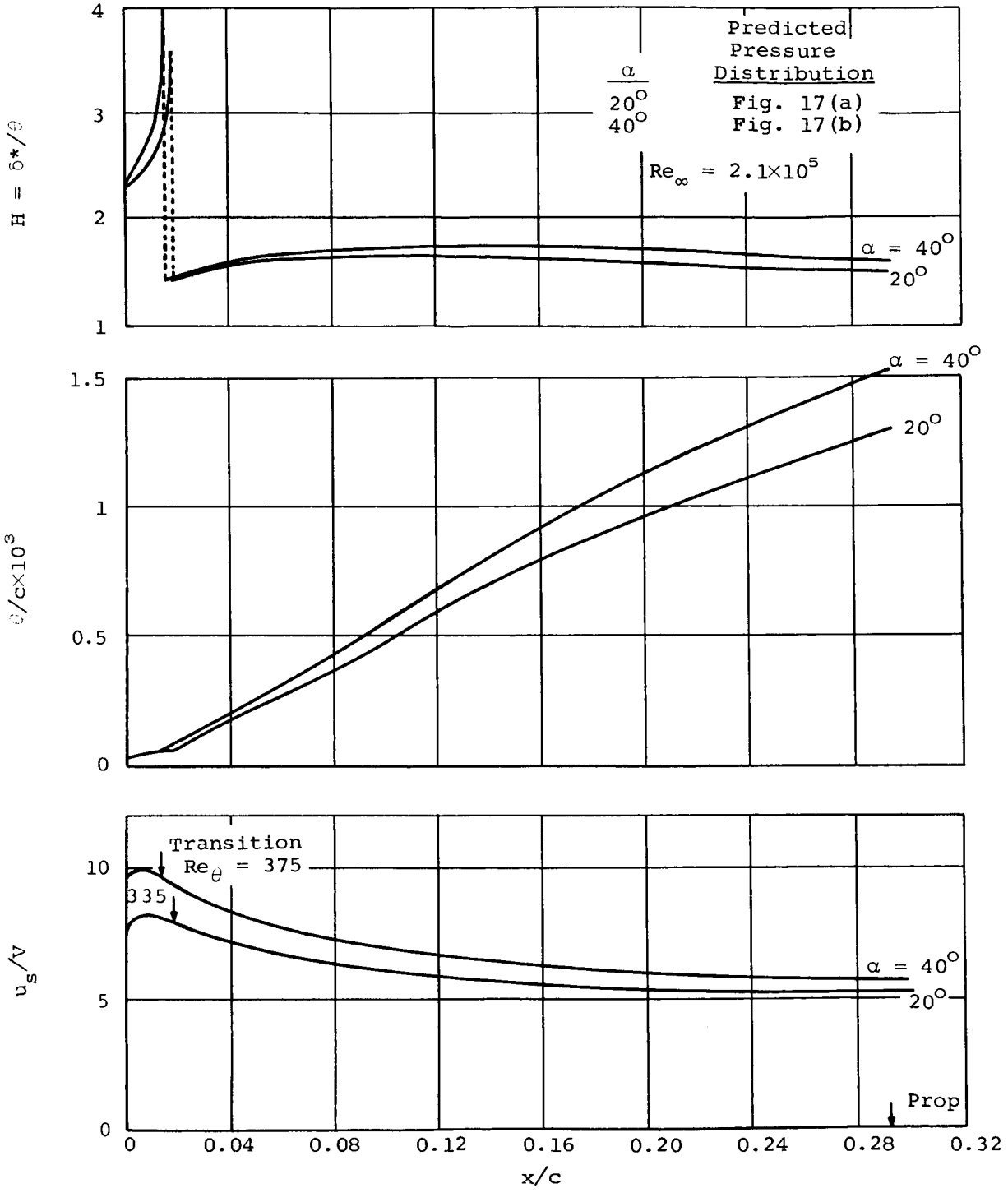

(a) $\alpha = 20^{\circ}$, J = 0.178; and $\alpha = 40^{\circ}$, J = 0.178.

Figure 22.- Computed boundary layers for the 4-foot model duct at $\alpha > 0$, J $\simeq$ 0.17.

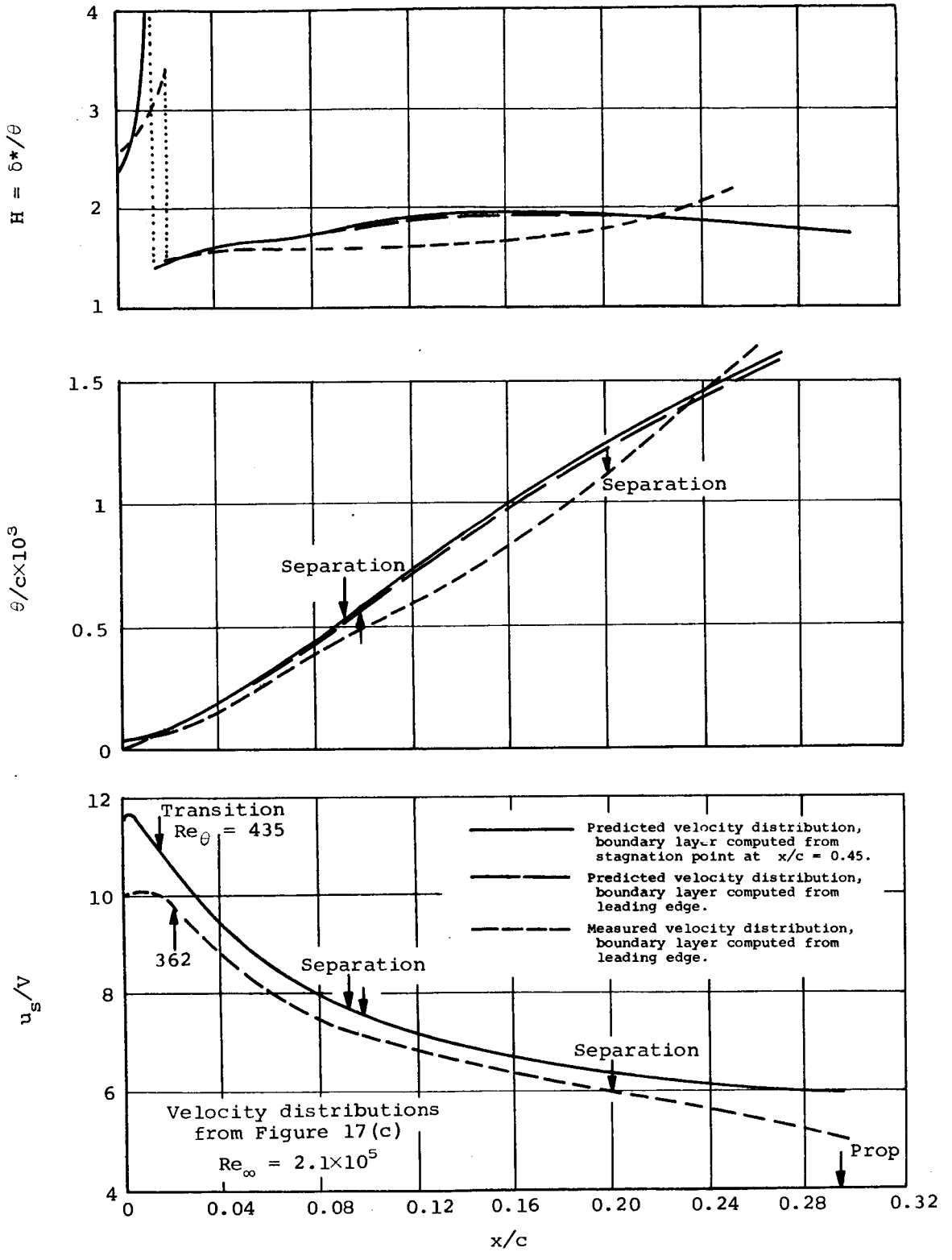

(b) $\alpha = 60^\circ$, J = 0.176.

Figure 22.- Continued.

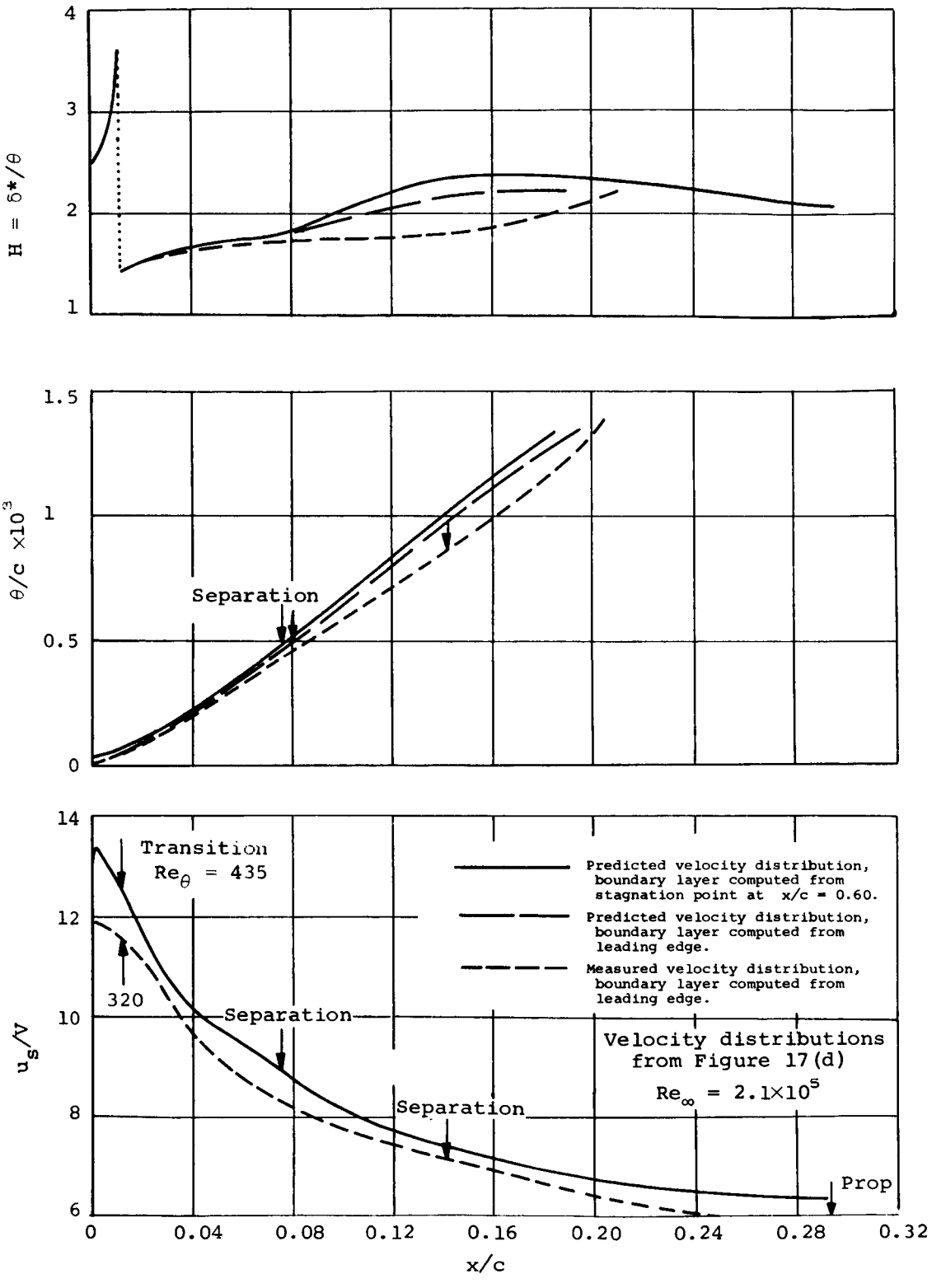

(c) $\alpha = 80^{\circ}$, J = 0.166.

Figure 22.- Concluded.

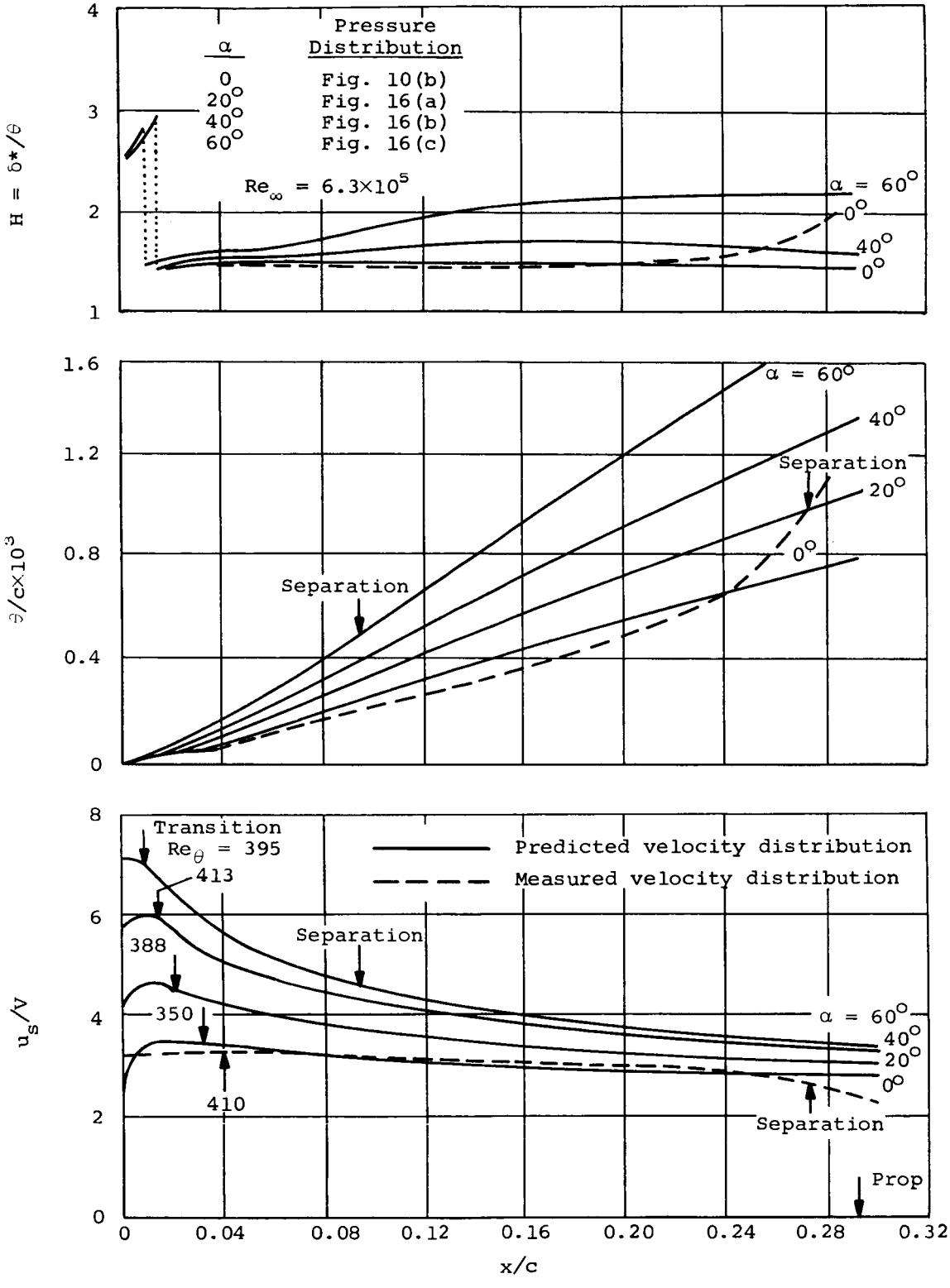

Figure 23.- Computed boundary layers for the 4-foot model duct at $\alpha \geq 0$, $J \approx 0.34$.

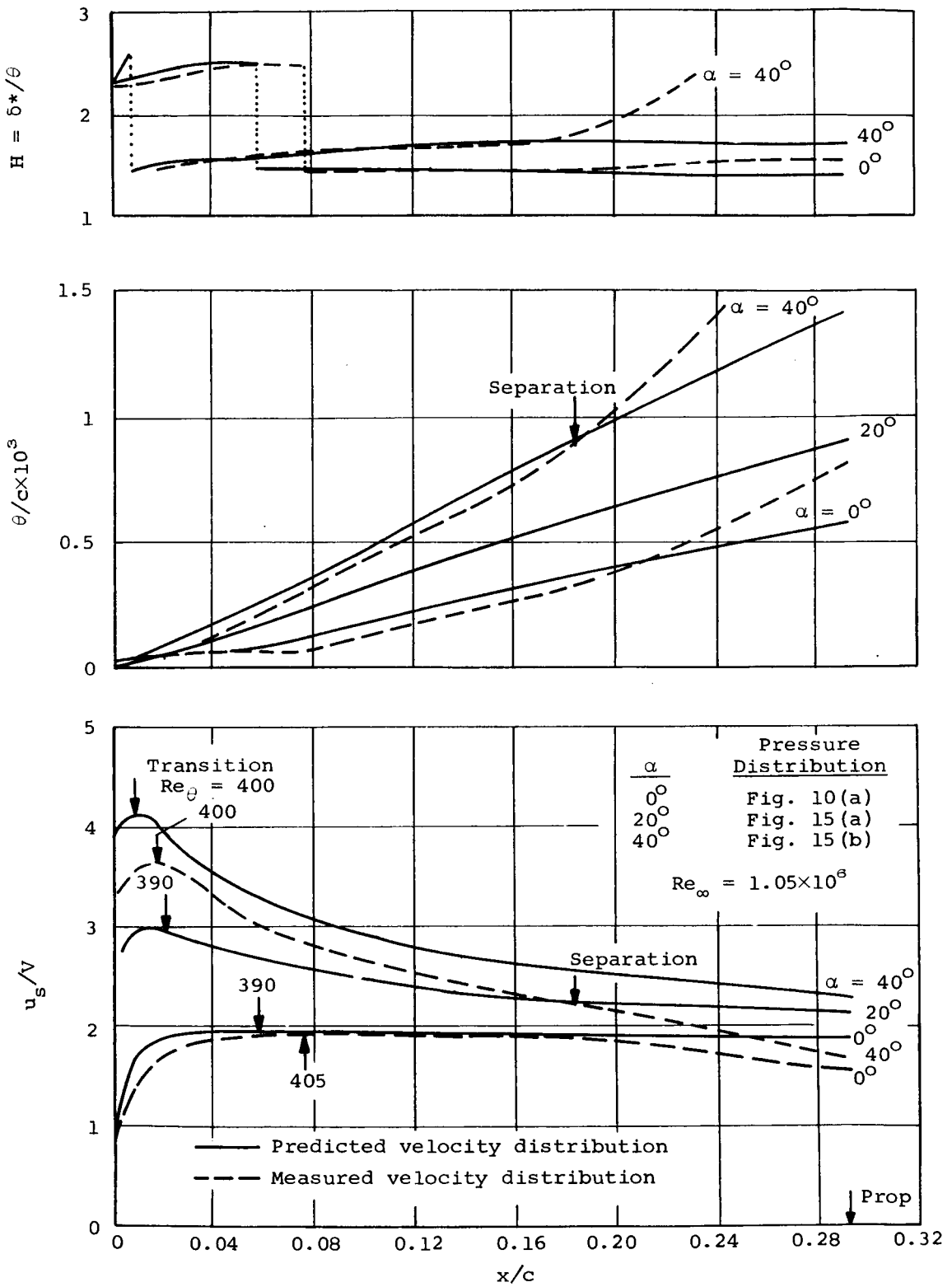

Figure 24.- Computed boundary layers for the 4-foot model duct at $\alpha \geq 0$, $J \simeq 0.54$.

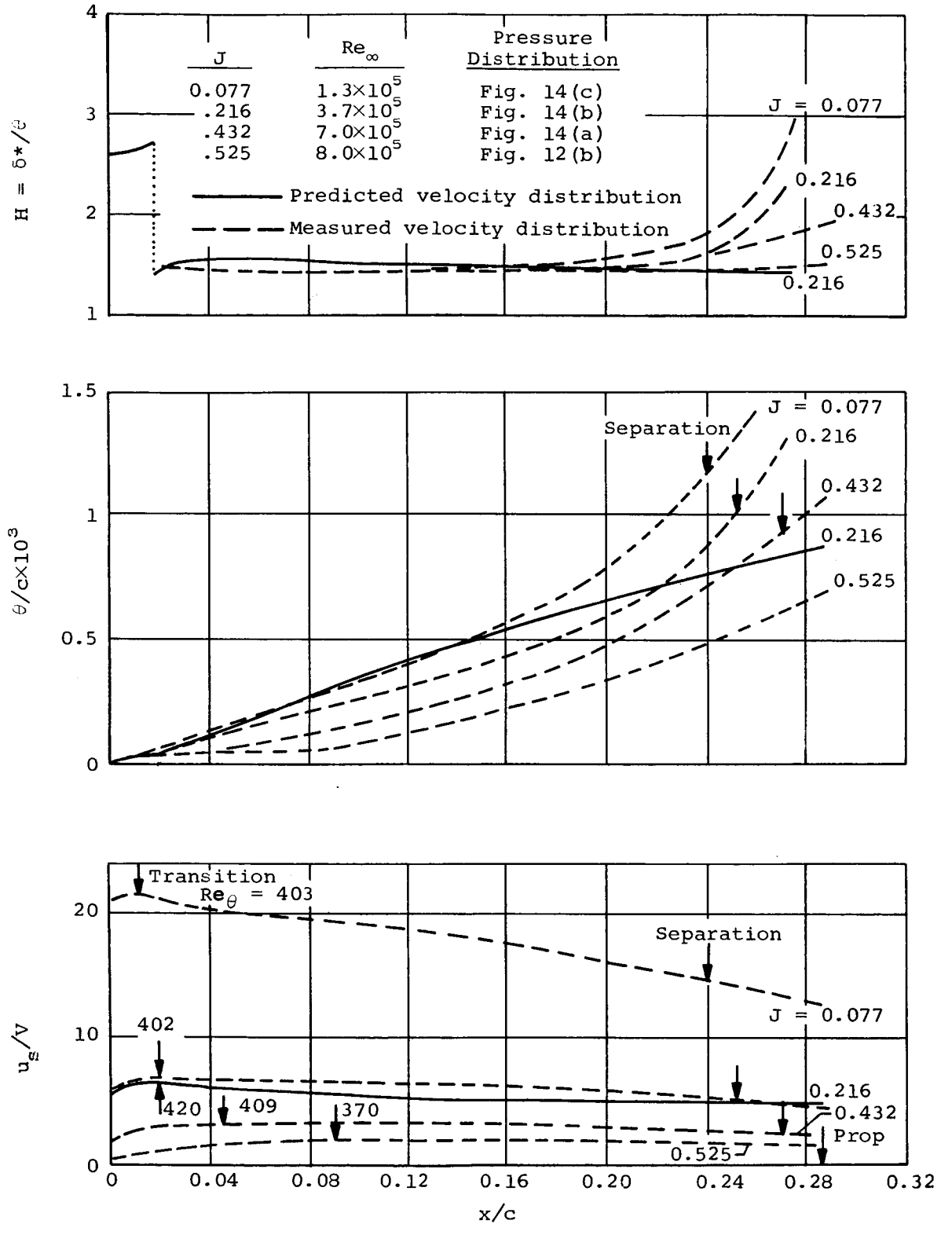

Figure 25.- Computed boundary layers for the 7-foot model duct at $\alpha = 0$.

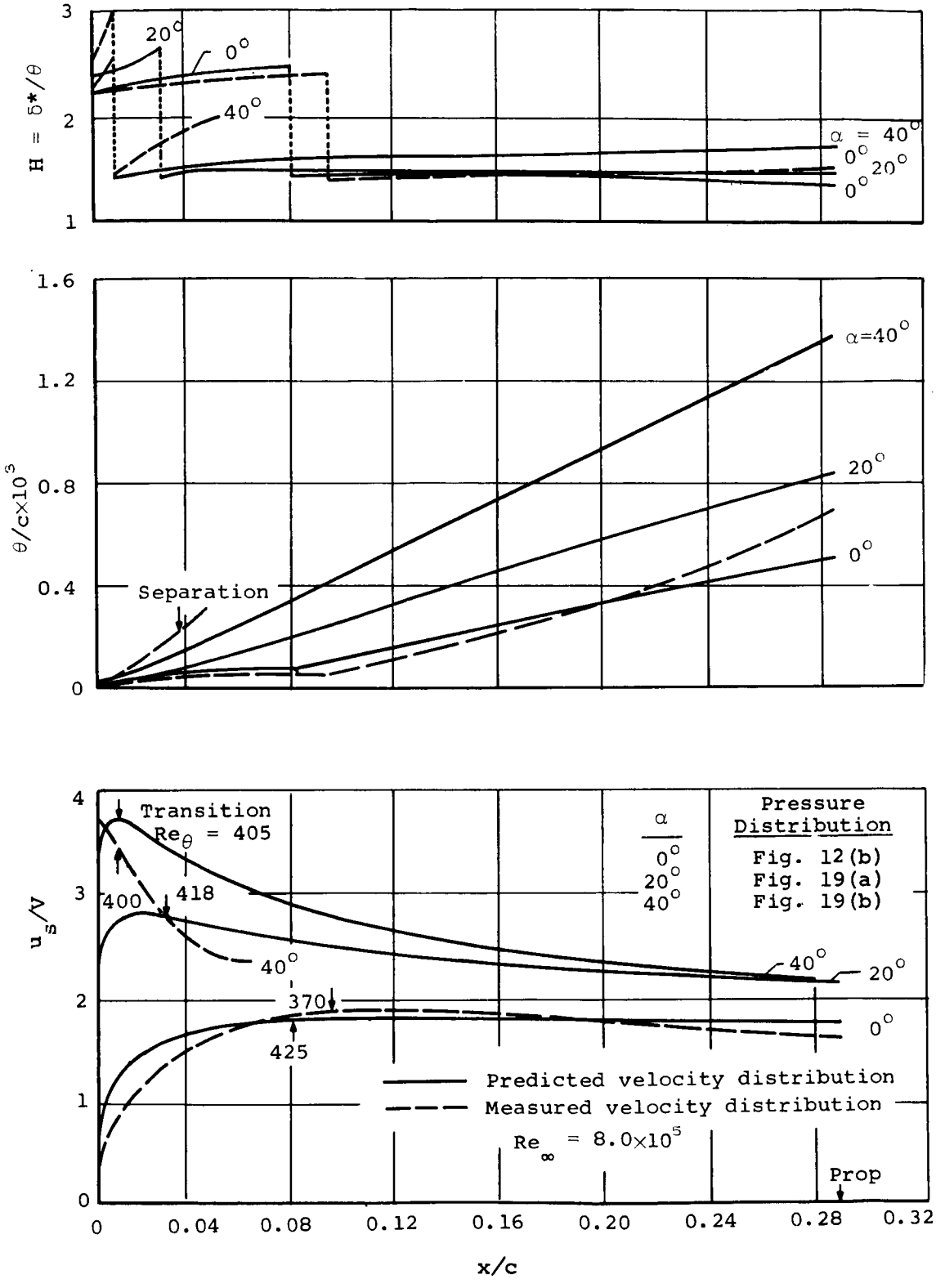

(a) $J \simeq 0.52$.

Figure 26.- Computed boundary layers for the 7-foot model duct at $\alpha \geq 0$.

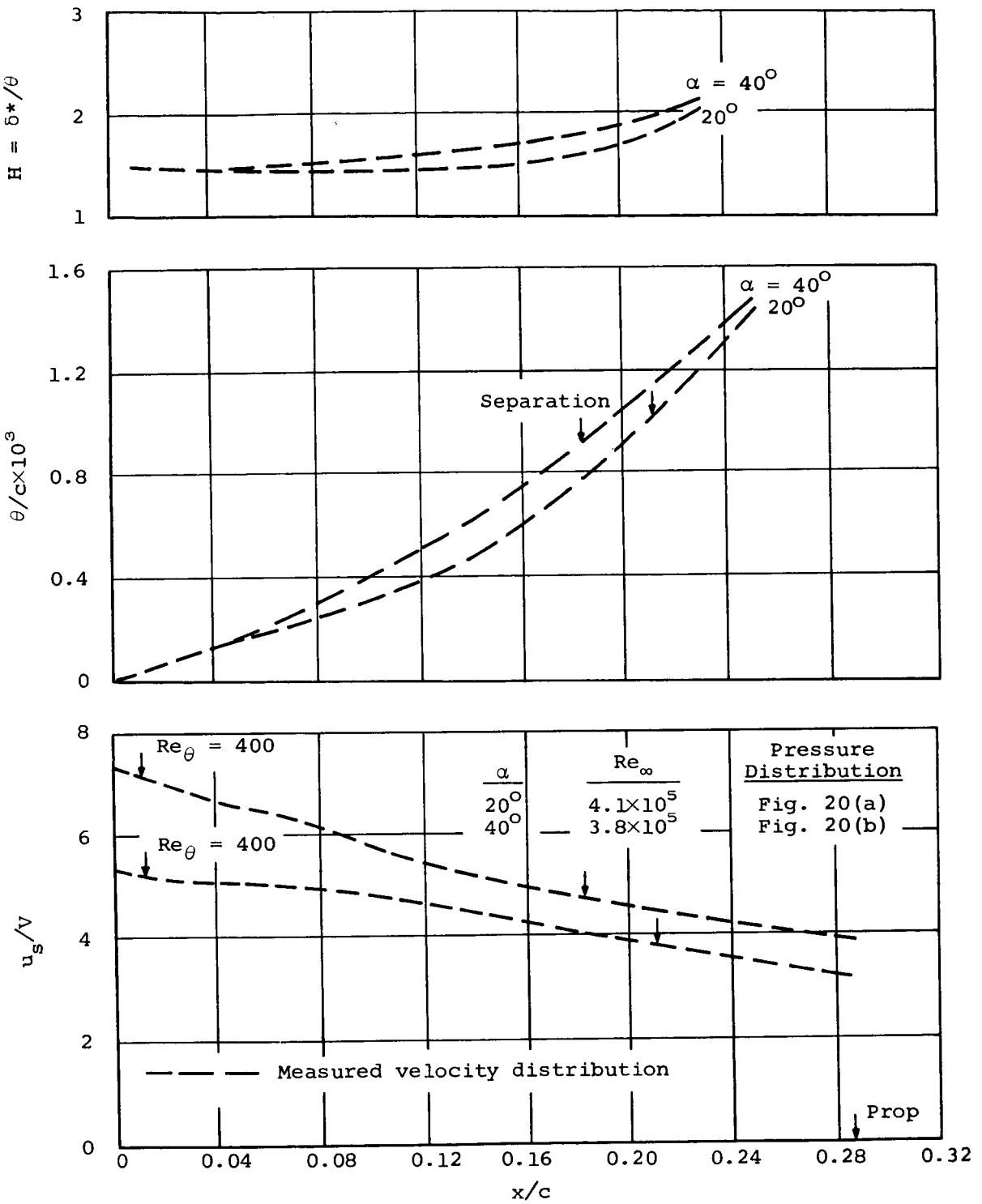

(b) J ≃ 0.21.

Figure 26.- Concluded.

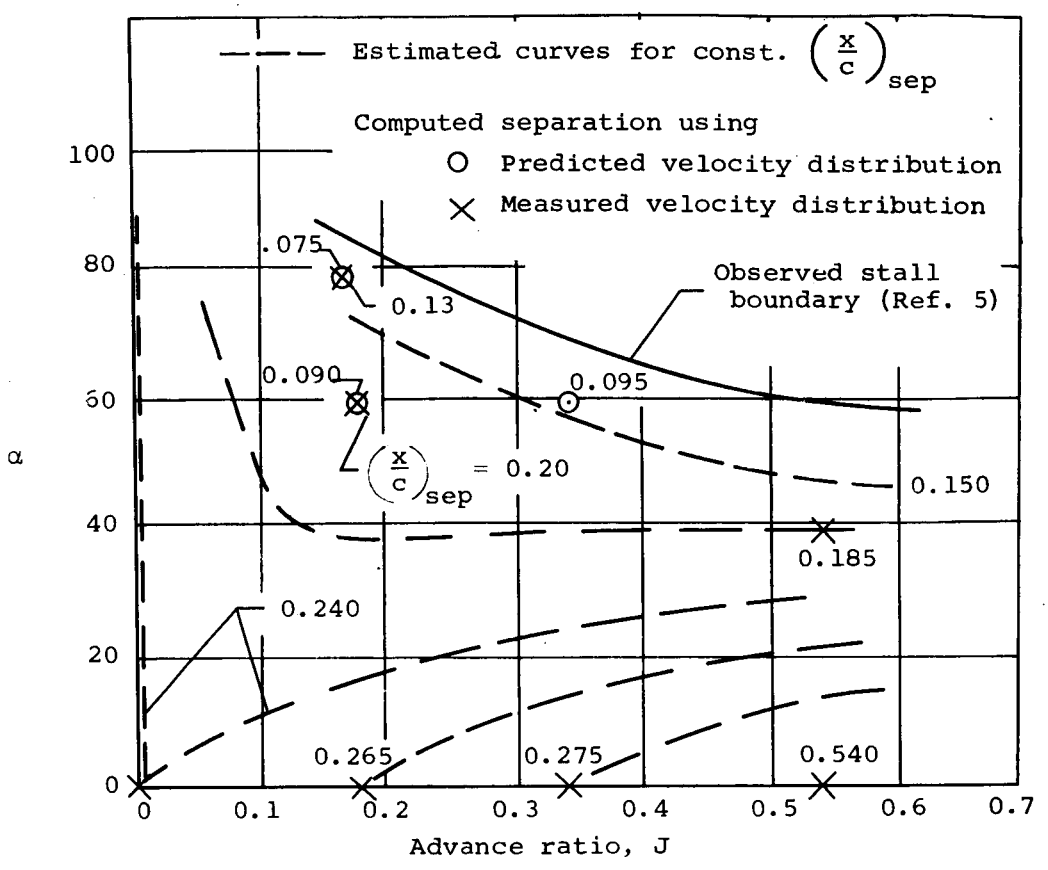

(a) Observed stall boundary and computed separation points for the 4-foot model duct.

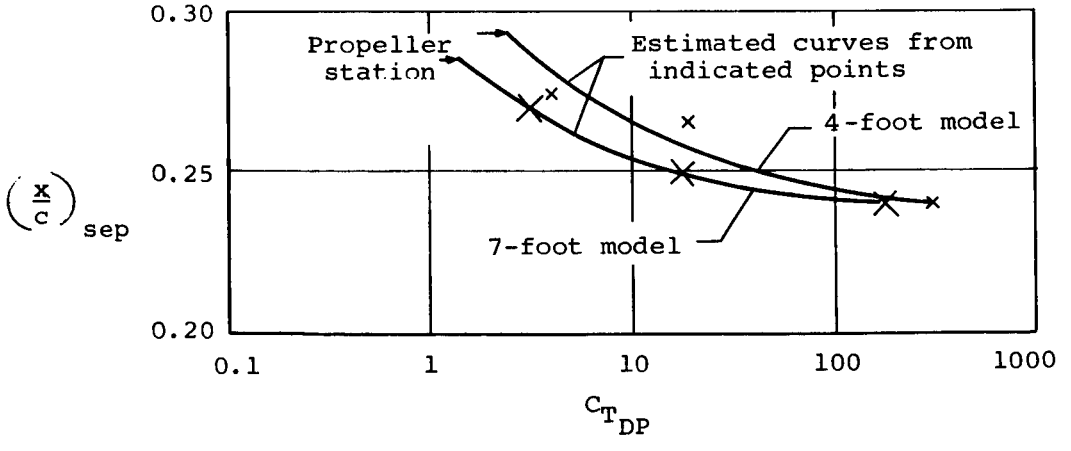

(b) Computed separation points for both ducts at $\alpha = 0$.

Figure 27.- Flow separation for both ducts.

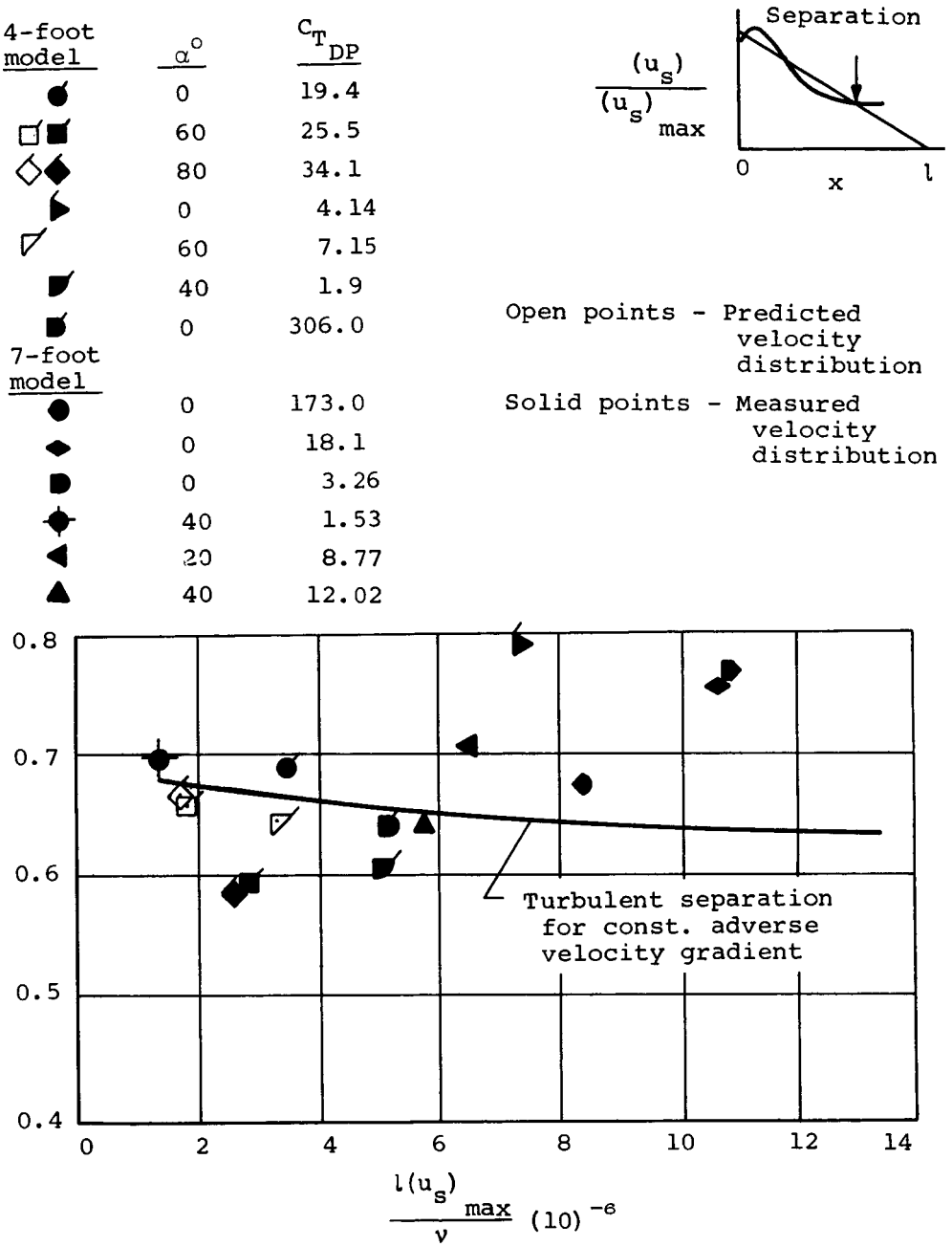

Figure 28.- Summary of computed location of separation for both ducts.